Characteristics and Generation Mechanism of Polar Cap Patches: Multi-instrument Observations

by

Jiaen Ren

A dissertation submitted in partial fulfillment
of the requirements for the degree of
Doctor of Philosophy
(Climate and Space Sciences and Engineering)
in the University of Michigan
2022

Doctoral Committee:

Associate Professor Shasha Zou, Chair
Assistant Professor Yang Chen
Professor Mark B. Moldwin
Professor Aaron J. Ridley

Jiaen Ren
jiaenren@umich.edu
ORCID iD: 0000-0002-9605-1608

DEDICATION

This work is dedicated to my mother Sulian Zou, my father Xiaolong Ren and my girlfriend Li Fang.

ACKNOWLEDGMENTS

I would like to express my deepest appreciation to Professor Shasha Zou for her continuing support, encouragement and mentorship throughout the past five years. I'm also grateful to the colleagues I worked with, Zihan Wang, Thomas Coppeans, Doğacan Su Öztürk, Lei Liu and Ercha Aa for their help and discussions. Especially, I would like to thank Zihan Wang for a lot of helpful discussions throughout our graduate studies, Thomas Coppeans for the collaboration and help on development of the visualization software. Many thanks to Mark Moldwin, Aaron Ridley and Yang Chen for their service on my committee.

I also would like to thank Kevin Sterne and Michael Ruohoniemi for providing the SuperDARN data, Anthea Coster for the help with the TEC data and Elizabeth Kendall for providing the Sondrestrom ISR data used in Chapter 2 of this dissertation, Robert G. Gillies and Eric Donovan for processing and preparing the RISR-C data used in Chapter 3, and Roger H. Varney, Ashton S. Reimer for their help and suggestions on the PFISR data used in Chapter 4. Thanks also to Yang Chen, Jiayue Lu and Naomi Giertych for their work and advice on the study in Chapter 4.

TABLE OF CONTENTS

LIST OF FIGURES

FIGURE

ABSTRACT

This dissertation includes studies on the generation mechanisms and plasma characteristics of polar cap patches and ion upflows in the high-latitude ionosphere, which is a region that involves dynamic processes reflecting the coupling of the solar wind, magnetosphere and ionosphere. Observational datasets from coherent and incoherent scatter radars (ISRs), Global Positional System (GPS) receivers and Low-Earth Orbiting (LEO) satellites were used in these studies. Polar cap "patches" are $\sim$100 to 1,000 km islands of high-density plasma present in the polar cap, which can cause scintillation of communication and navigation signals. Using the global total electron content (TEC) maps and observations from the Sondrestrom ISR, we investigated a dynamic generation process of a polar cap patch during the geomagnetic storm on 13 October 2016. Evidence showed that the patch was segmented from the Storm-enhanced density (SED) by a transient fast flow associated with dayside magnetic reconnection. The roles of enhanced frictional heating and transport of ambient plasma in the segmentation process were discussed. In another work, based on 7-months of measurements taken by the Canadian component of the Resolute Bay ISR (RISR-C) in 2016, an automatic algorithm to identify the polar cap patch was developed and a database of 437 patches was constructed. We then studied the Magnetic Local Time (MLT) distribution of the patch occurrence frequency and also conducted a superposed epoch analysis on the altitude profiles of plasma density, temperature and field-aligned ion fluxes measured within the patches. The results showed that the patch electron temperature is typically lower than its surrounding areas, indicating their major source is the solar radiation produced plasma on the dayside mid-latitude region. When high-density plasma structures, such as the SED and polar cap patch, seed ion upflow in the F region and topside ionosphere, large ion fluxes can be produced, which may have significant impact on the distribution of ion outflow. We investigated the statistical characteristics of ion upflow and downflow using a 3-year (2011–2013) dataset from the Poker Flat ISR (PFISR). The results showed that ion upflow occurs more frequently on the nightside and when the ionospheric convection speed and the geomagnetic activity level increase. The downflow occurs most often on the dayside subauroral region when the IMF By $>$ 10 nT and the IMF Bz $<$ -10 nT, which we suggest is associated with enhanced plasma pressure gradient and poleward thermospheric wind during the decaying phase of the dayside SED and the SED plume. Results in this dissertation deepen our understanding of the polar cap patch and ion upflow in terms of their formation and plasma characteristics, and can be applied to studies of high-latitude high-density structure related scintillations

and be used to validate and improve numerical models of the high-latitude ionosphere.

CHAPTER 1

Introduction

1.1 Solar wind-magnetosphere-ionosphere coupling

1.1.1 Solar wind

As the star of the Solar System, the Sun has been emitting radiation steadily over the past billions of years, which made it possible for the development of life on Earth. Besides radiation, the Sun has also been a continuous source of interplanetary plasma and magnetic field that is the so called *solar wind*, which strongly controls the near-Earth space environment. The *solar corona*, the outermost layer of the solar atmosphere, has a temperature ($\sim 10^6$ K) so high that the hot ionized plasmas flow radially away from the Sun and drags the solar magnetic field lines along with them into space, which become the solar wind with interplanetary magnetic field (IMF) embedded.

Near the Earth, the solar wind is supersonic with a speed of ∼200-900 km/s, plasma number density ∼1-80 cm^{-3} and electron temperature $\sim 10^5$ K (Schunk and Nagy, 2009). The magnitude of the IMF decreases from $\sim 10^5$ nT near the Sun to a few nT at Earth orbit.

Some structures in the solar wind with enhanced plasma pressure and IMF strength may cause severe geomagnetic effects on the Earth. One such structure is caused by speed differences in the solar wind. The general solar wind speed depends on the magnetic field structure and strength in the corona. In regions named *coronal streamers*, where the solar magnetic field forms a loop that makes it harder for the hot plasma to escape, slow solar wind results. In other regions called *coronal holes*, where the magnetic field is radially aligned, fast solar wind is generated. The rotational period of the Sun varies from around 25 days at the equator to around 31 days near the pole. As the solar magnetic field dragged radially outward, its footprint on the surface of the Sun rotates slowly, which bends the IMF into spiral shapes. The spiral angle is dependent on the solar wind speed, and when the slow solar wind is closely followed by a stream of fast solar wind, the two streams create a spiral compression zone at their interface, which is called a *corotating interaction region* (CIR). The resulting pressure enhancement may develop into shock waves when the speed

difference of the two streams exceeds the local sound and Alfvén speed, which occasionally occur before reaching 1 AU.

Another geoeffective solar wind structure is caused by a transient release of a large amount of particles in the solar coronal, named *coronal mass ejections* (CMEs). The speed of the CMEs varies from a few hundreds to over one thousand km/s. As fast CMEs move into the slower background solar wind, becoming the so-called *interplanetary CMEs* (ICMEs), shock waves often develop in front of them. The ejected plasma in the ICME is often associated with strong and smoothly rotating magnetic fields called *magnetic clouds*. Once a CME is released from the Sun, it usually takes 1-3 days to reach Earth's orbit. The enhanced IMF within the magnetic cloud, if directed southward, can cause intense geomagnetic disturbances.

1.1.2 The Earth's magnetosphere

The Earth has an intrinsic magnetic field that can divert charged solar wind particles and protects the atmosphere from being directly exposed to the interplanetary environment. Within a few Earth radii, the terrestrial magnetic field can be approximated by a dipole field with field lines originating from the magnetic north near the geographic South Pole to the magnetic south near the geographic North Pole. Beyond this range the Earth's magnetic field interacts with the solar wind and therefore deviates from the dipole approximation. As shown in Figure 1.1, on the upstream side, the terrestrial magnetic field is compressed by the supersonic solar wind and a *bow shock* is formed in front of the magnetopause. The region between the bow shock and magnetopause is named the *magnetosheath*, where the shocked solar wind is deflected and flows around the magnetopause on the flanks. The magnetopause is a tangential discontinuity boundary that separates the magnetosheath and the *magnetosphere*, which refers to the space dominated by the Earth magnetic field. The location of the magnetopause is determined by the pressure balance between the magnetosphere and magnetosheath, and is typically at 10 Earth radii (R_E) away along the Earth-Sun line. On the flanks, the solar wind velocity gradually becomes parallel to the magnetopause, which leads to a long magnetotail in a roughly cylindrical shape. The tail is separated by the central plasma sheet into the northern and southern lobes, where the magnetic fields have opposite directions. The energetic charged particles in the plasma sheet move towards the Earth and become trapped in closed magnetic field lines in the inner magnetosphere. These trapped particles also rotate around the Earth under the gradient and curvature of the magnetic field with electrons and ions moving in opposite directions, which creates a net current around the Earth known as the *ring current*.

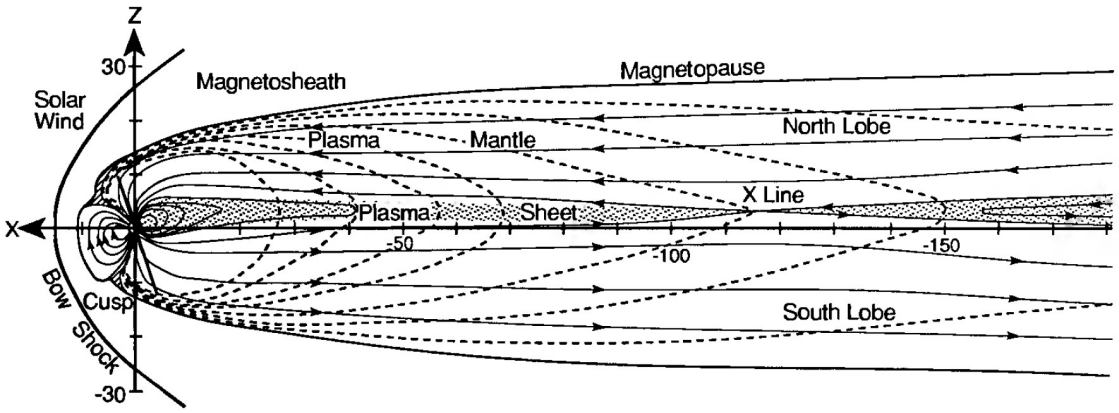

Figure 1.1: Illustration of the Earth's magnetosphere configuration. From Kivelson et al. (1995)

1.1.3 The Earth's ionosphere

The Earth's ionosphere refers to regions above $\sim$ 60 km altitude where the neutral atmosphere is partially ionized and significant amount of electrons and ions are produced mainly by photons and energetic particle precipitation. The main source of Earth's ionosphere is photons of the solar radiation at X-ray and extreme ultraviolet (EUV) wavelengths. The ionization due to particle precipitation may be important in some regions, such as the auroral zone. When atoms or molecules of neutral gas absorb a photon with energy exceeding their ionization potential, free electron and ion pairs are produced. This process is called *photoionization*. The primary neutral constituents for photoionization are N_2, O_2 and O. The ions and electrons recombine into neutral particles and reduce the ionosphere plasma density. The production rate of photoionization is proportional to both the solar radiation intensity and the neutral gas density. While the former increases with altitude, the latter decays with altitude. As a result, a peak ionization production rate can be found near 100 km altitude. The dominant mechanisms that produce, recombine and transport the ion vary with altitude and, based on the inflection points in the vertical electron density profile, the ionosphere can be categorized into 5 regions: D (60 - 90 km), E (90 - 140 km), F1 (140 - 200 km), F2 (200 - 500 km) and topside (above the peak ion density), as shown in the Figure 1.2. On the night side, without the photoionization from sunlight, the D, E and F1 regions dramatically reduce while the F2 region has much less plasma density mainly due to recombination.

In the D region, the main ionization source is X rays ionization of N_2, O_2 and Lyman-α ionization of NO, which produces O_2^+ and NO^+ as the major ion species. The generated N_2^+ can rapidly charge exchange with O_2 to produce O_2^+ (Gombosi, 1998). In the E region, the major source is similar to the D region, while the N_2^+ can also be converted into NO^+ through charge exchange with atomic oxygen O, resulting in mainly NO^+ and O_2^+. The major ion species in the F1 region is O^+, which can be quickly converted into NO^+ and O_2^+ at lower F1 altitude $\sim$ 140 km by the

following charge exchange reactions:

$$\begin{aligned} O^+ + N_2 &\rightarrow NO^+ + N \qquad k_{N_2} \approx 1 \times 10^{-12}\ \mathrm{cm^3 s^{-1}} \\ O^+ + O_2 &\rightarrow O_2^+ + O \qquad k_{O_2} \approx 2 \times 10^{-11}\ \mathrm{cm^3 s^{-1}} \end{aligned} \tag{1.1}$$

Since the densities of N_2 and O_2 decrease as the altitude increases, in the top F1 and F2 region the ion composition becomes dominated by the O^+ produced by the photoionization of atomic oxygen. The main plasma loss of the F-region ionosphere is due to charge exchange of O^+, as described above, and the subsequent rapid dissociative recombination of NO^+ and O_2^+:

$$\begin{aligned} O_2^+ + e &\rightarrow O + O \qquad k_{O_2^+} \approx 3 \times 10^{-7}\ \mathrm{cm^3 s^{-1}} \\ NO^+ + e &\rightarrow N + O \qquad k_{NO^+} \approx 3 \times 10^{-7}\ \mathrm{cm^3 s^{-1}} \end{aligned} \tag{1.2}$$

Since the production and loss of the F region plasma are mainly controlled by O and N_2, respectively, the O/N_2 ratio is usually used as an indicator of local ionosphere density change rate. In addition to the chemical loss, electrons in the F region have little collisional effects and can diffuse along the nearly vertical magnetic field lines at high latitudes to higher altitudes under the pressure gradient. However, unlike the light-weight electrons, the ions are much heavier and therefore are bounded by the gravitational force. So the separation of elections and ions creates a polarization electric field (also named as ambipolar electric field) that can lift lighter ions (with mass less than half of the major ions) until a diffusive equilibrium is reached.

1.1.4 Coupling of the solar wind, magnetosphere and ionosphere

The general interaction between the solar wind, magnetosphere and ionosphere can be understood using the *Dungey* model (Dungey, 1961), where the mass, momentum and energy transport is driven by a process named *magnetic reconnection*. As illustrated in Figure 1.4, the model explained the general plasma convection in both the magnetosphere and ionosphere by magnetic reconnection in front of the magnetopause and in the magnetotail.

The magnetopause marks the boundary between the shocked solar wind and IMF and the magnetosphere. Most of the Earth's magnetic field lines form a closed loop at mid and low latitudes. At high latitudes, however, the field lines can be connected with the solar wind IMF and become open field lines via magnetic reconnection. Reconnection happens when field lines with opposite directions are pushed into close contact, inducing a thin current sheet. As a result, the magnetic energy converts into heat via Joule heating and particle acceleration, and the magnetic topology is changed so that the previously anti-parallel field lines break and then connect with each other.

To better study the reconnection between the IMF and the magnetosphere, we can project the

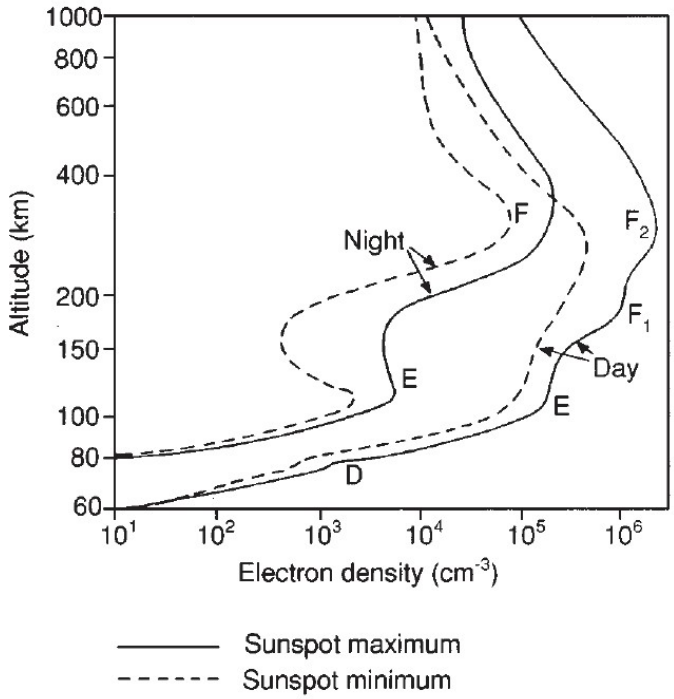

Figure 1.2: Typical ionosphere electron density vertical profiles at mid-latitude regions. From Hargreaves (1992).

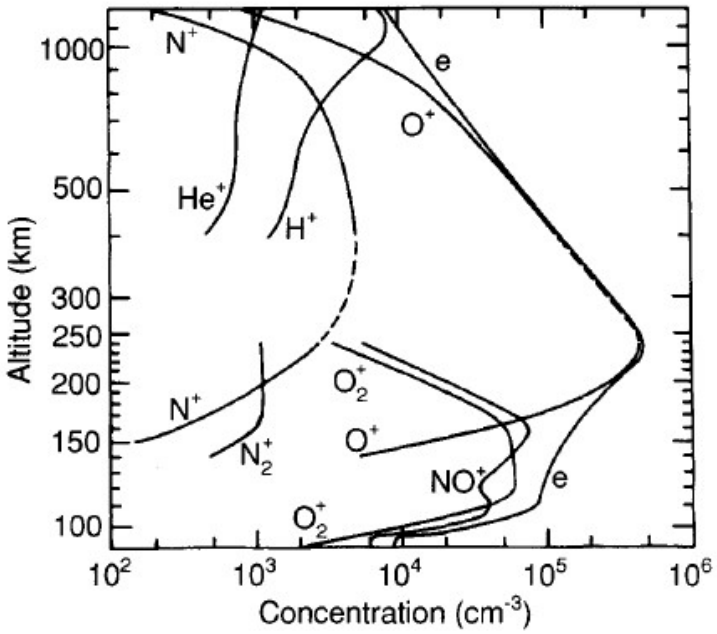

Figure 1.3: Typical vertical profiles of ionosphere composition at mid-latitude regions. From Johnson (1966).

IMF onto the geomagnetic dipole axis and see how strong the IMF is in the anti-parallel direction of the magnetosphere. More specifically, the IMF can be decomposed into 3 orthogonal components Bx, By and Bz using the Geocentric Solar Magnetospheric (GSM) coordinates, in which the origin is located at the center of the Earth and the x-axis is along the Sun-Earth line pointing towards the Sun. The y-axis is defined as the cross product of the x-axis and the Earth magnetic dipole axis, pointing towards the dusk side. Finally, the z-axis is the cross product of x- and y-axis.

During periods of southward IMF (Bz$<$0), the solar wind field lines move into the oppositely oriented geomagnetic field lines near the front of the magnetopause, triggering magnetic reconnection where closed geomagnetic field lines become open field lines connected with the solar wind IMF. In the ionosphere, these newly open field lines can be traced down into a region at high latitudes that is called the *cusp*, and the entire region with open field lines is named as the *polar cap*. The open field lines are dragged by the solar wind over the pole into the magnetotail, where the field lines are stretched into an elongated configuration. There is also viscous interaction (Axford and Hines, 1961) between the solar wind and the magnetosphere near the dawn and dusk magnetopause, where closed field lines are transported anti-sunward along the flanks towards the tail. Near the center of the magnetotail, a plasma sheet is formed with a dawn-to-dusk current that separates the tail into two lobes (north/south) with oppositely directed magnetic field. As more magnetic flux is transported from the dayside into the tail lobes, a pressure gradient builds up, thinning the central plasma sheet, and eventually leads to reconnection that closes the open field lines in the tail lobe. The newly closed field lines move towards the Earth and field lines in the nightside inner magnetosphere return to the dayside through the flanks. The charged particles in the tail plasma sheet also move sunward to the inner magnetosphere, and some are captured by the Earth's rotational electric field while others keep moving sunward towards the dayside magnetopause.

1.1.5 High-latitude ionospheric convection

In the high-latitude ionosphere, the large-scale plasma convection is mainly dependent on the electric fields and the resulting E$\times$B drift. Since the solar wind plasma can be treated as highly conducting and collisionless, in a reference frame moving with the solar wind there is no electric field, while on the Earth we experience a *convection electric field* that is given by $E_{SW} = -V_{SW} \times B_{SW}$, where V_{SW} is the solar wind velocity and B_{SW} is the IMF vector. During southward IMF conditions, E_{SW} has a direction that points towards the dusk. Since charged particles can easily move along magnetic field lines, the high conductivity prevents any significant electric potential gradient from building up along the field lines. As a result, the field lines can be treated as electric equipotentials. This means that, for the polar cap, the potential drops between different field lines in the solar wind will remain the same when the field lines are traced down to the ionosphere. Therefore,

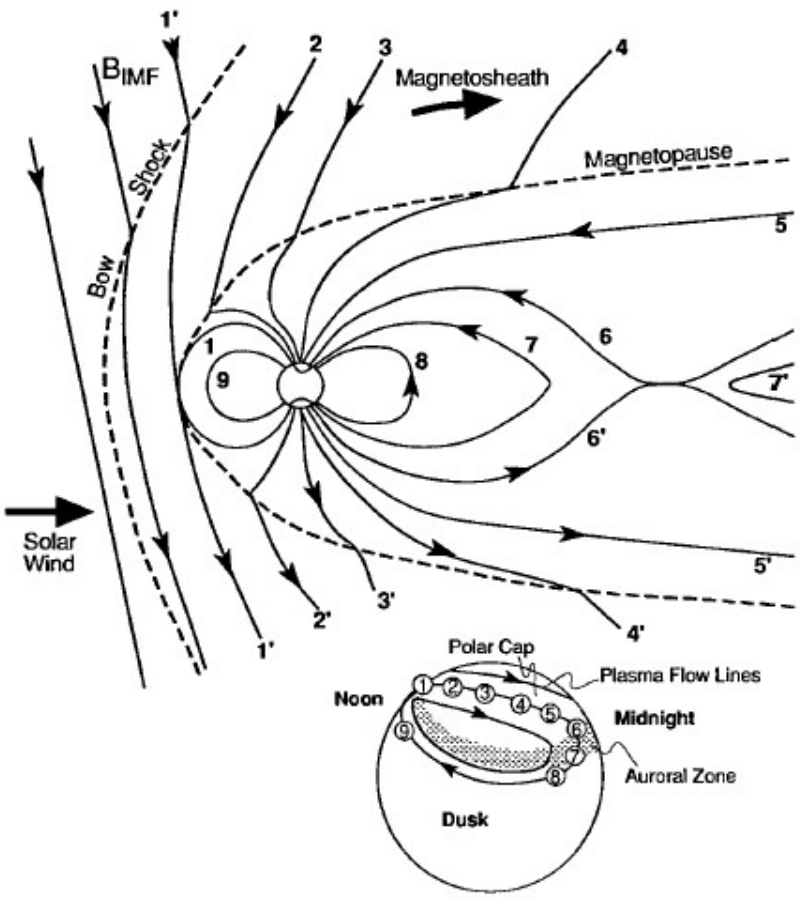

Figure 1.4: Convection of magnetic field flux and plasma in both magnetosphere and ionosphere under southward IMF conditions, as described by the Dungey model. From Hughes (1995).

during periods of southward IMF, the solar wind convection electric field is mapped down to the polar cap ionosphere as a dawn-to-dusk electric field, which drives the ionosphere plasma to move anti-sunward via the E×B drift, as shown in Figure 1.5 (b). In regions just equatorward of the polar cap boundary, which features frequent auroral activity and therefore is named the *auroral zone*, the magnetic field lines form closed loops that connect to the sunward return flow in the magnetosphere, as illustrated in Figure 1.5 (a). Along these closed field lines, the dawn-to-dusk magnetospheric electric field mapped to the auroral zone is oriented towards dusk-to-dawn, opposite to that in the polar cap. This leads to a sunward plasma flow in the ionosphere that returns to the dayside on the dawn and dusk sides, creating a so-called two-cell convection pattern shown in Figure 1.5 (c) under the southward IMF conditions. When solar wind and IMF change their conditions and influence the site and rate of the reconnection process, the plasma convection pattern in the high-latitude ionosphere will also change its size, strength and configuration (Weimer, 1996, 2001).

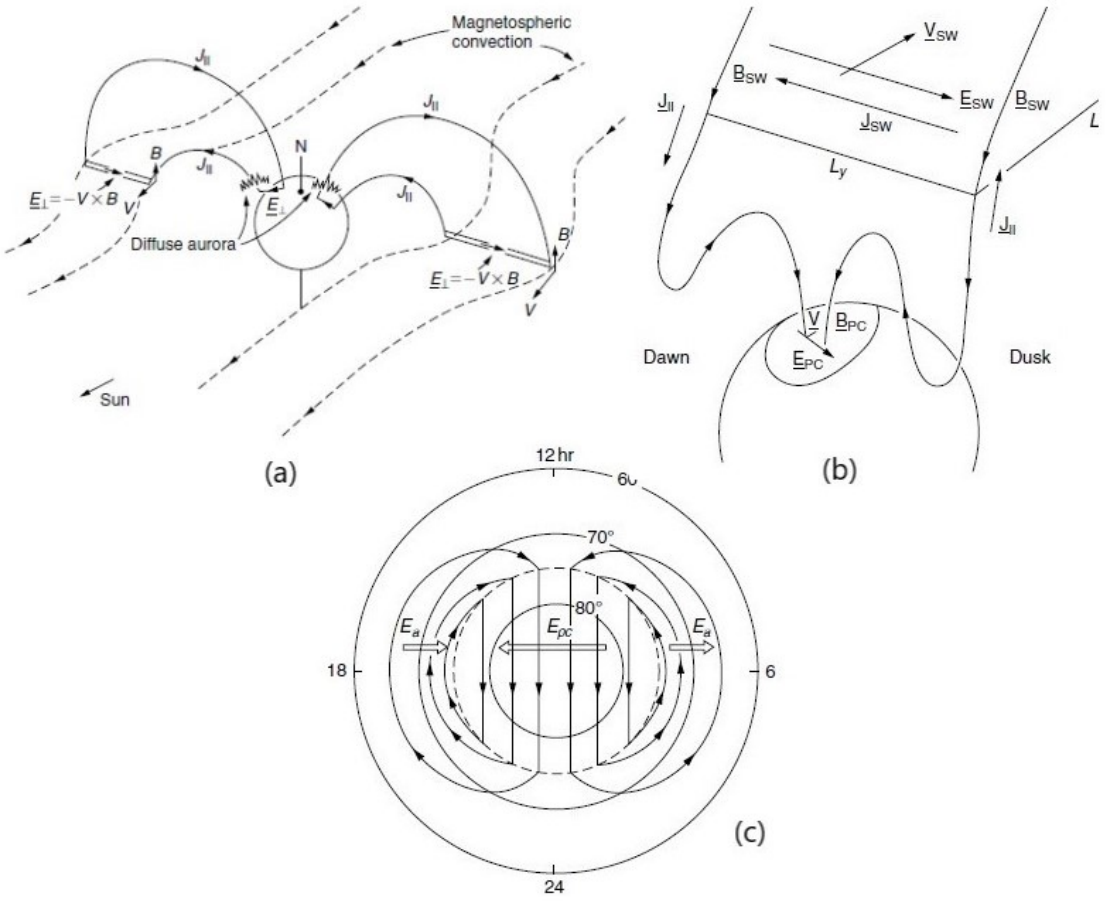

Figure 1.5: (a) 3D view of auroral zone magnetic field lines that connects the sunward flow in the inner magnetosphere on the dawn and dusk sides. (b) Schematic illustration of open field lines that connect the ionosphere polar cap with the solar wind IMF. (c) Representation of high-latitude ionosphere electric fields and the plasma two-cell convection pattern for southward IMF conditions. From Kelley (2009).

1.1.6 Geomagnetic storm

During extended periods of strongly southward IMF and enhanced solar wind speed, the magnetic reconnection rate on the dayside magnetopause significantly increases and consequently enhances the convection electric field both in the magnetosphere and ionosphere. The enhanced convection injects more energetic particles into the ring current, which further weakens the strength of the horizontal component of the magnetic field on the Earth's surface measured by the Dst and SYM-H indices. This period of intense and prolonged geomagnetic activity is named a *geomagnetic storm*. As shown in Figure 1.6, during storms, the enhanced ring current causes a rapid decrease in the SYM-H index with a magnitude up to several hundreds nT. This stage is called the *main phase*, which may last for about several hours. When the IMF becomes less southward or changes

to northward, the reconnection rate decreases to normal levels and the ring current strength starts to decay gradually with time. This is called the *recovery phase* and usually lasts for a couple of days. During geomagnetic storms, the increased reconnection rate and geomagnetic disturbances will intensify particle precipitation and auroral activity. The enhanced coupling between the solar wind and the magnetosphere will also increase the strength and coverage of the convection electric field in the high-latitude ionosphere. As a result, the polar cap and auroral zone can expand significantly to lower latitudes, which may lead to formation of high plasma density structures in the polar ionosphere.

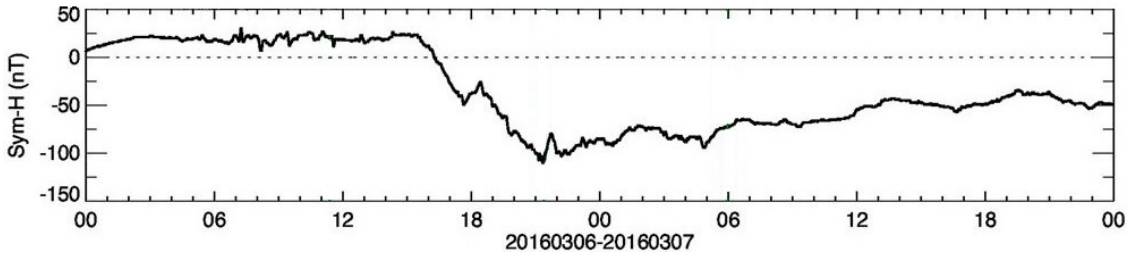

Figure 1.6: SYM-H index during a geomagnetic storm on March 6, 2016. From Zou et al. (2021).

1.2 High-latitude ionosphere density structures

1.2.1 Storm-enhanced density

The high-latitude ionosphere is usually characterized by low-density F region plasma as compared with the midlatitude sunlit region due to higher solar zenith angle and thus lower extreme ultraviolet (EUV) ionization. During geomagnetically disturbed periods, however, high-density thermal plasma on the dayside can be transported poleward by enhanced and equatorward-expanded high-latitude convection. Consequently, structures of dense F region plasma can be present in the subauroral region and even in the polar cap.

During geomagnetic storms, a ridge of significantly increased F region plasma density often forms near noon and postnoon magnetic local times (MLTs) at subauroral latitudes, which is termed as the storm-enhanced density (SED) (Foster, 1993), as shown in Figure 1.7. Under the effect of high-latitude convection, the dense plasma can extend northwestward toward the dayside cusp near noon and form a plume-like structure. The main contribution to the density increase within the SED is the imbalanced production and loss. That is, the plasma is lifted to higher altitudes with a lower recombination rate while the solar EUV production is still ongoing in the sunlit region. The lifting can be caused by the vertical component of $E \times B$ drifts, as a result of eastward penetrating electric fields at the subauroral and midlatitude regions where the magnetic fields are

not purely vertical (David et al., 2011; Deng and Ridley, 2006; Heelis et al., 2009; Zou et al., 2013, 2014; Zou and Ridley, 2016). Another important factor that affects plasma vertical motion is thermospheric wind. During storm periods, enhanced auroral activity and heating lead to equatorward neutral winds at subauroral latitudes, which push plasma upward along the magnetic field lines (Lu et al., 2012). The dynamic evolution of the SED is determined by the interplay between the electric fields and thermospheric winds (Zou et al., 2014). A more recent modeling study by Liu et al. (2016) showed that while the E × B drift is the dominant factor in generating the SED in the topside ionosphere, the thermospheric wind plays a more important role in SED formation in the lower altitude F region ionosphere.

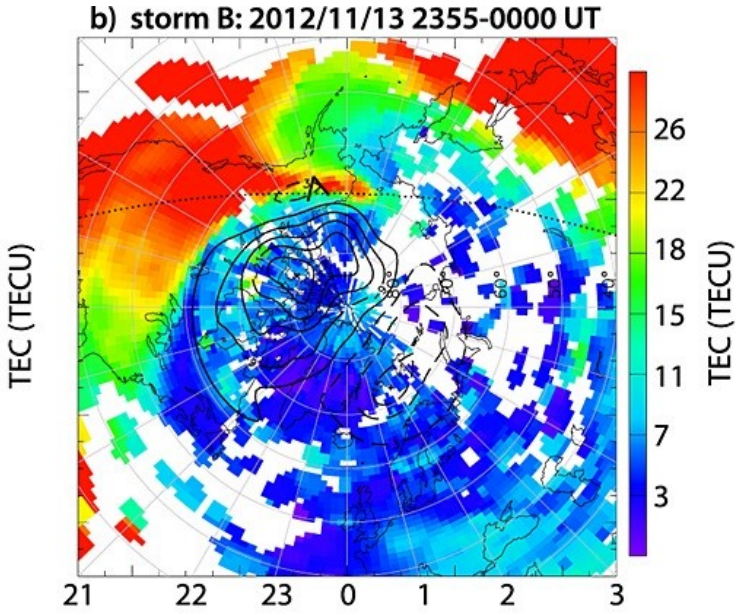

Figure 1.7: A polar view of TEC map showing a SED appearance during a geomagnetic storm on November 13, 2012. From Zou et al. (2014).

As the SED plume reaches the dayside cusp, the high-density plasma within the plume can be entrained into convection inflow region and then can enter the polar cap during periods of southward IMF (e.g., Thomas et al., 2013). A sustained transport of such dense plasma can form a large-scale transpolar structure from dayside to nightside known as the tongue of ionization (TOI) (Foster et al., 2005; Knudsen, 1974; Moen et al., 2008; Sato and Rourke, 1964; Zhang et al., 2015). Hosokawa et al. (2010) reported all-sky imager observations of a TOI during the storm on 14–16 December 2006, and showed its dynamic motion and mesoscale structures. Based on measurements from the Super Dual Auroral Radar Network (SuperDARN), they suggested that while the absence of large-scale convection pattern changes during periods of stable IMF allows a continuous structure of the TOI, small-scale flow channels near the cusp, probably associated with the dayside transient magnetic reconnection, can be responsible for the mesoscale structures within the

TOI. By combining vertical total electron content (TEC) maps derived from the Global Positioning System (GPS) data and SuperDARN convection pattern, Thomas et al. (2013) demonstrated the formation of a TOI from a SED plume under the effect of equatorward extended convection electric fields during the storm on 26–27 September 2011. They also observed enhanced HF backscatters associated with small-scale field-aligned irregularities within the TOI but not within the SED region, indicating that the small-scale structures are caused by modulations of electric fields near the dayside polar cap boundary.

1.2.2 Polar cap patch

Since polar cap patches were discovered by Weber et al. (1984) and then defined by Crowley (1996) as islands of high-density ionospheric plasma surrounded by plasma of half or less density in the F-region ionosphere (Figure 1.8), their generation mechanism and evolution process, as well as their impact on modern technology have been widely studied. Polar cap patches are generally viewed as the main cause for disturbances in navigation and communication signals in the polar regions (Basu et al., 1987, 1988) so understanding the formation of these high-latitude density structures is of significant practical importance. Studies have shown that the irregularity structure sizes within these patches can vary from hundreds of kilometers to tens of meters (Carlson, 2012), possibly due to gradient drift instability (e.g., Tsunoda, 1988); thus, they may disrupt transionospheric radio waves varying from high frequency (HF) communication to satellite ultra-high frequency (UHF) communication. The associated amplitude and phase scintillation may cause increased uncertainty or even loss of lock of the Global Navigation Satellite Systems (GNSS) receivers.

1.2.3 Generation mechanisms of polar cap patch

During periods of unsteady IMF By and Bz, the convection pattern near the dayside cusp can change dramatically (Heelis, 1984; Reiff and Burch, 1985; Burch et al., 1985; Ruohoniemi and Greenwald, 1998; Greenwald et al., 1999; Milan et al., 2000). As a result, as the SED plume is entrained into the convection flows, the large-scale plasma plume can break into smaller-scale patches, which are known as polar cap patches.

The creation of polar cap patches requires a source of high-density plasma and a mechanism to cut the large-scale plasma source into patches. While a good understanding of the sources has been obtained, the cutting mechanisms still remain controversial. As for sources, dayside midlatitude solar EUV-produced plasma and SED during storm times are generally believed to be the major reservoir for polar cap patches (Ren et al., 2018). In addition, soft particle precipitation can also become a potential source (Oksavik et al., 2006; Walker et al., 1999) but produce relatively weaker patches.

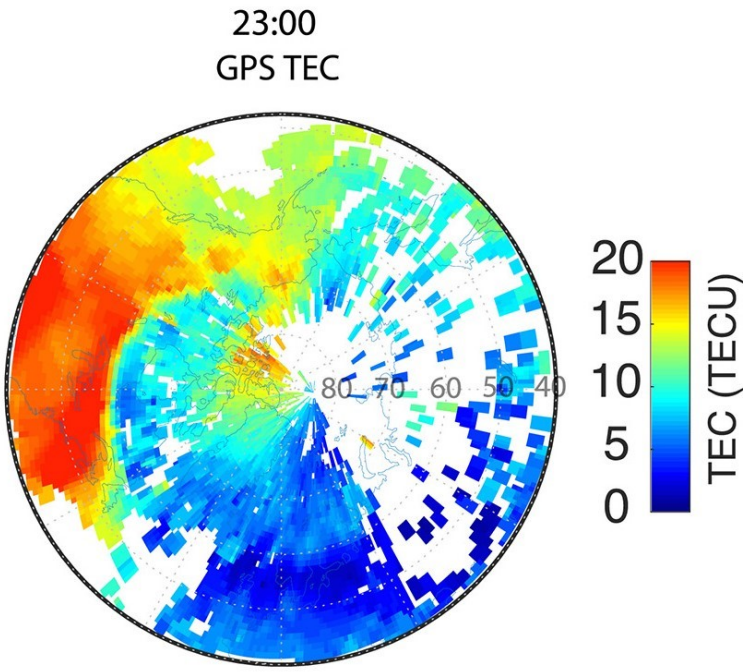

Figure 1.8: Example of a polar cap patch observed in the TEC map in the Norther Hemisphere during a geomagnetic storm on September 8, 2017. From Wang et al. (2019).

Besides the source, a mechanism to separate a portion of high-density plasma from the reservoir, for example, the SED plume, can produce patches. Several mechanisms have been proposed: temporal variation of the size of the ionospheric convection pattern (Anderson et al., 1988), transient dayside magnetic reconnection (Lockwood and Carlson, 1992), plasma fast flow channels causing enhanced recombination and low-density regions (Valladares et al., 1994, 1996), and IMF By reversals and cusp particle precipitation (Rodger et al., 1994). Imager and radar observations have shown that some patches associated with localized flow channels can originate from poleward moving auroral forms (Wang et al., 2016), which are usually seen as a result of transient reconnection, and the patch structuring processes have dependence on the IMF By condition (Zhang et al., 2011). Soft particle precipitation near the cusp can be another source of plasma density enhancement, which can then be isolated into patches by high-speed plasma flow channels associated with IMF By reversals (Rodger et al., 1994). Using numerical simulations, a more recent study by Wang et al. (2019) showed that intensified Birkeland Current Boundary Flows (BCBF) associated with enhanced westward drifting partial ring current can cut the SED into patches through increased frictional heating and recombination, without requirements for IMF shifts or dayside reconnections.

While many mechanisms have been proposed for the patch formation, it is not clear yet which produces most of the patches observed. In recent years, the development of observational instru-

ments provides great opportunities to put the proposed mechanisms to test.

1.2.4 Statistical study of polar cap patch

Previous statistical studies on the polar cap patches have used database from satellites (Coley and Heelis, 1995; Noja et al., 2013), meridian scanning photometers (MSP) (McEwen and Harris, 1996; Moen et al., 2007), and all-sky imagers (Hosokawa et al., 2009) to study their drift motion and occurrence frequency at different universal times (UT) and local times (LT). Based on ion density measurement taken by the Dynamic Explorer 2 spacecraft, Coley and Heelis (1995) developed an automatic technique to identify polar cap patches, followed by a statistical study of 281 patches showing a typical patch horizontal size of ∼300–400 km and an occurrence frequency peak around winter solstice and between ∼12–20 UT in the northern hemisphere (NH). Sojka et al. (1994) used Utah State University time-dependent ionospheric model to simulate the seasonal and UT variation of patch formation by modulating the IMF By component. Their results predicted an absence of patches between 8 UT and 12 UT and most intense patches between 20 UT and 24 UT at winter solstice in the NH. These model predictions were later confirmed by total electron content (TEC) observations (David et al., 2016). McEwen and Harris (1996) analyzed 523 patches observed by the meridian-scanning photometer at Eureka, Canada during winters from 1990 to 1994. They found that more patches are observed during local evening hours than the morning hours, and most of the patches occurred during or ∼1–2 hr after negative IMF Bz conditions. More recently, Noja et al. (2013) analyzed GPS TEC observations from the CHAMP satellite during 2001–2004 and reported higher patch occurrence at the dayside polar cusp and dusk side at ∼80°MLat. In their results, more patches were observed between 1400 MLT to 2100 MLT near the RISR site. Spicher et al. (2017) used Swarm satellites observation during 2013–2016 and showed that the patch occurrence rate was enhanced during local winter and reduced during local summer for both hemispheres. They also showed that more patches were observed in the dusk (dawn) sector for negative (positive) IMF By condition.

Hosokawa et al. (2009) investigated the motion of 561 individual polar cap patches observed from 2005 to 2007, using all-sky airglow imagers at Resolute Bay. They demonstrated that the dawn-dusk component of the patch's drift velocity is mainly controlled by polarity of the IMF By component. In addition, they found that the patches tend to drift towards dusk even when the IMF By equals 0, which is consistent with the fact that typically the dusk convection cell is bigger than the dawn cell due to the conductivity effect (Atkinson and Hutchison, 1978; Ruohoniemi and Greenwald, 1996, 2005). Moreover, Moen et al. (2007) used 8 years of data from MSP at Svalbard and observed 333 patches in 43 days that exited the polar cap during nighttime. They found a nearly symmetric bell-shape distribution of patch occurrence centered around 23:25 MLT, which

is likely caused by the tendency of patch motion from dawn to dusk. In a recent study by Zou et al. (2015), 97 patches were observed by an all-sky imager at Resolute Bay with simultaneous flow measurements by SuperDARN during the northern winter months from 2008 to 2012. Localized flow enhancements were found to be associated with $\sim$67% of the patches with a typical flow speed of 600 m/s, in favor of IMF By-dominated conditions.

1.3 Ion upflow

Over the last three decades, numerous studies have shown that ions from the Earth's ionosphere can be an important source of magnetospheric plasma (Chappell, 2015; Lotko, 2007; Moore and Horwitz, 2007; Welling et al., 2015; Yau and André, 1997). Ion upflow events in the F region and topside ionosphere can greatly influence the ion density and fluxes at higher altitudes, and thus may control to a great extent directly the ion outflow fluxes observed at high altitudes (Nilsson et al., 2008; Strangeway, 2005; Tu et al., 2007).

Observational characterization of the ion upflow occurrence rate can provide valuable information about the available source population as a function of solar wind and interplanetary magnetic field (IMF) condition, as well as the level of geomagnetic activity. Ion upflow and downflow events occurring in the F region and topside ionosphere have been studied using data from ground-based incoherent scatter radars (ISRs) (Buchert et al., 2004; Endo et al., 2000; Foster et al., 1998; Ji et al., 2019; Keating et al., 1990; Liu et al., 2001; Ogawa et al., 2009; Semeter et al., 2003; Zou et al., 2017a,b) and in situ satellite observations (Coley et al., 2006; Loranc et al., 1991; Redmon et al., 2010; Seo et al., 1997; Wu et al., 2000). The in situ satellite observations have large spatial coverage but limited coverage of altitude at any given time; while the ground-based ISRs, which are at fixed geographic locations, are able to provide altitude profiles of important plasma state parameters that can shed light on their formation mechanisms. In addition, some of the satellite observations mentioned above are actually vertical flows, while the ground-based ISRs can measure the field-aligned flows as well as the vertical flows.

The observed ion upflow exhibits considerable spatial and temporal variation. Based on satellite observations, the occurrence rate of upflow is generally larger than that of downflow in the auroral zone, but smaller in the polar cap. The downflow in the polar cap was observed using the DE-2 satellite and suggested to be ballistic return of outflowing ions (Loranc et al., 1991), which was later studied using simulations (Loranc and Maurice, 1994). Statistical studies of ion upflow were mainly conducted using the EISCAT radars at either Tromso (Endo et al., 2000; Foster et al., 1998; Keating et al., 1990) or Longyearbyen (Ji et al., 2019; Liu et al., 2001; Ogawa et al., 2009, 2019). The peak upflow occurrence rate was found in the premidnight sector near the Harang reversal region by EISCAT at Tromso ($\sim$66.7 MLat), while on the dayside at EISCAT Longyearbyen

(∼75.4 MLat). This effect of the MLat difference causing different occurrence rate statistics will be discussed in detail in Chapter 4.

1.4 Purpose of the dissertation

This dissertation include studies on the generation mechanism and statistical characteristics of polar cap patches using observational evidences from multiple instruments.

Chapter 2 presents the formation of a polar cap patch during the geomagnetic storm on October 13, 2016, using global TEC maps, SuperDARN high-latitude convection pattern and the Sondrestrom ISR observation. The comprehensive observational tools shed light on the controversial patch segmentation mechanism. This study shows the entire process of a patch being segmented from a SED base due to transient appearance of a fast flow, which was associated with dayside reconnection location changes based on the Sondrestrom ISR and SuperDARN observations. The roles of enhanced frictional heating and transport due to fast flows are discussed.

Statistical properties of the polar cap patches reveal key information regarding their formation mechanisms and propagation processes. Enhancements of the electron temperature within a patch compared with the surrounding region may indicate that the patch was generated by particle precipitation, while a decrease in the electron temperature may suggest that the plasma enhancement was generated on the dayside due to solar EUV radiation and then propagated to its current location. Observations have shown that the electron temperature within the dayside SED and SED plume is typically lower than the surrounding regions (Foster et al., 2005; Zou et al., 2013, 2014). Weber et al. (1984) observed approximately seven plasma patches with sizes of 800–1,000 km drifting antisunward using an all-sky imaging photometer and an ionosonde. Combined with simultaneous particle measurements taken by Dynamic Explorer 2 satellite, they showed that these patches were not generated locally but near the dayside auroral zone because of the absence of accelerated and structured electron precipitation. However, there have not been any systematic studies on the vertical profiles of patch plasma characteristics due to lack of instruments deep in the polar cap.

In Chapter 3, a statistical study is presented on the plasma characteristics of polar cap patches, utilizing data collected by the Canadian Resolute Bay ISR (RISR-C) throughout the whole year of 2016. RISR-C has the highest magnetic latitude among the current ISRs and is located deep in the polar cap, making it an ideal instrument to use for polar cap patch study. An automatic patch detection algorithm was developed to construct a collection of patch events, and then a superposed epoch analysis was conducted to show the typical vertical profiles of plasma density and temperatures measured within the patches at different MLT sectors in comparison with the overall typical profiles of the corresponding sector. Based on the results, the most dominant source of polar cap patches observed by RISR-C is discussed.

When the SED and polar cap patch encounter particle precipitation, large ion upflow fluxes can be generated (Zou et al., 2021), which can play an important role in ion outflow formation and plasma transfer from the ionosphere to the magnetosphere. Despite the first field-aligned ion upflow observations from the Chatanika ISR in Alaska (Bates, 1974), a comprehensive statistical study of upflow and downflow does not exist for the American sector. Neglecting the heat flow from the top of the ionosphere, the field-aligned component of the ionospheric ion velocity is affected by the thermospheric wind, ExB drift, and other vertical forces, including the pressure gradient and gravity. The magnetic field geometry affects the effectiveness of these forces, and their relative location to the auroral oval determines the corresponding magnetospheric region where the upflow and downflow map magnetically. Therefore, it is important to determine the geographical differences of occurrence rate of ion upflow and downflow, and test their dependence on season, IMF, and solar wind, as well as geomagnetic activity.

Chapter 4 contains a study using the Poker Flat ISR (PFISR) observation from 2011 to 2013 for a statistical study on the occurrence and plasma characteristics of ion upflow and downflow in the American sector. The correlation between the upflow occurrence and the solar wind, the IMF conditions and local magnetic disturbances were investigated. Unlike traditional ISRs, PFISR is part of the Advanced Modular ISR (AMISR) system with electronic pulse-to-pulse steering capability, which allows nearly simultaneous measurements of the plasma parameters in multiple look directions without physical movement of the radar antenna. Moreover, while ISRs are generally expensive to run, PFISR can operate semicontinuously in a low-duty cycle mode between user-requested high-duty cycle experiments, providing better data coverage throughout the year. Therefore, there are far more field-aligned profiles available from PFISR than those from other traditional ISRs for statistical analysis.

Chapter 5 summarizes the major conclusions drawn from the works in this dissertation and discuss a few potential projects for future work, including spherical harmonics reconstruction of TEC maps and machine learning of forecasting TEC maps.

CHAPTER 2

Direct Observation of Formation of a Polar Cap Patch Associated With Dayside Reconnection Driven Fast Flow

2.1 Introduction

Dayside solar-produced concentrated F region plasma can be transported from the midlatitude region into the polar cap during geomagnetically disturbed periods, creating plasma density irregularities like polar cap patches, which can cause scintillation and degrade performance of satellite communication and navigation at polar latitudes. In this chapter, we investigated the dynamic transport and multiscale plasma density structures of the high-latitude ionosphere during the geomagnetic storm on 13 October 2016, based on vertical GPS TEC maps, Active Magnetosphere and Planetary Electrodynamics Response Experiment (AMPERE) field-aligned current (FAC) maps, SuperDARN convection patterns, and Sondrestrom ISR.

During the storm main phase, a SED was formed within an extended period of strong southward interplanetary magnetic field (IMF) Bz condition. Total electron content (TEC) maps show that a polar cap patch was segmented from the SED plume. The Sondrestrom Incoherent Scatter Radar (ISR) was underneath the segmentation region and captured the dynamic process. It shows that the patch segmentation was related with a sudden northeastward flow enhancement reaching $\sim$2 km/s near the dayside cusp inflow region. The flow surge was observed along with an abrupt E region electron temperature increase, F region ion temperature increase, and a density decrease. The upstream solar wind and IMF observations suggest that the flow enhancement was associated with dayside magnetic reconnection triggered by a sudden and short period of IMF By negative excursion. Quantitative estimation suggests that plasma density loss due to enhanced frictional heating was insufficient for the patch segmentation because the elevated F region density peaking at $\sim$500 km made dissociative recombination inefficient. Instead, the patch was segmented from the SED by low-density plasma transported by the fast flow channel from earlier local time.

In Section 2.2, we give a brief introduction to the instruments and data sets that were used in the study. Section 2.3.1 outlines the soalr wind and IMF conditions of this geomagnetic storm event on 13 October 2016. Section 2.3.2 shows the ionosphere plasma density increase in midlatitude and subauroral regions and discusses how the dense plasma was transported into the polar cap during the storm main phase. Section 2.3.3 focuses on the formation of a polar cap patch during the event by carefully examining conjunction observations from the GPS TEC, SuperDARN convection, and Sondrestrom ISR. Finally, Section 2.4 summarizes the observations and conclusions. The work in this chapter has been published in Ren et al. (2020a).

2.2 Instrumentation and Data

2.2.1 GPS Total Electron Content

In this study, GPS TEC data are used to show large-scale plasma structures and their transport from midlatitude to high-latitude ionosphere. The GPS TEC data were obtained from the Madrigal database, and the detailed data processing method can be found in Rideout and Coster (2006) and Vierinen et al. (2016). The conversion from the LOS TEC values to vertical TEC is done by assuming a slab ionosphere at 350 km altitude, and only data points with elevation angle above 30° have been used. The TEC data shown in this paper have a temporal resolution of 5 min and spatial resolution of 1° × 1° in latitude and longitude with a 3° × 3° median filter applied to overcome the sparsity of data in the polar cap.

2.2.2 Super Dual Auroral Radar Network

We used SuperDARN convection maps to evaluate how the transport of ionosphere density structures is affected by the large-scale convection pattern during the storm period. As an international network of more than 30 HF radars, SuperDARN covers areas from midlatitudes to the polar regions for both hemispheres. The low-power HF radars operate continuously and measure the velocity of field-aligned plasma irregularities projected in the LOS of radar beams. The two-dimensional E × B velocity vectors can be derived when they are measured within the common field of view by two radars. A solution of high-latitude electrostatic potential field can be determined by combining all the velocity measurements and model results for areas where no observational data are available (Ruohoniemi and Baker, 1998). As a result, SuperDARN provides large-scale ionospheric convection maps on equal-area grids (100 km × 100 km) in the Altitude Adjusted Corrected Geomagnetic (AACGM) coordinate (Shepherd, 2014) every 2 min.

2.2.3 Active Magnetosphere and Planetary Electrodynamics Response Experiment

AMPERE FACs maps are used to indicate the location of the auroral oval and polar cap boundary and show expansions or contractions of the polar cap. Based on measurements of the magnetic field perturbations from the Iridium Communications constellation of more than 70 satellites at low-Earth orbits (∼780 km), AMPERE provides a global view of FACs. The orbits of satellites form 12 longitudinal planes roughly equally spaced by 2 hrs of local time, and satellites along the same track are separated by 9 minutes. The magnetic field perturbation data are calibrated and then used in spherical harmonic inversion (Green et al., 2006; Waters et al., 2001). The FACs are derived by taking the curl of the fitted perturbations and are provided in the AACGM coordinates on 1 hr MLT by 1° magnetic latitude (MLat) grids every 2 min. More detailed descriptions of the data product can be found in Anderson et al. (2014) and references therein.

2.2.4 Sondrestrom ISR

The ISRs are powerful ground-based instruments for ionosphere observations. By measuring the backscattered signals from electrons in the ionosphere, the ISRs have the ability to resolve the altitudinal profiles of electron density, electron and ion temperatures, and LOS ion velocity simultaneously. During this event, the Sondrestrom radar observed a fast flow channel associated with dayside reconnection when it was located near the dayside cusp, and in Section 2.3.3, we discuss the contribution of this fast flow channel to the formation of a polar cap patch. The Sondrestrom radar (67° N, 309° E, geographic; 74° N geomagnetic) was located near the west coast of Greenland and was operating under composite scans mode during this event. Under this mode, the radar was alternating between two scanning planes both roughly parallel to the magnetic meridian with one tilted slightly westward and the other tilted slightly eastward. Each scan takes ∼4 min and consists of 14 beams directions (Figure 2.7) with measurement ranges from ∼120 to ∼1,300 km, and the altitude resolution changes from ∼23 km in the E region to ∼65 km in the F region. By pairing the corresponding LOS velocity measurements at the same latitude and altitude from two successive scans (one eastward and one westward), an average F region two-dimensional horizontal velocity can be resolved for a given latitude. Finally, the resolved velocities are averaged in 0.25° latitude bins covering up from ∼65° to ∼80° MLat. In this study, for plasma density and temperatures, the latitude scans at a certain altitude were obtained by selecting the measurement at the closest altitude from each beam within a scan. In addition, data points of the resolved velocities with uncertainties larger than 250 m/s were dropped.

2.3 Observations

2.3.1 Solar Wind and IMF Condition for the 12–14 October 2016 Storm

Figure 2.1 shows the IMF (a–d) and solar wind (e–g) conditions, interplanetary electric field (h), AE (i), and SYM-H (j) indices from 12 UT on 12 October to 21 UT on 14 October 2016. The IMF and solar wind parameters were obtained from the NASA OMNI database, and they were observed by the WIND spacecraft and then time-shifted to the Earth's bow shock nose. This geomagnetic storm was a classic ICME-driven intense storm with clear shock, sheath, and magnetic cloud signatures. The storm was initiated with a storm sudden commencement (SSC) at 22:16 UT on 12 October, induced by the sudden enhancement of the solar wind dynamic pressure when the interplanetary shock in front of the ICME arrived. The solar wind speed jumped from ∼340 to ∼440 km/s (Figure 2.1e) at the shock and then decreased gradually. Typical ICME magnetic cloud signatures, including strong magnetic field, slow magnetic field rotation, low proton number density and pressure, can be seen throughout an extended period of ∼34 hr starting from 06:12 UT on 13 October and ending at ∼06 UT on 14 October. The magnetic cloud started with a sudden southward turning of the IMF Bz from +5 to -9 nT at 06:12 UT (dashed line in Figure 2.1), which kept decreasing since then and reached -21 nT at 16:41 UT on 13 October. During the same period, the IMF By started with negative values as large as -14 nT and then gradually turned to positive and reached +23 nT at 23:02 UT on 13 October. The extended period of strong southward IMF Bz caused an intense geomagnetic storm with the minimum SYM-H index reaching -113 nT and AE peaking at ∼2,000 nT.

2.3.2 General Ionosphere Responses to this Storm

Figure 2.2 shows GPS TEC maps (left) and AMPERE FAC maps (right) with high-latitude ionosphere convection contours from SuperDARN at five selected time cadences. These five times were right before (2.2a) and after (2.2b) the IMF Bz southward turning at 06:12 UT, 1.5 and 2.5 hr (2.2c and 2d) after the southward turning, and near the SYM-H minimum (2.2e) at 18:37 UT.

Figure 2.3 shows the time series plot of the IMF By and Bz (3a), reproduced for convenience, and the average MLat of the dayside (11–13 MLT) polar cap boundary (3b), which is approximated by the location of the peak Region 1 currents estimated from the AMPERE FAC measurements, similar to the method used in Clausen et al. (2013). Additionally, in Figure 2.3c, a keogram of the averaged GPS TEC near magnetic noon (11–13 MLT) is shown from 21 UT on 12 October to 12 UT on 14 October 2016.

From Figures 2.2a and 2.2b, it can be seen that the size of the convection pattern had expanded significantly at 06:14 UT comparing with that at 06:10 UT, as a result of the sudden southward

turning of the IMF Bz occurring at 06:12 UT, as indicated by the vertical dashed line in Figure 2.3. About 1.5 hr later, as shown in Figures 2.2c, 2.2d, and 2.3c, the dayside midlatitude ionosphere around noon showed significant plasma density enhancement from 07:52 to 08:52 UT, indicating a positive ionosphere storm occurred during this period. In Figures 2.2d and 2.3c, at 08:52 UT, a sharp TEC boundary with latitudinal density gradient as large as -1.8 TECU/degree can be seen at $\sim$65° MLat and $\sim$12 MLT, well aligned with the outermost contour of the fitted SuperDARN convection pattern and the Region 2 downward FACs. As the IMF Bz kept decreasing after 08:52 UT, the polar cap open-closed field line boundary and the convection pattern keep expanding further equatorward, as indicated in Figure 2.3b, and the sharp TEC boundary also moved equatorward accordingly. Starting from $\sim$11 UT in Figure 2.3c, midlatitude plasma with TEC of $\sim$12 TECU was transported poleward into the polar cap near noon from the sharp TEC boundary. The transport had been intermittent from $\sim$11 to $\sim$16 UT, and several polar cap patches were observed to form and enter the polar cap during this time period. After $\sim$16 UT, as the southward IMF Bz approached its maximum and the polar cap boundary reached as low as $\sim$62° MLat at noon, more continuous and larger-scale poleward transport of subauroral high-density plasma ($\sim$20 TECU) was present until $\sim$20:30 UT.

During this period, while a large-scale TOI structure of high-density plasma was present on the TEC map, as shown in Figure 2.2e at 18:36 UT, from the TEC keogram in Figure 2.3c, we can see density variations of smaller scales were embedded within this large-scale density structure. When the TOI was present during $\sim$15 to $\sim$18 UT, the sharp TEC boundary rapidly moved to lower latitudes from $\sim$50° to $\sim$40° MLat. After $\sim$21 UT, as the high-density source region remained below $\sim$40° MLat and the polar cap boundary started to retreat poleward, the plasma density dropped to a level even lower than it was at same UT but 24 hr earlier before the geomagnetic storm occured, as can be seen from Figure 2.3c, forming a deep midlatitude trough.

In Figure 2.3c we show that after the sudden southward turning of the IMF Bz, the polar cap started to expand to lower latitudes, and about 1.5 hr later, a positive ionosphere storm occurred, significantly increasing the subauroral plasma density. During $\sim$11 to $\sim$16 UT, however, the poleward transport of the plasma was intermittent and, as a result, several polar cap patches instead of a relatively uniform TOI were formed during this time period. From the SuperDARN convection pattern in Figure 2.2d, note that the convection inflow region during this period was shifted toward dawn side at around 10 MLT due to the negative IMF By condition, while the subauroral density enhancement was mainly located on the noon and postnoon MLTs. A sharp TEC boundary instead of a TOI was formed because the convection direction at the boundary near the high-density source region was mostly westward instead of poleward. It was not until $\sim$16 UT when the IMF By started to turn into positive that the inflow region shifted to where the enhanced density was and formed a large-scale TOI structure.

2.3.3 Polar Cap Patch Formation Near Cusp

In this section, we show in detail the formation of a polar cap patch. Figure 2.5 shows a direct observation of formation of polar cap patch in the GPS TEC map as a result of a fast flow appearance in the convection inflow region from 13:00 to 13:15 UT on 13 October 2016 shown in Figure 2.6.

In Figure 2.5, the ionosphere cusp location can be estimated by identifying the dayside convection inflow region from the SuperDARN convection pattern and between the merging region of the dawn and dusk Region 1 FACs from the AMPERE data. The TEC map in Figure 2.5a shows that, at 13:00 UT when the dayside cusp was near magnetic noon, the convection inflow region extended into the high-density plasma source region at $\sim$65° MLat and $\sim$12° MLT. As a result, the poleward convection flow near magnetic noon directly transported the high-density plasma from the source region into the polar cap. At 13:08 UT (2.5b), a convection flow kink appeared near magnetic noon as the convection inflow region shifted toward the dawn side, and the boundary of convection pattern slightly retreated to higher latitude, which is shown in from Figure 2.3b within the shaded area. The FACs pattern at the same time shows that the kink was near the upward and downward Region 1 FACs overlapping region and thus was the typical cusp location. After this convection flow configuration changed, plasma with lower density was transported to the polar cap, as seen at 13:12 UT in Figure 2.5c. And as a result, the high-density plasma moving poleward into the polar cap seen in 4a was cut off from its subauroral source region and became a polar cap patch. The flow kink shown in the SuperDARN convection map was derived based on real radar measurements, as shown in Figure 2.4.

As shown in Figure 2.6, this sudden flow direction change near cusp was also observed by the Sondrestrom ISR, which provides altitudinal profiles and latitude scans of multiple physical parameters. From Figures 2.5 and 2.6c, on a large scale, it can be seen that when the radar corotated into the dayside convection inflow region, the background flow direction changed gradually from eastward (blue) to northward (green). However, following a sudden southward IMF Bz decrease (2.6a, black curve) and further-negative excursion of the IMF By (2.6a, blue curve) from 12:35 to 12:50 UT, a channel of northeastward flow burst exceeding 2000 m/s can be seen at $\sim$13:00 UT (10 MLT) in Figures 2.6b and 2.6c, and it was moving poleward. The plasma in the background surrounding region showed dominantly northward motion with velocity of 500–1,000 m/s. Both E region electron (2.6d) and F region ion temperatures (2.6f) showed sudden enhancement associated with the fast flow channel. The E region electron temperatures increase indicated presence of energetic particle precipitation, and the F region ions were heated by frictional heating within the fast flow. Meanwhile, as shown in Figures 2.6e and 2.6g, a distinct area of low density and cold electron temperature in the F region was also observed associated with the fast flow channel.

The observed plasma density decrease could be caused by the fast flow through two possible ways. The first one is the increased recombination rate due to frictional heating within the fast

flow. The other one is low-density plasma nearby transported by the flow channel into the radar field of view. In order to determine which factor played a more dominant role in this case, careful examinations on the measurements from individual radar scans are required.

In Figure 2.7, the Sondrestrom ISR measurements from three consecutive eastward scans show plasma properties before, during, and after the period that the fast flow appears, respectively. During the first scan from ∼12:57 to ∼13:01 UT, the radar had seen hot and dense solar EUV-produced plasma with density reaching $\sim 10^{11.5}$ m^{-3} (Figure 2.7a) and electron temperature over 2,500 K (2.7d), throughout the radar field of view from 65° to 80° latitude. The height of peak electron density (hmF2) was lifted up to ∼500 km altitude, most likely due to the upward component of the E × B drift as the plasma is moving poleward on the dayside, which can be seen from the radar ion LOS velocity measurements (2.7j). Within 10 min after the first scan, starting from ∼13:07 to ∼13:11 UT, a structure of cold plasma with significantly lower density $\sim 10^{10}$ m^{-3} and electron temperature below 1,000 K appeared in the middle of the radar field of view (6b and 6e). The electron density profiles within the structure peaked at ∼250 km altitude. The most upward beam in the middle, which also pointed slightly toward the east as shown in the bottom right panel of Figure 2.7, had seen strong LOS ion velocity over 1,000 m/s away from the radar (2.7k), indicating the presence of eastward fast flow overhead. The drastic differences in the plasma density, temperature, and hmF2 are strong evidence indicating that the low-density structure was transported into the radar field of view from a different plasma source than the high-density plasma seen during the first scan, most likely from the polar cap on the dawn side according to TEC maps shown in Figure 2.5.

In addition, quantitative estimations of the density decrease caused by the frictional heating have been conducted and the results are shown in Figure 2.8. By averaging the measurements taken from the nine beams above 71.7° MLat in each scan, the altitudinal profiles of ion temperature and electron density were calculated for 12:57 and 13:07 UT, as shown in Figures 2.8a and 2.8b, respectively. Besides, the density profiles of neutral N_2 provided by the Madrigal database using the MSIS 2000 model are also shown in Figure 2.8c, which is required for the estimation. In Figure 2.8d, we demonstrate a comparison between the total density decrease measured by the Sondrestrom ISR from 12:57 to 13:07 UT and the estimated density decrease caused by the frictional heating.

Although the enhanced ion flow speed leads to noticeable ion-neutral frictional heating at altitudes below 250 km (Figure 2.8a), for altitudes above 300 km, the frictional heating was not sufficient to account for the density decreases observed, mainly due to the lack of neutrals above 300 km. At 12:57 UT, according to Figure 2.6b, the mean plasma flow speed at ∼72° MLat was ∼1.3 km/s, while at 13:07 UT the flow speed rapidly increased to ∼2.3 km/s, creating enhanced frictional heating through ion-neutral collisions, which increased the ion temperature within the

next 10 min mainly below ∼250 km, as can be seen in Figure 2.8a. Since the neutral density was much higher than the ion density below ∼600 km, the time scale for the neutral temperature to increase was much longer, so we can assume that at 13:07 UT, the neutral temperature remained the same as the ion temperature at 12:57 UT. For altitudes between ∼200 and ∼700 km, the dominant ion species is O^+. Based on the equations given by St.-Maurice and Torr (1978), as a result of the elevated ion temperature and enhanced flow speed, the charge exchange rates between O^+ and N_2 and between O^+ and O_2 could have increased by up to ∼250% and ∼80%, respectively. Description of the calculations in detail can be found in Ren et al. (2020a). Because the dissociative recombination of the resulting NO^+ and $O_2{}^+$ was significantly faster than radiative recombination of O^+, we can estimate the density decrease by computing how much O^+ had been lost by charge exchange within 10 min. As shown in Figure 2.8d, the frictional heating could only account for the density decrease below ∼300 km altitude, while above ∼300 km, where the largest density decrease is observed, the contribution from the enhanced frictional heating was several order of magnitudes lower than the observed values. This is mainly because the neutral density, shown in Figure 2.8c, decreases exponentially with altitude. In additional, considering that the neutrals could also be heated to some extent and lead to N_2 and O_2 density increase as a result of thermosphere expansion, we also did a similar estimation with neutral density doubled, but the results were not affected much. This estimation suggests that enhanced frictional heating was not the dominant effect that accounts for the appearance of the low-density structure seen above ∼300 km and also the low TEC structure seen in the TEC map. According to the analysis above, it can be concluded that the low-density structure observed was transported by the northeastward fast flow channel from a nearby region on the dawnside and the impact of frictional heating was limited to altitudes below ∼300 km.

2.4 Discussion

This result shows an interesting contrast with the scenario demonstrated by Wang et al. (2019), in which the frictional heating-induced density decrease can account for the segmentation of a SED plume. In both cases, low-TEC regions were observed in the TEC map during the segmentation process; however, a key difference that the two-dimensional TEC maps cannot show is that the plasma vertical density profiles in these two events peaked at very different altitudes. As shown in the Figure 2.5d of Wang et al. (2019), the density profile peaked at ∼300 km at $\sim 4 \times 10^{11}$ m^{-3} when the boundary fast flow between the Regions 1 and 2 FACs was present, while in our case, the observed SED plume had been significantly lifted and the maximum density was found reaching $\sim 1.9 \times 10^{11}$ m^{-3} at ∼500 km at ∼12:57 UT. Since the neutral density drops with altitude exponentially, there are over 2-3 orders of magnitude less neutrals at 500 km for the ions (mostly

O+) to react with than those at 300 km, making the frictional heating a lot less effective in raising the recombination rate and decreasing the plasma density. To show the importance of hmF2 in affecting the density loss due to frictional heating, we hypothetically lowered the density peak from ∼500 to ∼300 km while keeping other parameters unchanged, and our estimation showed that the frictional heating could cause a $\sim 1.3 \times 10^{11}$ m^{-3} density decrease within 10 min, ∼2-3 orders of magnitude larger than it did at ∼500 km. In conclusion, the fact that the SED plume had been lifted to a much higher altitude (with hmF2 ∼500 km) was the main factor that made frictional heating less effective for patch segmentation in this case. Using numerical model, Zou and Ridley (2016) found that SED plasma originating from different local time sectors could have different characteristics, such as NmF2 and hmF2, implying different segmentation mechanisms may exist for SED plasma originating from different local times.

Detailed examinations of sequence of the observations suggest the fast flow surge, and the associated plasma characteristics were ionospheric signatures of magnetic reconnection. At first, following the sudden IMF By negative excursion from ∼12:40 to ∼12:50 UT (Figure 2.6a), an initial E region electron temperature increase can be seen at ∼12:52 UT near 72° MLat (Figure 2.6d), which was due to precipitating particles streaming from the reconnection site. At this latitude, the northeastward flow surge exceeding 2 km/s appeared at ∼13:00 UT. Then at ∼13:04 UT, significant ion temperature increase at ∼350 km altitude was observed, due to frictional heating within the fast flow or particle precipitation from the reconnection site. This series of observations matched very well with the expected signatures of magnetic reconnection reported by Carlson (2004). Carlson et al. (2006) showed the first observation of these signatures from the EISCAT Svalbard radar (ESR) and concluded that it validated the Lockwood and Carlson (1992) mechanism, in which reconnection driven convection flow surge transiently injects corotating subauroral high-density plasma into the polar cap. In their study, under a positive IMF By condition, a northwestward flow surge carrying subauroral plasma into the polar cap was seen at ∼10 MLT, similar to the local time of our case. The northeastward fast flow we observed was consistent with the negative IMF By condition. On the contrary, in our case it was the low-density rather than high-density plasma that is carried by the flow surge, being injected toward noon into the middle of a stream of high-density plasma that was previously transported into the polar cap a few minutes before (see Figure 2.5). Therefore, the transient flow surge in this case only acted as a segmentation mechanism (with little frictional heating effect). Essentially, the physical process here was most likely the same as that described in the Lockwood and Carlson (1992) mechanism but happened in a different ionosphere precondition (mostly plasma density distribution).

To generalize, a similar scenario of polar cap patch formation as the one discussed in this study requires the following: (1) A structure of high-density plasma lifted in altitude is present in the polar cap near the cusp, which could be either a small-scale stream of plasma that just entered the

polar cap from the SED, or a preexisted large-scale TOI; (2) a reservoir of low-density plasma in adjacent regions, such as non-SED high-latitude plasma or the main polar cap trough; and (3) a fast flow channel (most likely driven by dayside reconnection) from the low-density reservoir to the high-density structure. While for those lifted density structures (hmF2 $\sim$500 km), both the low-density reservoir and flow channel are required; for those density structures without being lifted (hmF2 $\sim$300 km), the fast flow channel alone can create segmentation via frictional heating.

2.5 Summary and Conclusions

In this chapter, we investigated the dynamic structuring of high-density plasma from a dayside subauroral SED to the polar cap during a geomagnetic storm on 13 October 2016, based on observations from the GPS TEC maps, AMPERE FACs maps, SuperDARN convection patterns, and Sondrestrom ISR. During the storm main phase, a sudden southward turning of the IMF Bz triggered an expansion of the polar cap and a positive ionosphere storm, which created a strong convection pattern and significantly increased the subauroral plasma density as the SED at post-noon MLTs. However, the dayside convection inflow region was shifted toward the dawnside at around 10 MLT due to the negative IMF By condition, unfavorable for continuous transport of the SED plasma into the polar cap and formation of TOI. Instead, a dayside magnetic reconnection-driven fast flow channel, triggered by a sudden and short period of IMF By negative excursion, transported low-density cold plasma from earlier local time into the convection inflow region and segmented a group of SED plasma into a polar cap patch. Quantitative estimations of the effect of enhanced frictional heating due to the fast flow have been conducted. However, while increased ion temperature was present within the fast flow, it was not sufficient to deplete the SED plasma down to observed values above 300 km, mainly because the F region peak in the SED structure had been lifted to altitudes $\sim$500 km, where the neutrals were lacking, and thus, the loss due to the enhanced dissociative recombination was not efficient to deplete the SED plasma. This work presents a comprehensive suite of observations that show the detailed formation process of a polar cap patch and provide supporting evidence for the reconnection-driven segmentation mechanisms proposed in previous studies (Lockwood and Carlson, 1992; Anderson et al., 1988). Distinctions from the traditional reconnection segmentation mechanism is also suggested and discussed.

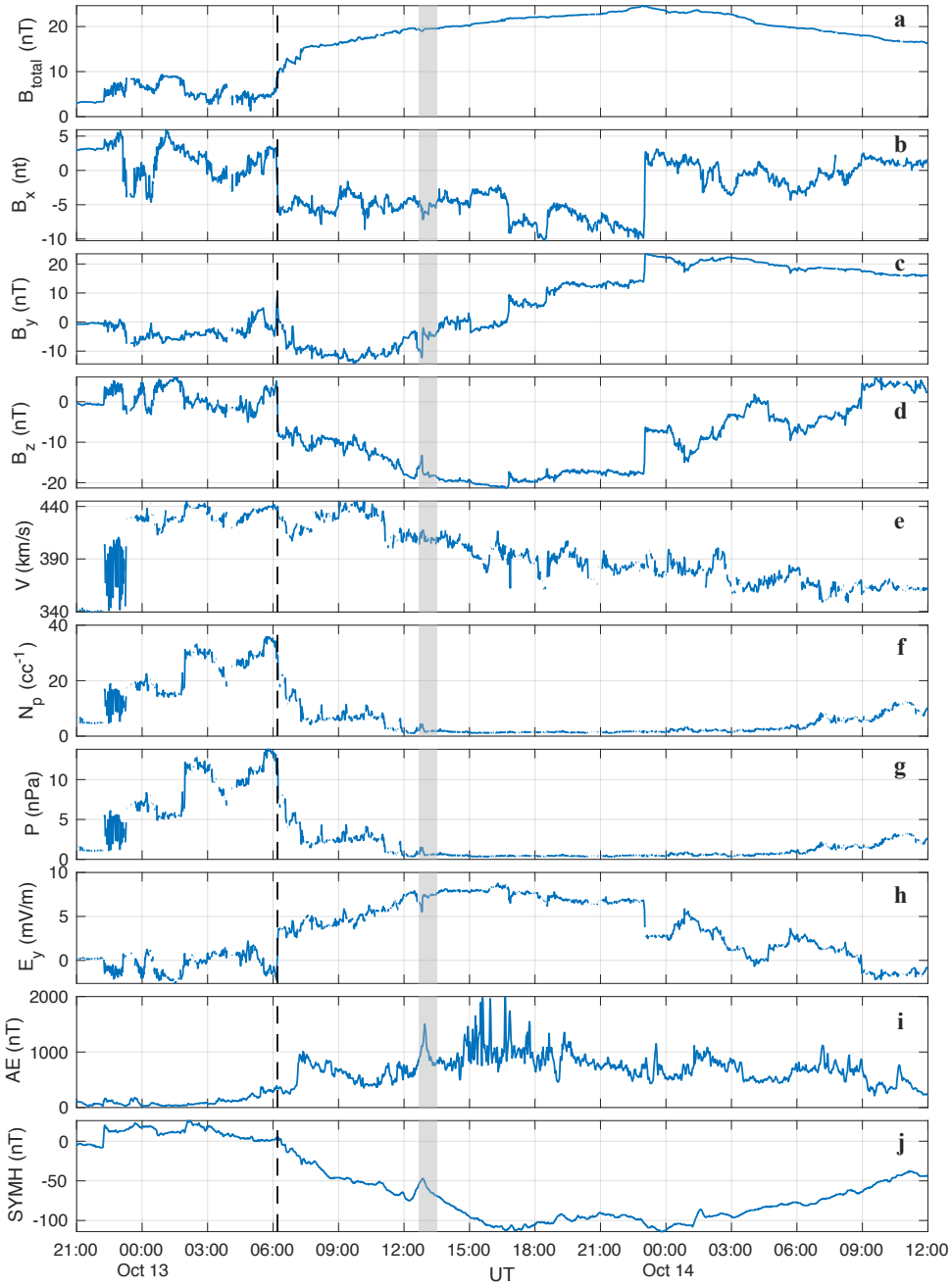

Figure 2.1: Solar wind and IMF conditions, provisional AE index and SYM-H component from 12 UT on 12 October to 21 UT on 14 October 2016, obtained from the NASA OMNI database. The geomagnetic storm is initiated at the arrival of an interplanetary shock and then enters the main phase as the solar wind presents a clear magnetic cloud structure. The shaded area marks the period when the generation of the polar cap patch was observed in TEC maps.

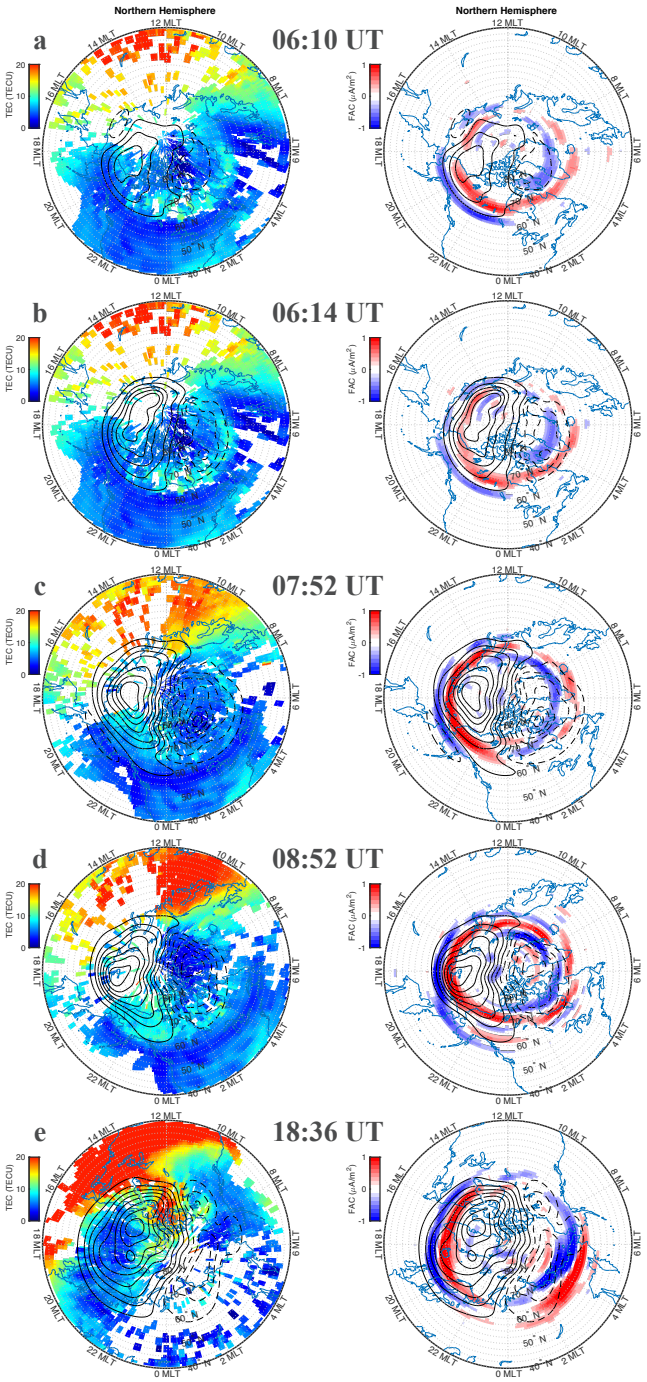

Figure 2.2: GPS TEC maps from the Madrigal database (left) and AMPERE FACs maps (right) with high-latitude ionosphere convection pattern from SuperDARN overlaid at (a) 06:10 UT, (b) 06:14 UT, (c) 07:52 UT, (d) 08:52 UT, and (e) 18:36 UT. The outermost dashed (solid) contour of the convection cell corresponds to 3 kV (-3 kV) equipotential line, and the interval between two contours is 6 kV. The size of the convection pattern had expanded significantly at 06:14 UT comparing with that at 06:10 UT, as a result of the sudden southward turning of the IMF Bz occurring at 06:12 UT. Dayside midlatitude ionosphere around noon showed significant plasma density enhancement from 07:52 to 08:52 UT as an ionosphere storm entered the positive phase. Magnitude of the FACs system also increased comparing (c) and (d) with (a) and (b).

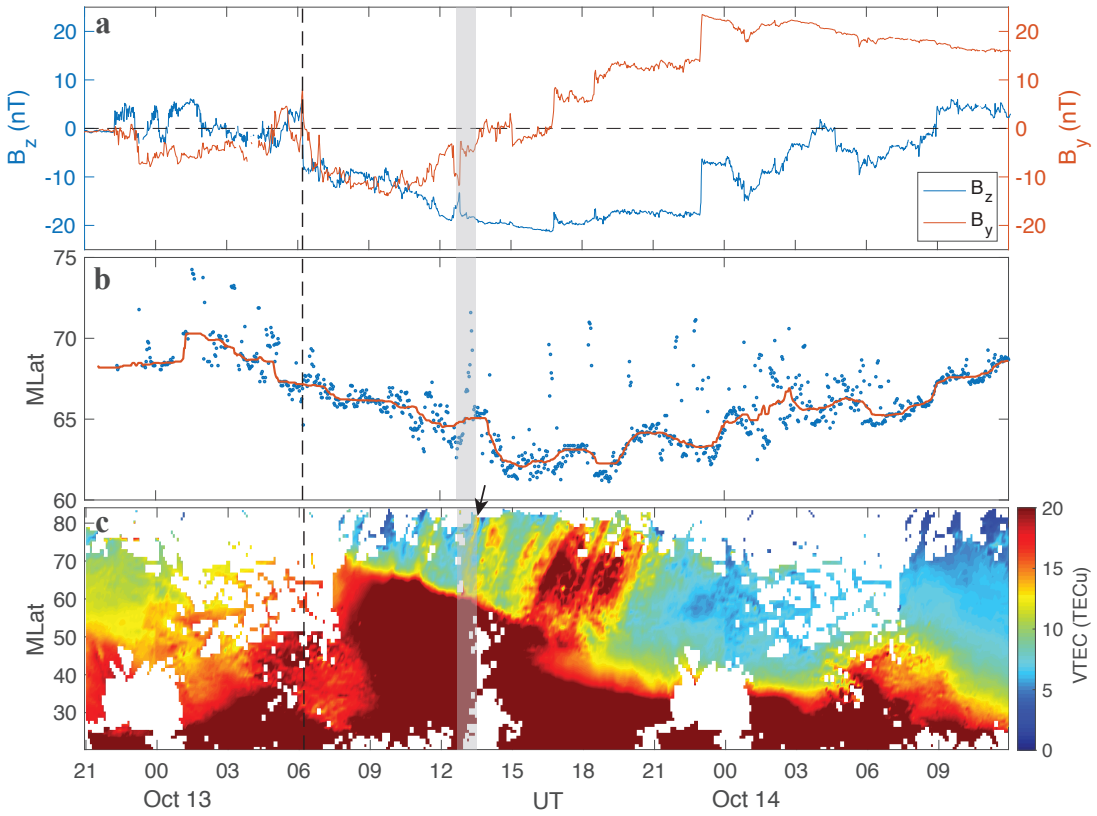

Figure 2.3: (a) IMF By and Bz from the NASA OMNI database. (b) The blue dots show estimate Region 1 FACs average latitude between 11 and 13 MLT for every 2 min, as an approximation for the latitudes of polar cap boundary. The red curve is obtained by applying median filter with a 50-point window. (c) GPS TEC keogram between 11 and 13 MLT from the Madrigal database, from 21 UT on 12 October to 12 UT on 14 October 2016. The vertical dashed line marks the onset of a southward IMF Bz turning at 6:12 UT. The shaded area indicates the period of a polar cap patch formation at ∼13 UT, as discussed in Section 2.3.3. The arrow marks the trace of the patch in the TEC keogram.

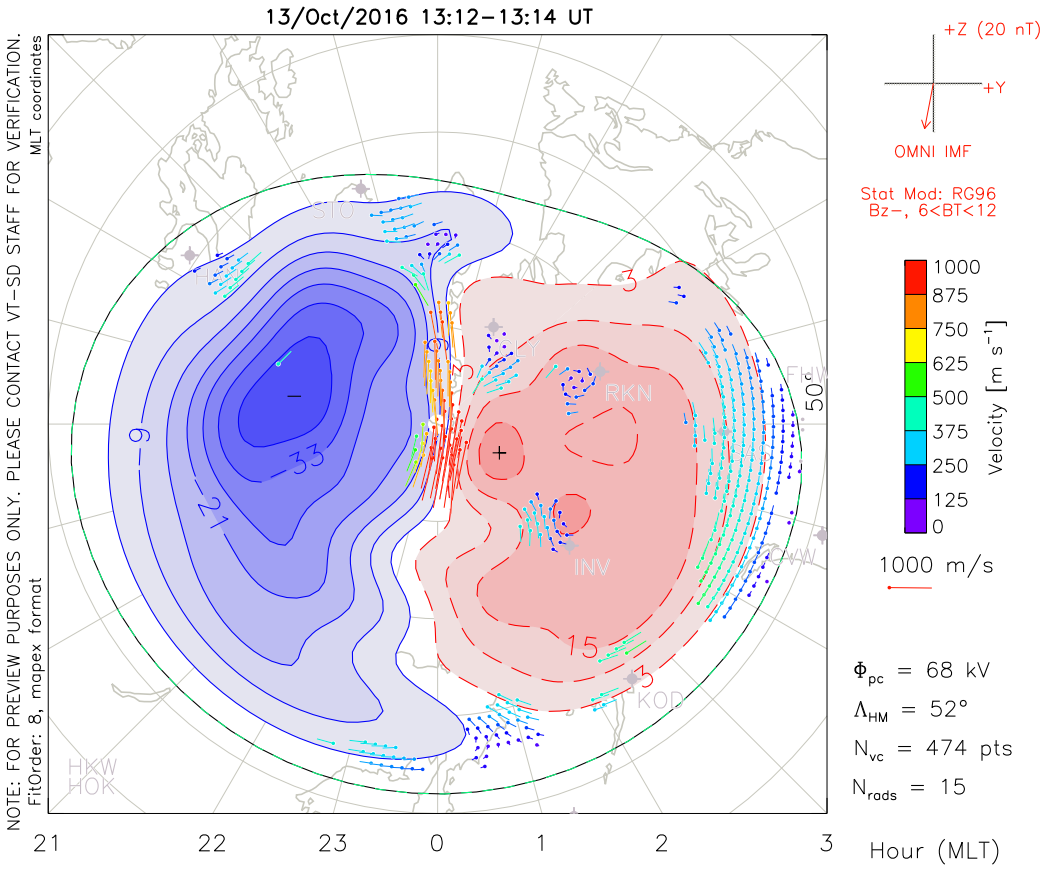

Figure 2.4: The SuperDARN convection map with true velocities derived from real radar measurements plotted as vectors. This figure is made by using the plotting tools on the SuperDARN website.

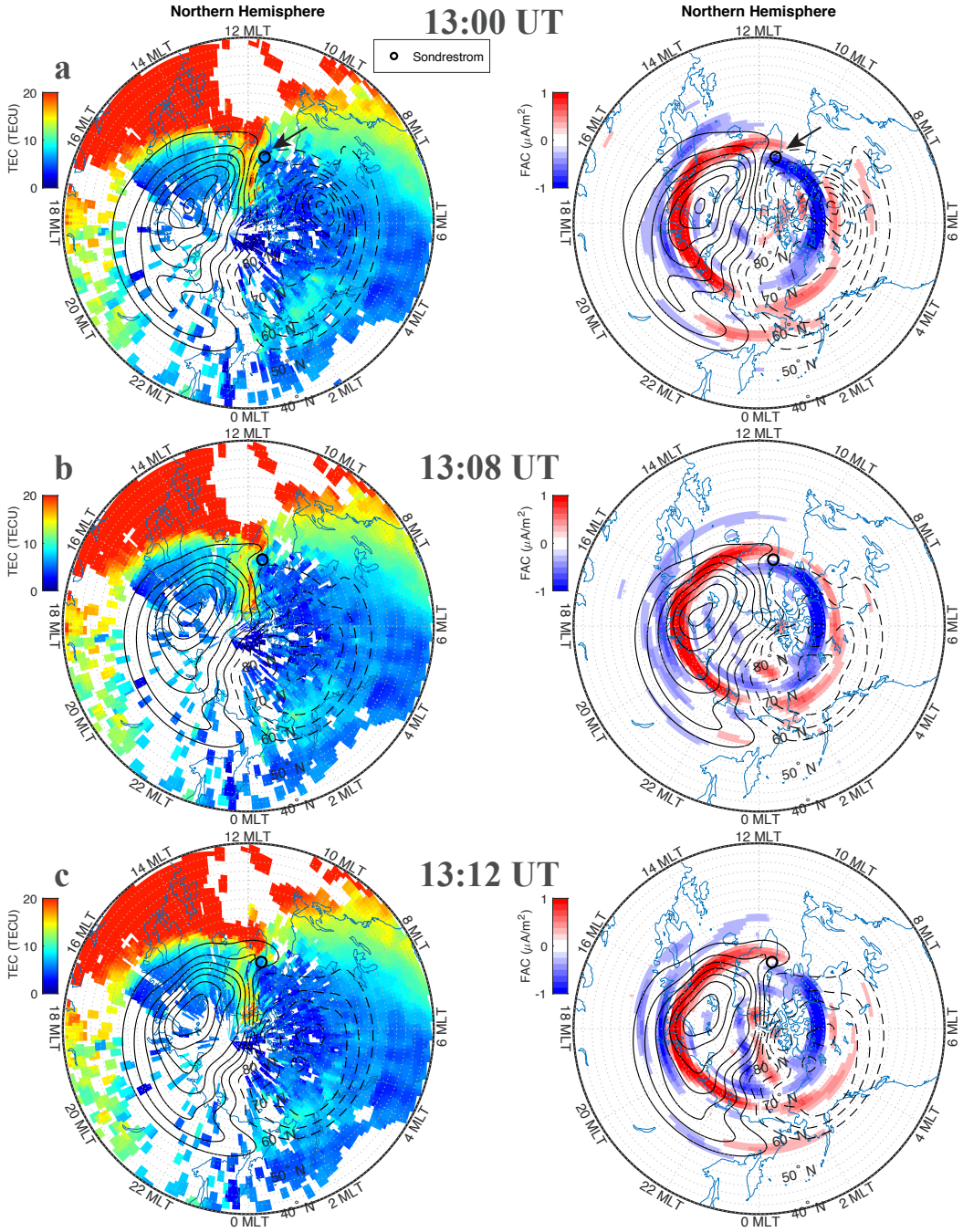

Figure 2.5: GPS TEC, AMPERE FACs maps, and SuperDARN convection patterns at 13:00 UT (a), 13:08 UT (b), and 13:12 UT (c) on 13 October 2016. The Sondrestrom ISR, marked by the black circle, was located near the dayside convection inflow region around 11 MLT. From the TEC map, it can be seen that high-density plasma moving poleward into the polar cap was segmented into patches due to the sudden convection direction change near the inflow region. SuperDARN had real radar measurements near the convection kink, as shown in Figure 2.4.

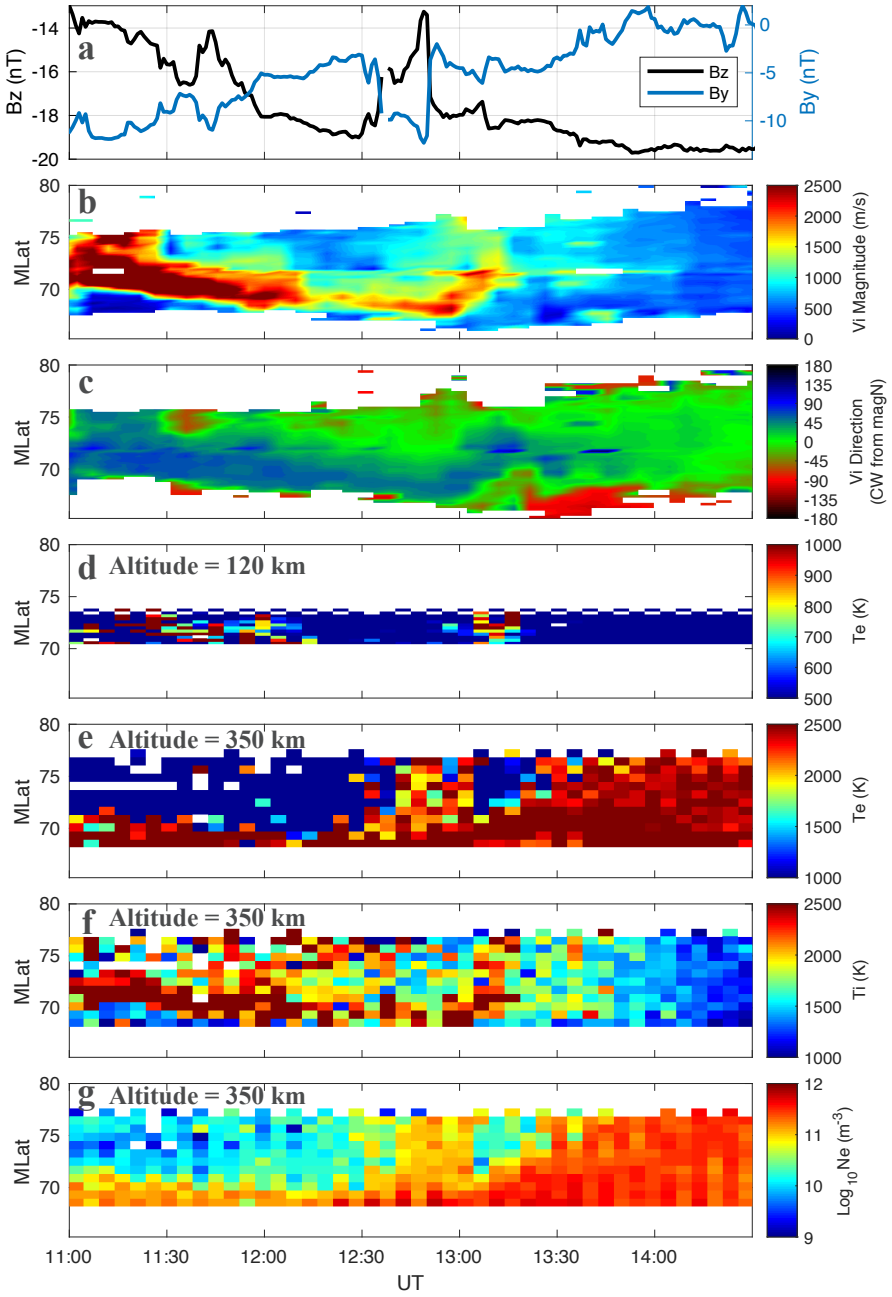

Figure 2.6: (a) The solar wind IMF By and Bz components from the OMNI database. Sondrestrom ISR latitude scans of plasma convection velocity (b) speed and (c) direction (zero starts from the magnetic north and rotates clockwise for positive values), electron temperature at (d) 120 km and (e) 350 km altitude, (f) ion temperature, and (g) electron density at 350 km altitude from 11:00 to 14:30 UT on 13 October 2016. For the Sondrestrom ISR, MLT = UT – 3 hr. A northeastward fast flow channel as strong as 2 km/s could be seen at around 13 UT (10 MLT), and it was moving toward higher latitudes, while the plasma in the background showed northward motion with velocity of 500–1,000 m/s. Electron precipitation at 120 km, ion temperature increase, electron temperature, and density decrease at 350 km were observed along with the fast flow channel.

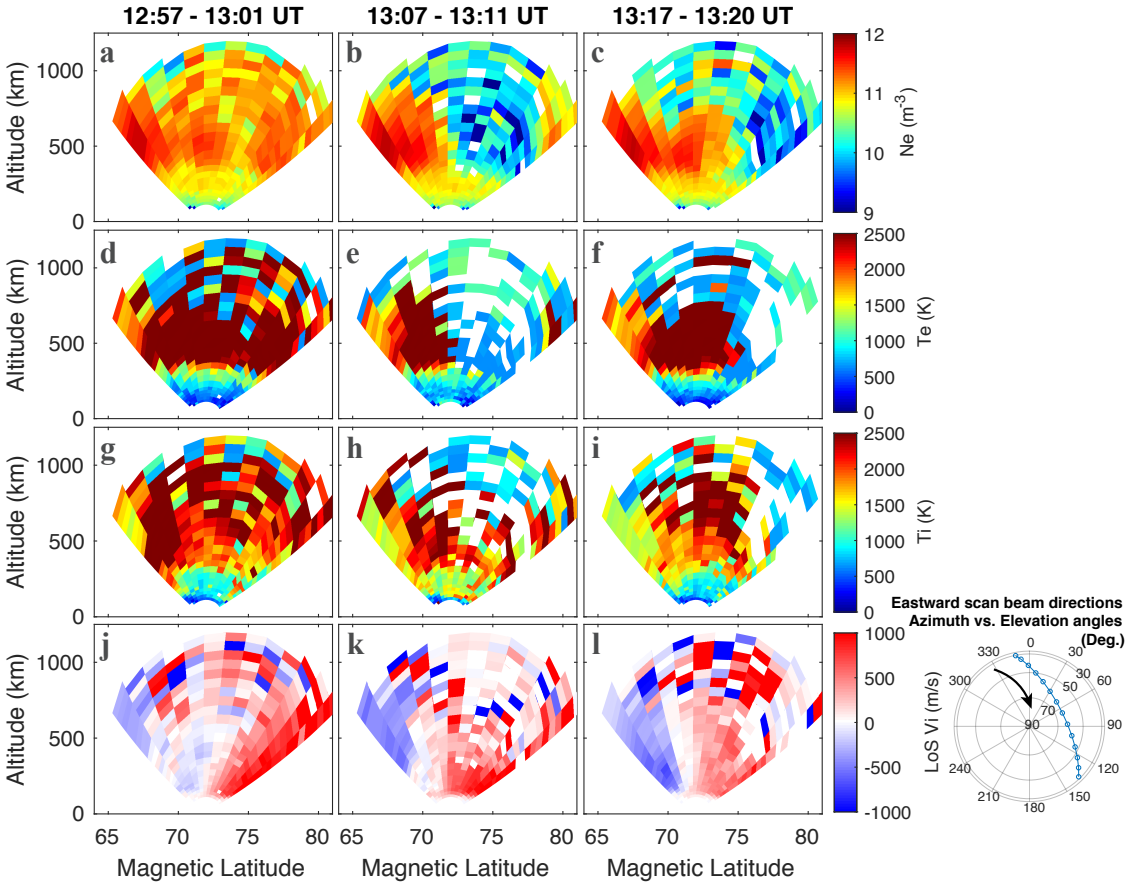

Figure 2.7: Sondrestrom ISR measurements of (a–c) electron density, (d–f) electron temperature, (g–i) ion temperature, and (j–l) ion LOS velocity (positive values indicate direction away from the radar) from three consecutive eastward scans before, during, and after the density decrease at ∼13:10 UT, when the fast flow was observed. The pointing directions of the radar eastward scan (always from the north to the south) is shown at the bottom right panel.

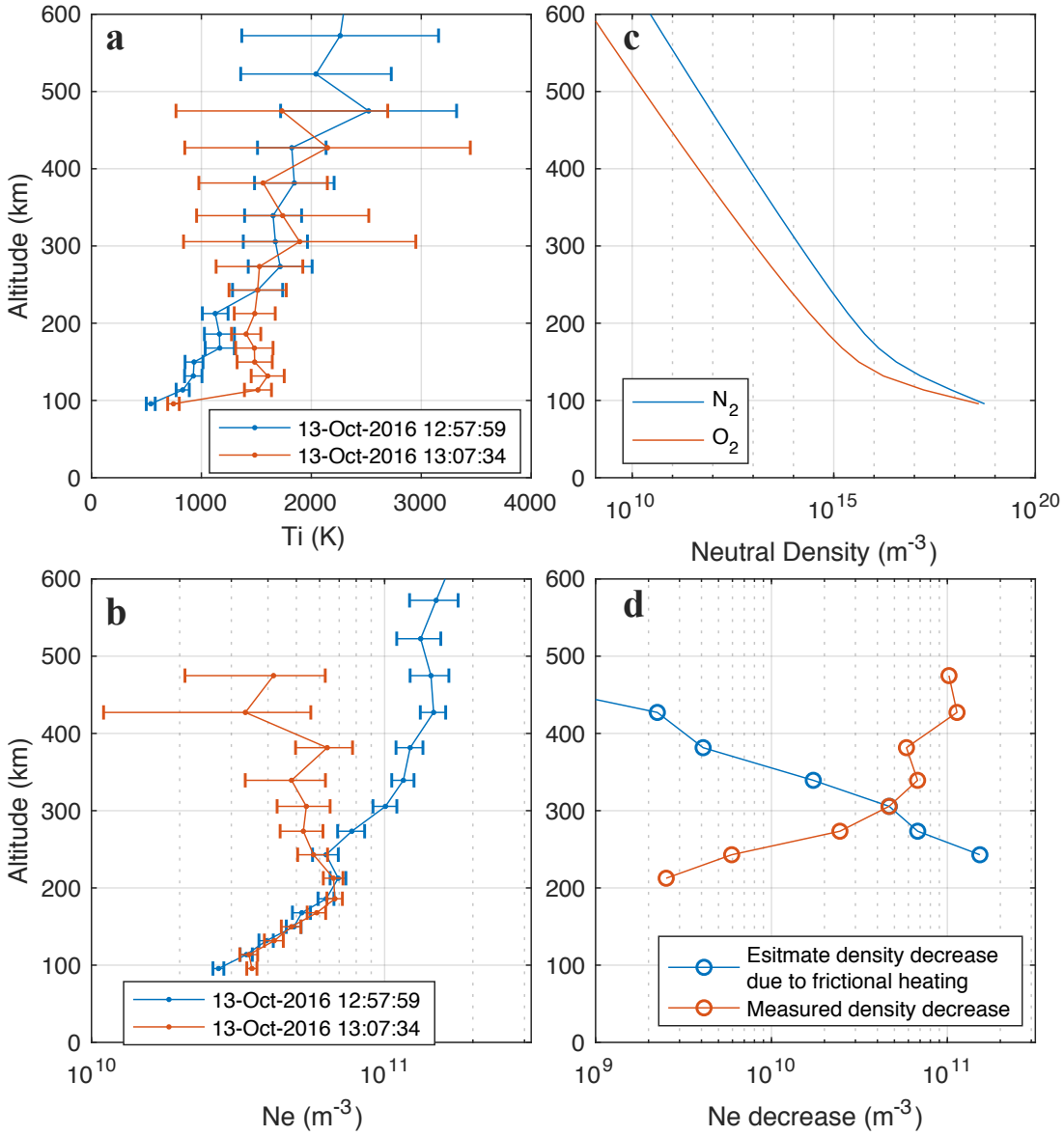

Figure 2.8: (a and b) Altitude profiles of ion temperature and electron density measured by Sondrestrom ISR eastward scans at 12:57 and 13:07 UT. The altitude profiles were calculated by averaging the measurements from the nine beams above 71.7° MLat in each scan. (c) N2 density profile provided by Madrigal based on MSIS 2000 model. (d) Estimate plasma density decrease caused by frictional heating using formulations in St.-Maurice and Torr (1978), compared with total density decrease in observation from 12:57 to 13:07 UT, as shown in (b).

CHAPTER 3

Statistical Characteristics of Polar Cap Patch Observed by RISR-C

3.1 Introduction

Polar cap "patches" are ∼100 to 1,000 km islands of high-density plasma at polar latitudes, which can cause scintillation to communication and navigation signals. While a good understanding of patch size and occurrence distribution in terms of season and time (UT or MLT) has been developed by previous statistical studies, more detailed statistical plasma characteristics within the patches, such as their vertical profiles of density and plasma temperature, were not well known until this study. Fortunately, the newly deployed Resolute Bay Incoherent Radar provides such a capability. Perry and Maurice (2018) used a patch detection algorithm on the northern face of the Resolute Bay Incoherent Scatter Radar (RISR-N) data measured during 5 days each in March and December in 2010, and reported distributions of F-region plasma density and temperatures of the patches, but the statistical profiles within the patches were not studied.

In this chapter, based on 7-month measurements taken by the Canadian component of the RISR radars (RISR-C) (Gillies et al., 2016) in 2016, we developed an automatic algorithm to identify the polar cap patches and constructed a database of 437 patches. We then studied the MLT distribution of patch occurrence frequency and also conducted a superposed epoch analysis on altitude profiles of plasma density, temperature and ion fluxes measured within the patches. The work presented in this chapter has been published in Ren et al. (2018).

3.2 Instrumentation and Data

3.2.1 RISR-C Database

Resolute Bay is currently the highest geomagnetic latitude (82.43°) ISR station (74.73° N, 94.91° W geographic) in the world, making it an ideal place for polar cap patch observation. The RISR-C

database used in this study contains measurements from January to March and from September to December in 2016, with a total observational time of ∼1,100 hr. During the 7 months, the radar operated for several selected days in each month. All the RISR-C data from 2016 were collected during coordinated experiments with RISR-N, but only RISR-C data were used in this chapter because we aim to study the patch profile along the field-aligned direction, which is within the RISR-C field of view and outside the RISR-N field of view. In each run, the radar provides measurements of electron density, electron and ion temperature, and ion LOS velocity from ∼100 to ∼700 km in altitude, with a spatial resolution of ∼24 km (long pulse mode) and a time resolution of 1 min. Raw electron density directly obtained from power without range integration or correction for measured electron and ion temperature ratios is also available with a spatial resolution of ∼3 km. In addition, since RISR uses a phased array of thousands of antenna element units to enable almost simultaneous multiple-beam measurements, its beam configuration can be changed on demand for each operation. As a result, there are in total four different beam configurations throughout the 7-month data set that were used in this study. In order to interpret the LOS velocity and other parameters in a straightforward and meaningful way, for each beam configuration we choose to use data obtained from the beam pointing most closely to the field-aligned direction, which is nearly vertical (169.09° azimuth, 86.41° elevation) at Resolute Bay. The beams that have been used in this study are 83.0° elevation and -157.0° azimuth, 85.0° elevation, and -157.0° azimuth and 90.0° elevation. Projections of ISR K vectors of these three beams on the field-aligned direction are around 0.997, 0.998, and 0.999, respectively.

3.2.2 Patch Identification Technique

Using the time series data of electron density observed by RISR-C, we developed an automatic algorithm to identify the patches and constructed a database of 437 patches. In the identification algorithm, a set of criteria listed below has been applied to effectively distinguish the features of a patch from other density enhancements shown in the data.

1. A patch should appear as a density peak in the F-region with a minimum prominence of $log_{10}(2)$ in log scale, according to the classical definition that a patch has at least double density of its surrounding plasma (Crowley, 1996).

2. A patch should last at least 3 min but no more than 2 hr in the radar observation, given a typical patch size range of ∼100–1,000 km (Coley and Heelis, 1995) and a patch convection velocity range of ∼150–500 m/s that Hosokawa et al. (2009) reported at Resolute Bay. A density enhancement with shorter duration is regarded as noise, and those with longer duration can be most likely regarded as part of the tongue of ionization.

To fulfill the term "F-region" in the first criterion, average raw electron density from 250 to 400 km is calculated at each time record, shown in log scale as black curve in the second panel of Figure 3.1. Based on the second criterion, a 3-point median filter has already been applied to remove high-frequency fluctuations. Then a peak-finding algorithm is applied to only identify those peaks with minimum prominence of $log_{10}(2)$ within a temporal width of 2 hr. The base level used to measure the prominence of a peak is determined in this way: Find the minimum values in a 1-hr window before and after the peak position, respectively, then choose the higher one of the two minimum values to be the base level. The half prominence width indicates the duration between two edges of a patch moving over the radar site. We have applied this patch identification procedure to the entire data set, followed by a visual inspection. As a result, 437 patches have been identified, allowing us to analyze their statistical characteristics.

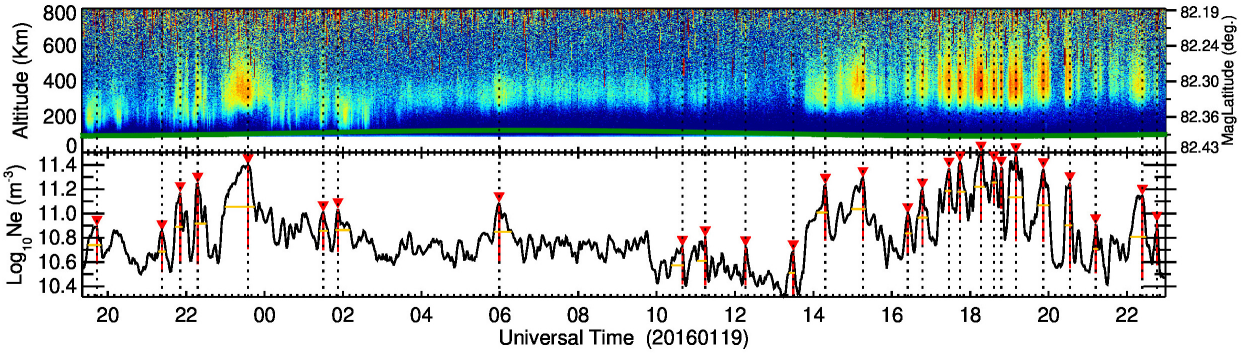

Figure 3.1: An example of patch identification procedure for RISR-C measurement on January 19, 2016. The first panel shows the electron density obtained directly from power with no range integration and no correction for measured temperature. In the second panel, black curve shows average electron density from 250 km to 400 km with a 3-point median filter applied. The density peaks that fulfill the criteria mentioned in the text are marked by red triangles. Within each peak, the vertical red line and horizontal yellow line indicate its prominence and half-prominence width, respectively.

3.3 Statistical Results

3.3.1 MLT Dependence of Patch Occurrence

In Figure 3.2, the first panel presents the total measurement time of RISR-C at each magnetic local time (MLT) and corresponding universal time (UT). The second and third panels show the number of patches observed and patch occurrence frequency (in terms of number of patches observed per hour) at each MLT. In general, patches are observed more often in the afternoon sector between 1400-1900 MLT. About 35% of the patches are observed during this 5-hour period, and nearly

60% of them are observed between 12-24 MLT. The minimum patch occurrence frequency locates at 5 – 6 MLT with a value of one per 7.1 hours, while the maximum occurrence frequency one per 1.4 hour is found at 14 – 15 MLT, nearly 3.2 times of the frequency at 5 – 6 MLT.

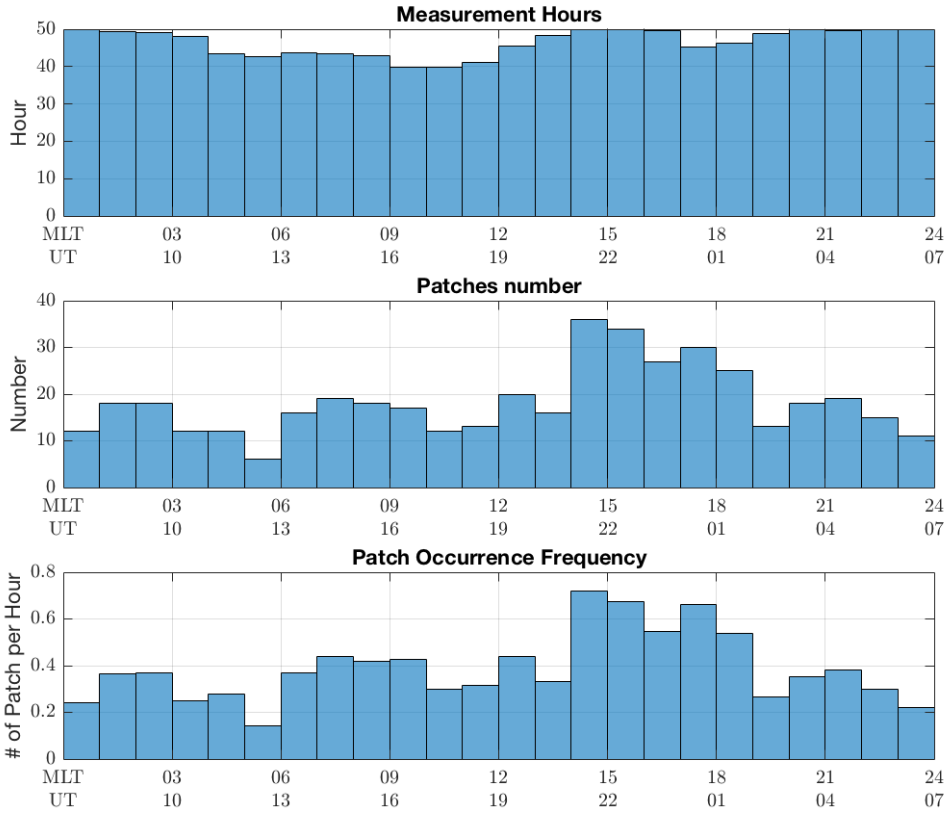

Figure 3.2: MLT and UT distribution of Resolute Bay Incoherent Scatter Radar-Canada measurement time, number of polar cap patches, and patch occurrence frequency. MLT = magnetic local time; UT = universal time.

3.3.2 Superposed Epoch Analysis of Patch Plasma Profiles

Figures 3.3-3.9 show the results of the superposed epoch analysis of the patch plasma profiles measured by RISR-C long pulse mode. At each altitude, the main curve represents the median value of all the corresponding measurements taken at that altitude level, while the horizontal line denotes the range from the first quartile (Q1) to the third quartile (Q3). Beams used in this study are described in section 2.1.

First, the median profiles of electron density (Ne, Figure 3.3), electron temperature (Te, Figure 3.4), ion temperature (Ti, Figure 3.5), ion line-of-sight velocity (LOS Vi, Figure 3.6, 8) and flux

(Ne times LOS Vi, Figure 3.7, 3.9) from all the available measurements are calculated and plotted as the black curves in each figure. Then we separate the data into 4 sectors: dawn (03-09 MLT), noon (09-15 MLT), dusk (15-21 MLT) and midnight (21-03 MLT). For each sector, the median profiles of those 5 parameters are calculated and plotted as the red curves in each figure. At last, the median profiles measured at the density peaks of the patches observed in each sector are plotted as blue curves in each figure. To control the data quality while maintain adequate amount of data for statistical analysis, we filtered the density and temperature data by limiting the relative error (ratio between uncertainty and measured value) to be less than 2. The measurement uncertainties are provided in RISR-C dataset. For LOS velocity, since the relative errors are generally larger, the limit is increased to 4 to keep sufficient data, while another limit that the absolute error should be less than 400 m/s is also added to control the quality of the data used in the study.

3.3.2.1 Electron Density Profile

As shown in Figure 3.3, compared with the overall median density, the sector median shows higher density than the all-MLT median in the noon and dusk sectors, and lower density in the dawn and midnight sectors, at almost all altitude levels. In all of the four sectors, the patch median plasma densities above 200 km are higher than the sector median plasma densities, as expected. The F-region density peak decreases from the dayside ($\sim$2.0×10^{11} m^{-3} for the noon sector, $\sim$3.6×10^{11} m^{-3} for patches) to the night side ($\sim$1.0×10^{11} m^{-3} for the midnight sector, $\sim$2.1×10^{11} m^{-3} for patches), in agreement with the results by Perry and Maurice (2018). The ratio of F-region density peak between the patches and the sector median is $\sim$1.8 in the noon sector and $\sim$2.1 in the dawn, dusk and midnight sectors. The topside ionosphere density differences between the patch and the sector median decrease from the dayside to the night side. Therefore, patch detection using LEO satellite in situ density above 450 km may not be very sensitive on the night side. Also, it is noted that patch density is lower than the sector median density below $\sim$ 200 km at all sectors except on the nightside. This phenomenon has been seen in the SED event reported in Figure 3.8 in Zou et al. (2013) due to lifting of the storm-time F-region plasma to higher altitudes.

3.3.2.2 Electron Temperature Profile

As shown in Figure 3.4, comparing the overall median electron temperature with the sector medians, higher temperature reaching $\sim$2000 K can be seen in the noon sector above $\sim$350 km, while a lower temperature around 1000 – 1250 K is present in the midnight sector. In the dawn and dusk sectors, the sector median electron temperature profiles are closer to the overall profile. Larger variations in the electron temperature above 200 km exist on the dayside than that on the night side. Below 200 km, the midnight sector median electron temperature shows larger variations than

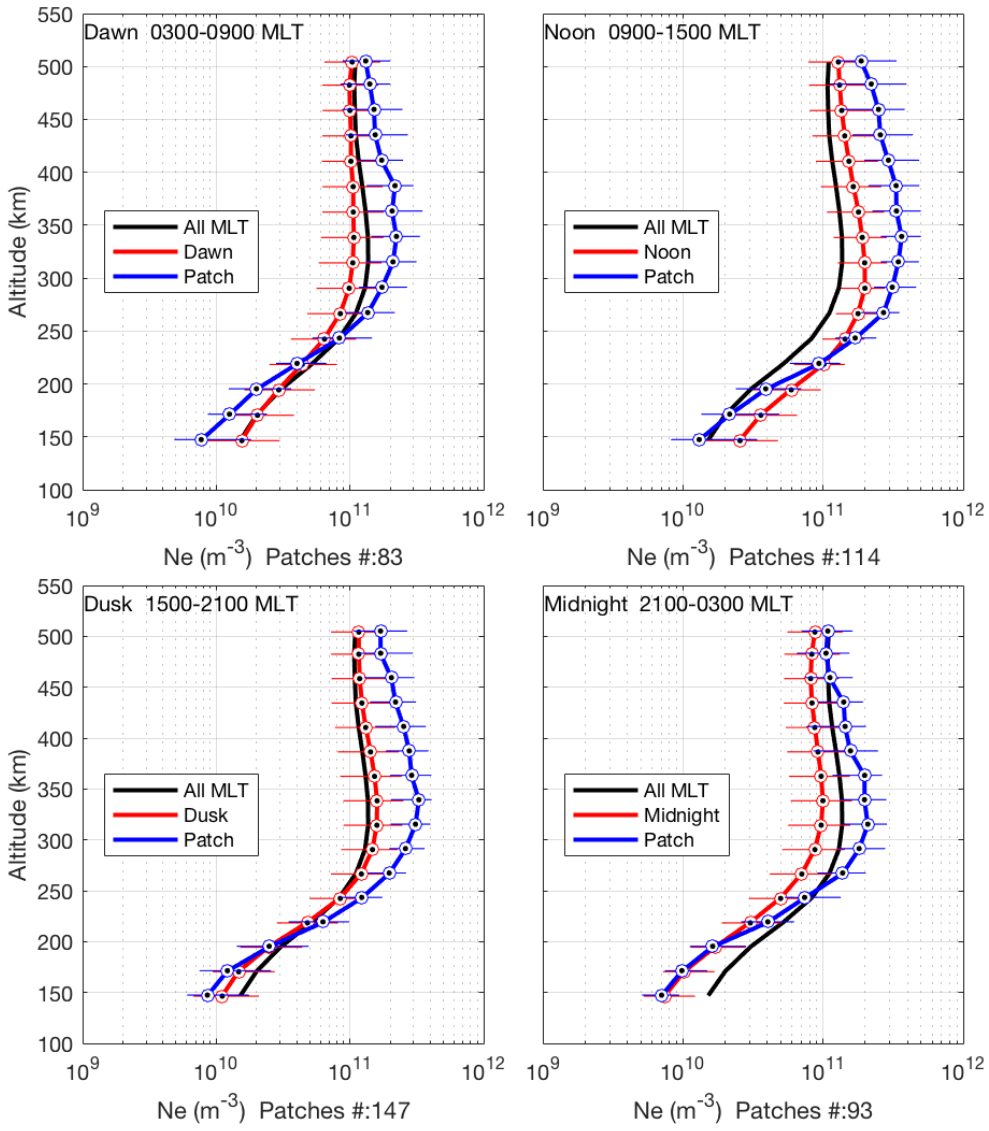

Figure 3.3: Electron density profiles measured in dawn (03–09 MLT), noon (09–15 MLT), dusk (15–21 MLT), and midnight (21–03 MLT) sector, respectively. The black curves represent the median profiles of measurements taken at all the MLTs. The red curves represent median profiles calculated using data only measured at each MLT sector. The blue curves represent median profiles measured at the density peaks of the patches observed in each sector. The horizontal bars (not shown for the black curves) indicate range from the first quartile (Q1) to the third quartile (Q3) of the corresponding data at each altitude. MLT = magnetic local time.

dayside, and the horizontal bars (from Q1 to Q3) of electron temperature mainly extend to its right, which is probably due to the heating effect of particle precipitations such as polar cap arcs on the night side.

In the noon sector, electron temperature within the patches show a clear suppression as large as $\sim$380 K between 250 – 450 km, compared with the sector median temperature. In the midnight

sector, electron temperature within the patches does not show large difference with the sector median. The results by Perry and Maurice (2018) also showed patch electron temperature ∼1800 – 2000 K in sunlit region and ∼1000 K in dark region. In the dawn and dusk sectors, the electron temperature within the patches is slightly lower than the sector median values, but the differences are small compared with that in the noon sector.

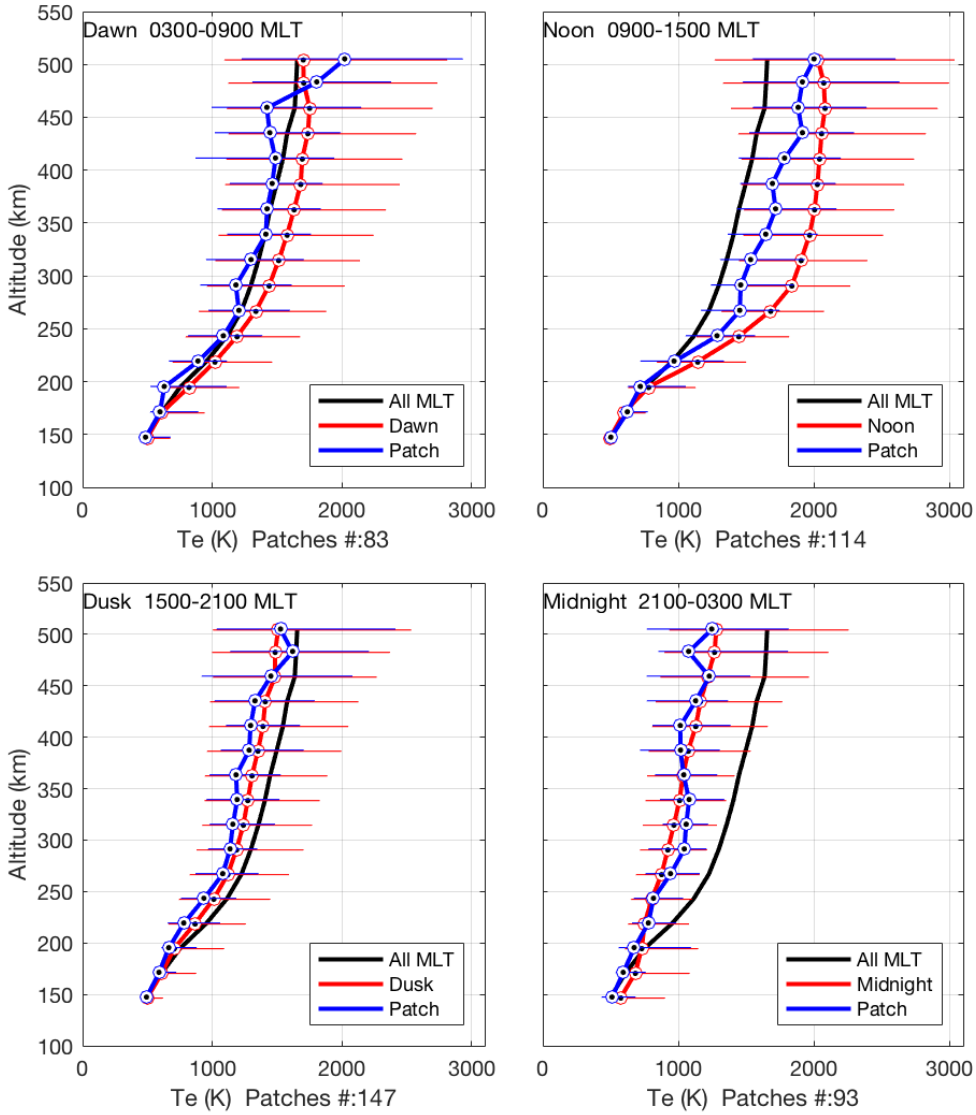

Figure 3.4: Electron temperature profiles in the same format as Figure 3.3.

3.3.2.3 Ion Temperature Profile

In general, the ion temperatures increase slowly to around 1000 K as altitude increases, which are ∼200 K higher than Perry and Maurice (2018) reported based on data taken in 2010 near

deep solar minimum. Thus the difference is likely due to the solar cycle effect. There is little difference shown among the three ion temperature profiles in each sector. In the noon sector, the ion temperature within the patches increases to ∼1230 K at ∼390 km, higher than the sector median by ∼150 K. This heating is likely due to stronger interaction between electrons and ions through the Coulomb collision within the patch. The Coulomb collision rate is proportional to plasma density and inversely proportional to electron temperature (Schunk and Nagy, 2009). So the colder patch electron temperature and the higher density within the patch facilitate stronger coupling between electrons and ions. Combined with electron temperature measurements, the sector median Te/Ti ratio in the noon sector can reach as large as ∼1.9 between ∼290 – 430 km, while within the patches the Te/Ti ratios are only ∼1.3 – 1.6 at the same altitudes.

3.3.3 Line-of-Sight Ion Velocity and Flux Profile

As mentioned in section 2.1, the data used to calculate the statistical profiles in this study are measured by 3 different beams (with 90°, 83° and 85° elevation angle, respectively) throughout the 7-month period, depending on the operation mode of the radar on each run. Specifically, the vertical beam (90° elevation) has in total ∼590 hours observation time and 133 patches observed. Meanwhile, the beam with 83° elevation angle has operated for ∼500 hours in total with 281 patches identified. The last beam with 85° elevation angle only has ∼20 running hours and observed 23 patches. Although the second beam has less total operation hours than the vertical one, it has observed more patches, mainly because January 2016 has seen 122 patches (more than any other months in the data) and during the most of that month only the beam with 83° elevation angle was operated.

In order to study the vertical motion of the patches, at first, only data from the vertical beam are used to calculate the LOS velocity and flux profiles, shown in Figures 3.6 and 3.7. The ion flux is calculated by multiplying ion LOS velocity with electron density, assuming charge neutrality. Since only 133 patches were observed by the vertical beam, the median profiles of the patches have more uncertainty. In addition, the vertical beam of RISR-C (and RISR-N) are less sensitive than the other looking directions since they are near the grating-lobe steering limit of the phased array. For the patch profile in each MLT sector, the median values at some altitudes are not plotted if the number of available data points at that altitude level is less than 10 after applying the data quality filter.

As illustrated in Figures 3.6 and 3.7, the overall median vertical ion velocity is downward (negative) with a speed of ∼60 m/s at ∼300 km, causing downward fluxes $\sim 1.1\times10^{13}$ $m^{-2}s^{-1}$. The sector median profiles of vertical ion velocity are similar to the overall velocity profile. For the noon sector, the sector median flux profile presents a downward flux $\sim 1.3\times10^{13}$ $m^{-2}s^{-1}$ at ∼300 km

because of high F2 layer density peak on the dayside. Within the patches, downward ion fluxes are found between 200 – 500 km in all sectors. In the noon sector, downward ion velocity and flux within the patches can reach as large as ∼66 m/s and ∼3.1×10^{13} $m^{-2}s^{-1}$ at ∼340 km, respectively, while within the patches in the midnight sector, downward ion velocities can reach ∼100 m/s with a downward flux of ∼3.3×10^{13} $m^{-2}s^{-1}$ at ∼360 km.

In addition, the beam with 83° elevation and -157° azimuthal angle observed 281 patches in total and therefore gives better statistical profiles of LOS ion velocity and fluxes, which are shown in Figure 3.8 and 3.9. The overall LOS ion velocity is ∼40 m/s downward at ∼300 km. The overall ion flux is ∼5×10^{12} $m^{-2}s^{-1}$ downward and at ∼300 km, where the density peaks. The noon sector has larger downward ion velocity ∼50 m/s at ∼300 km and downward ion flux ∼1×10^{13} $m^{-2}s^{-1}$ at ∼300 km, while oppositely the midnight sector has upward ion velocity ∼40 m/s between 200 km – 400 km and upward ion flux ∼4×10^{12} $m^{-2}s^{-1}$ at ∼300 km. Within the patches observed in the noon sector, downward ion velocity and flux as large as ∼80 m/s and ∼3×10^{13} $m^{-2}s^{-1}$, respectively, are found between 250 km – 400 km. For patches seen in the midnight sector, upward ion velocity and flux as large as ∼60 m/s and ∼1.2×10^{13} $m^{-2}s^{-1}$, respectively, are found between 250 km – 400 km.

3.4 Discussion

In Figure 3.2, we showed the occurrence frequency of the patches observed by RISR-C as a function of MLT and UT. Previous studies have reported a UT dependence of the polar cap patches occurrence in winter that more patches tend to appear during 1200 –2400 UT (Coley and Heelis, 1995) or during 2000-0300 UT (Sojka et al., 1994; David et al., 2016). This is suggested to be a result of the mismatch between the geographic and geomagnetic poles (Sojka et al., 1979; Foster, 1993; Carlson, 2012) that the polar cap or cusp will extend to lower geographic latitude on the dayside during 1200 – 2400 UT in the Northern hemisphere winter; thus, more solar EUV-produced high-density plasma will be introduced into the polar cap by the ionospheric convection during this period, which is favorable to the formation of polar cap patches. In our results, more patches were observed between 2200-0200 UT, consistent with the findings of Sojka et al. (1994) and David et al. (2016).

As for the MLT dependence, McEwen and Harris (1996) observed more patches during local evening hours than the morning hours, using meridian-scanning photometer at Eureka (89° MLat), close to Resolute Bay (82° MLat). Noja et al. (2013) also reported higher patch occurrence on the dusk side and lower occurrence on the dawn side around 6 MLT at ∼80° MLat, based on the CHAMP TEC observation from 2001 to 2004. In our results, more patches were observed between 1400-1900 MLT, consistent with the McEwen and Harris (1996) and Noja et al. (2013) studies.

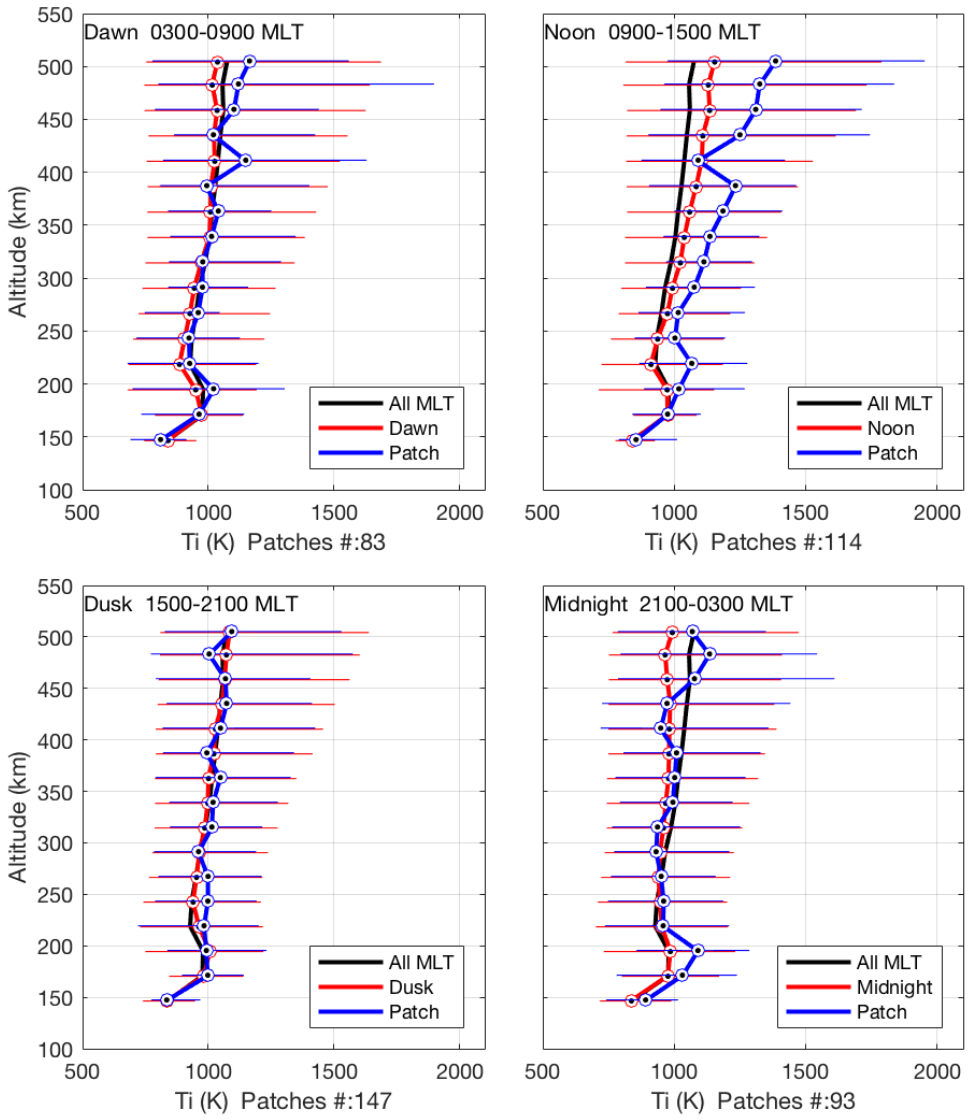

Figure 3.5: Ion temperature profiles in the same format as Figure 3.3.

The asymmetry of the dusk-dawn convection cells is suggested to affect patch MLT occurrence. In the polar cap, anti-sunward plasma flow is typically dominant during southward IMF Bz condition, while positive (negative) IMF By condition results in a dusk-to-dawn (dawn-to-dusk) flow direction near the dayside cusp and then a dawn-to-dusk (dusk-to-dawn) flow direction at higher latitudes. In the statistical study of patch convection velocity at Resolute Bay by Hosokawa et al. (2009), they demonstrated that the dawn-dusk direction of the patches drift velocity has a clear asymmetry: the convection velocity generally has a dawn-to-dusk direction even when the IMF By is 0. This dawn-to-dusk convection tendency can be explained by effect of day-night conductivity gradient (Atkinson and Hutchison, 1978), and it is also supported by empirical models

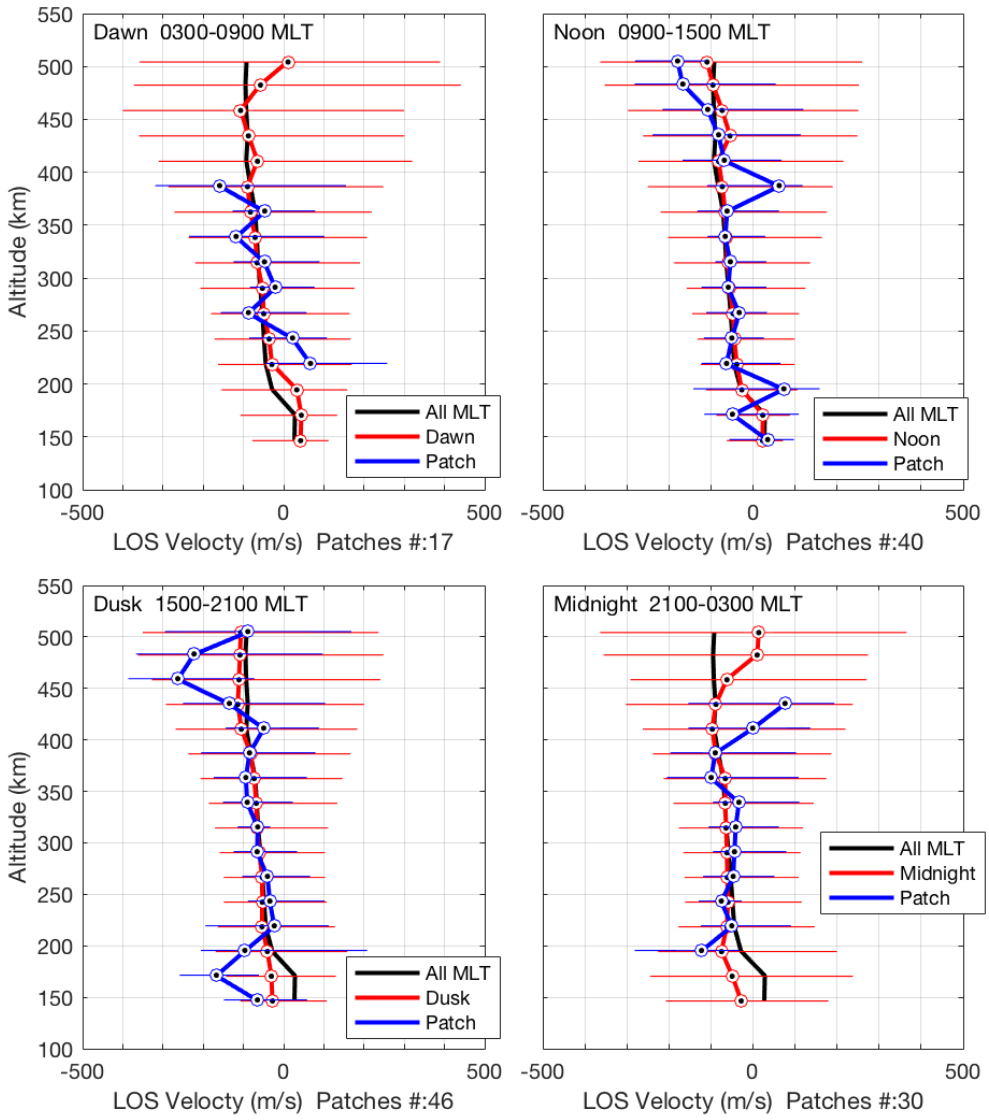

Figure 3.6: Line-of-sight ion velocity profiles in the same format as Figure 3.3, using only the vertical beam (90° elevation angle). Negative (positive) line-of-sight velocity means downward (upward). The median profiles measured within the patches (blue curves) are fluctuating due to the small number of patches observed in each sector. MLT = magnetic local time.

(Ruohoniemi and Greenwald, 1996, 2005) and numerical simulation results (Tanaka, 2001). This statistical dawn-to-dusk convection tendency means, after the patches are generated near the day-side cusp region, more patches will move into the dusk side of the polar cap rather than the dawn side, even when IMF By is close to 0. Therefore, the dawn-dusk asymmetry in the patch occurrence frequency shown in Figure 3.2 may be due to the dawn-dusk asymmetry of high-latitude ionospheric convection pattern.

On the night side, Moen et al. (2007) found a bell-shape patch occurrence distribution centered

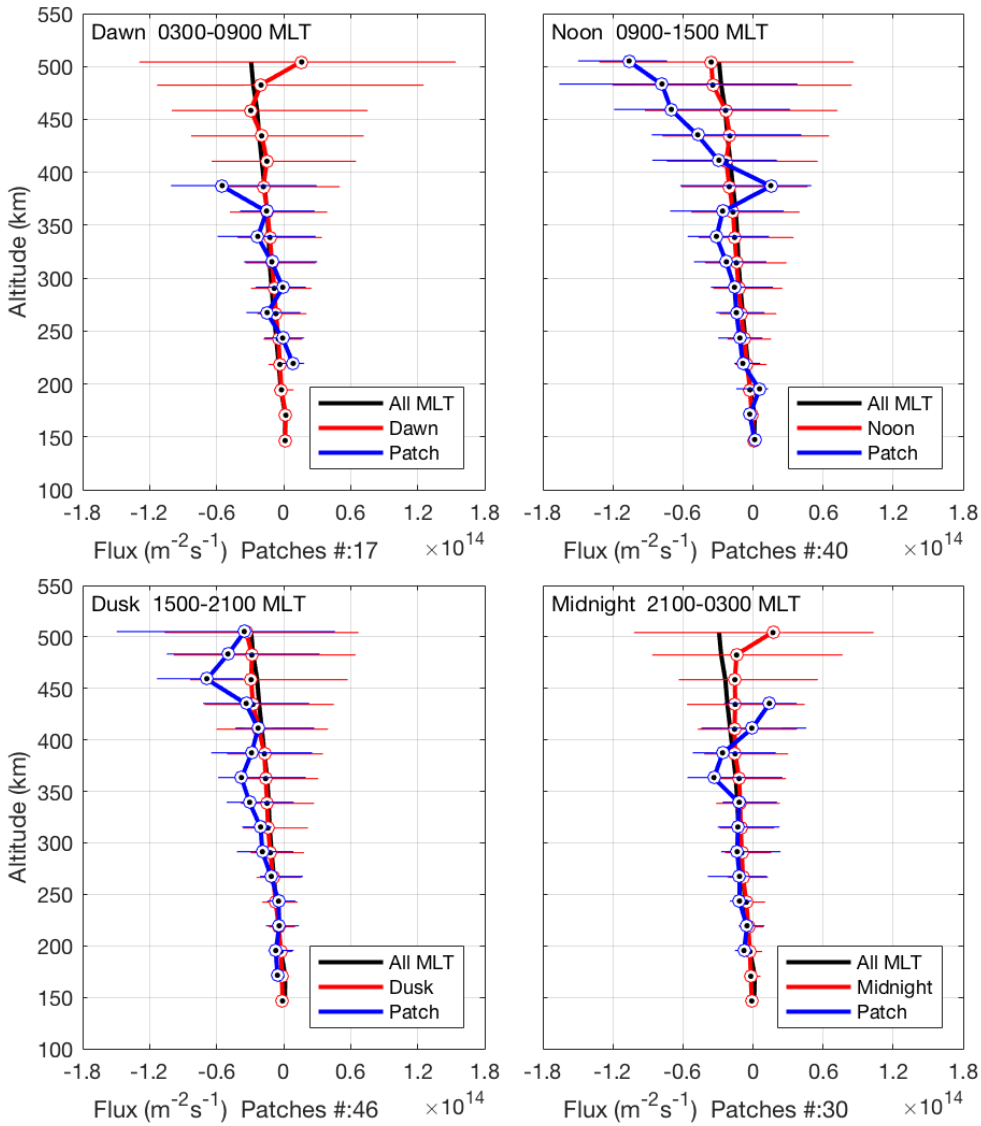

Figure 3.7: Line-of-sight ion flux profiles in the same format as Figure 3.3, using only the vertical beam (90° elevation angle).

at ∼23:25 MLT, a slight shift to the pre-midnight sector, at Svalbard (76° MLat) using a MSP. The authors also attributed this shift to the asymmetry of the convection pattern. It should be noted that several possible reasons could cause the difference between their patch occurrence distribution over MLTs and that in the present study. In their study, emission enhancements that reached the poleward boundary of the auroral oval within the MSP field of view were counted as patches. In addition, the patch occurrence distribution has a strong dependence on latitude. According to Noja et al. (2013), the peak of the patch occurrence is in the dusk side at RISR latitude (∼82° MLat), while for Svalbard (76° MLat) the peak is in the pre-midnight sector.

Therefore, we suggest that the peak of patch occurrence rate on the dusk side can be due to

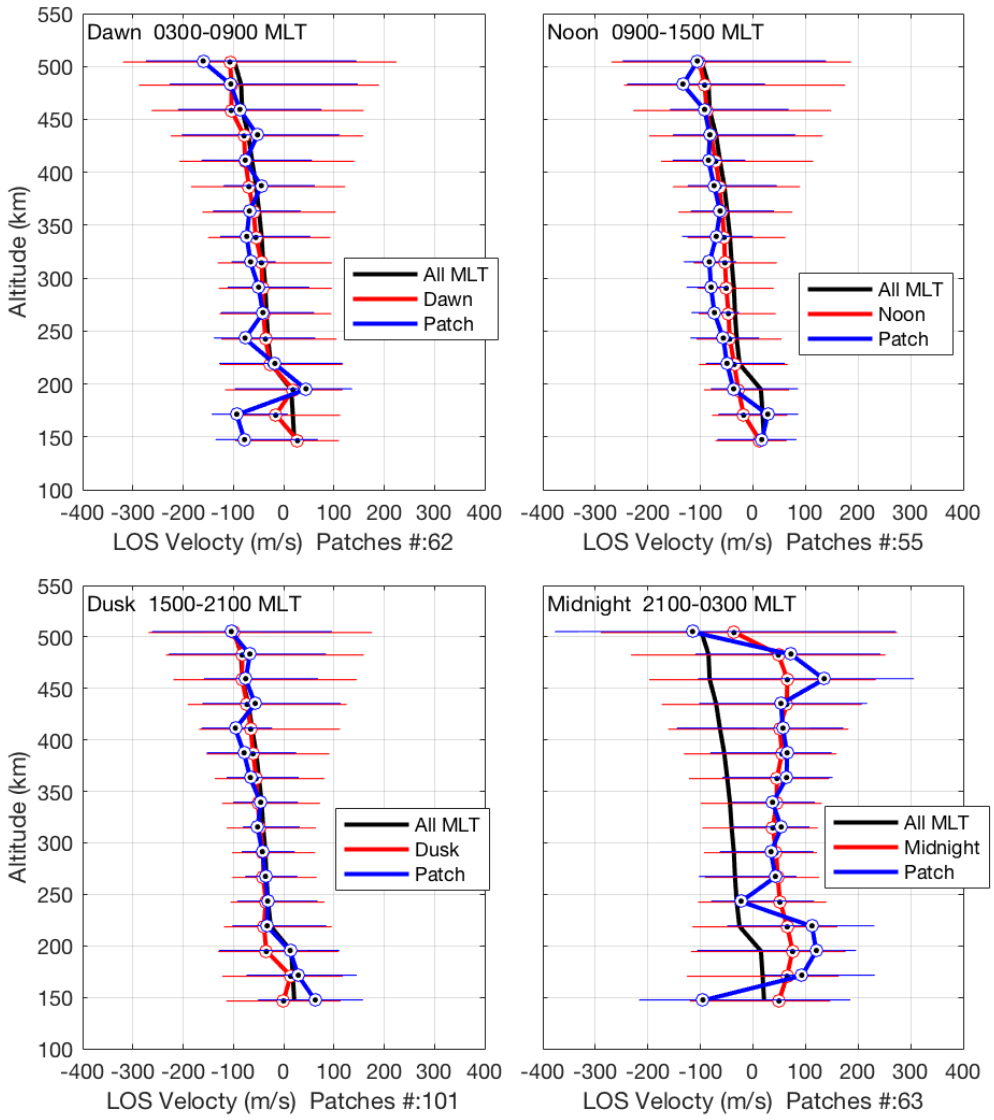

Figure 3.8: Line-of-sight ion velocity profiles in the same format as Figure 3.3, using only the beam with 83° elevation angle and –157° azimuthal angle. MLT = magnetic local time.

both the mismatch of the geographic and the geomagnetic poles and the asymmetry of dawn-dusk ionospheric convection. However, since the instrument we used is fixed on the Earth surface, the importance of these factors cannot be resolved based on the present data set.

Zou et al. (2014) found downward ion fluxes as large as $\sim 10^{14}$ $m^{-2}s^{-1}$ within the SED plume using the PFISR observation (65.4° MLat). They suggested that the downward flux could be explained by enhanced ambipolar diffusion due to an increase in pressure gradient and/or large poleward thermospheric wind during storm times, which can push the plasma downward along the field lines. In the dayside lower latitude region, the magnetic field has a smaller inclination angle, so the E×B drift velocity and the horizontal equatorward wind has a larger upward projection on

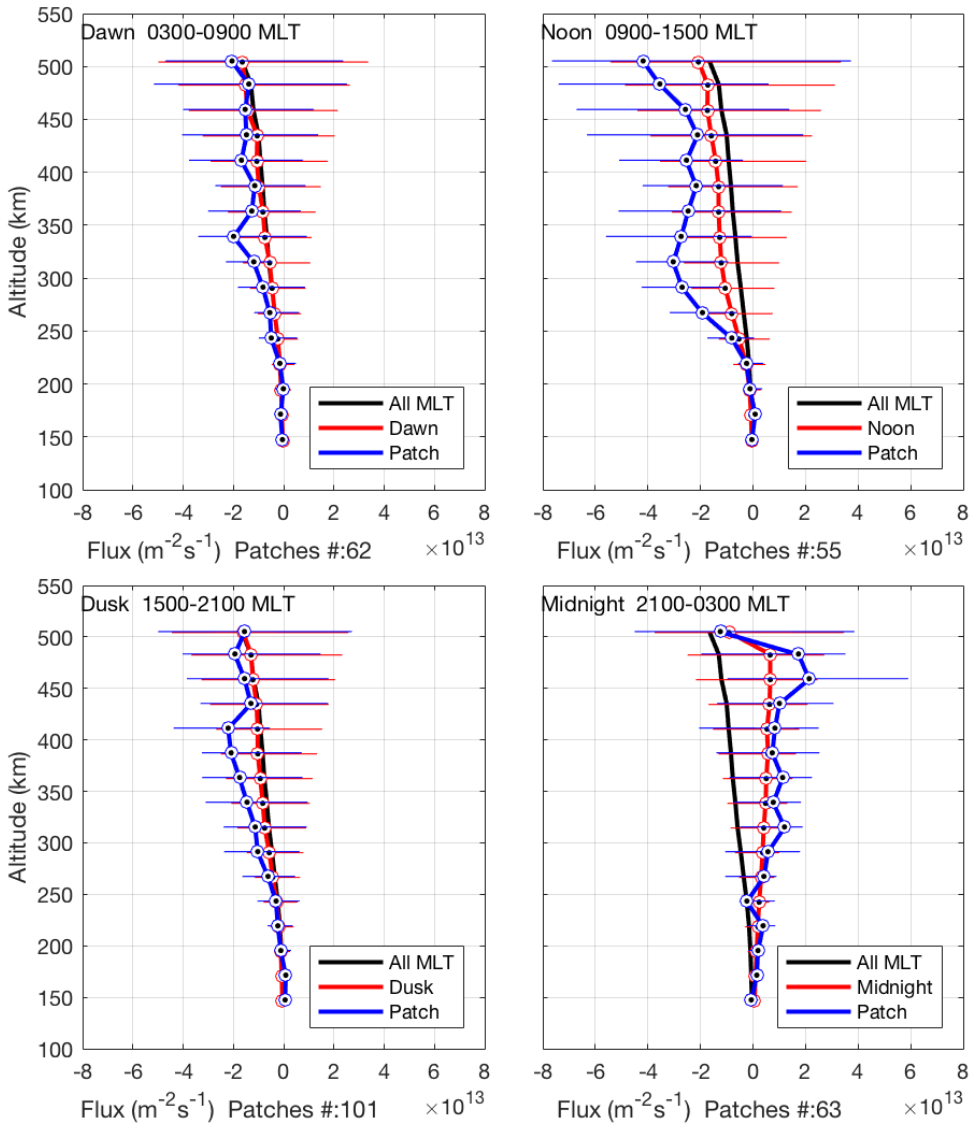

Figure 3.9: Line-of-sight ion fluxes profiles in the same format as Figure 3.3, using only the beam with 83° elevation angle and –157° azimuthal angle. MLT = magnetic local time.

vertical direction, which plays an important role in lifting and holding the plasma at high altitudes. This is also suggested to be important for the formation of high density within SED (Heelis et al., 2009; Zou et al., 2013, 2014). In our case, the elevation angle of magnetic field lines near Resolute Bay is ∼86.41°. The almost vertical field lines make the E×B drift velocity and the horizontal thermospheric wind become ineffective in holding the high-density plasma within the patch. Given a typical patch E×B drift velocity being ∼200 – 400 m/s (Hosokawa et al., 2009) and a typical anti-sunward thermospheric wind velocity being ∼200 m/s at Resolute (Wu et al., 2017), the anti-sunward E×B drift contributes to ∼12 – 25 m/s vertically upward velocity on the dayside and downward velocity on the night side, while the anti-sunward thermospheric wind causes ∼12 m/s

vertically downward velocity on the dayside and upward on the night side. Because the vertical projections from the anti-sunward E×B drift and thermospheric wind have opposite signs on the day and night sides, their combined effect is likely not important in affecting the vertical motion of the patches. Given ∼60 – 100 m/s downward velocity measured within the patches using the vertical beam, we suggest that the high-density plasma within the patches move downward are mainly due to a combination of pressure gradient force and gravitational force.

As for the beam with 83° elevation and -157° azimuthal angle pointing equatorward, since it has lower elevation angle than the magnetic field lines, the anti-sunward E×B drift will have larger downward component when projected along this beam on the dayside and upward component on the night side, same direction as the contribution from the anti-sunward thermospheric wind. Given the same typical E×B drift velocity and thermospheric wind velocity mentioned above, the E×B drift contributes ∼15 – 30 m/s downward velocity on the day side and upward on the night side along this beam direction, while the thermospheric wind produces ∼12 m/s velocity downward on the dayside and upward on the night side. In total, they can lead to ∼42 m/s ion velocity downward at dayside and upward at night side, which is comparable to the results shown in Figure 3.8.

In short, using only the measurements from the vertical beam, we found downward ion fluxes on a scale of 10^{13} $m^{-2}s^{-1}$ within the patches in all four sectors, likely caused by the pressure gradient force and gravity. Typical E×B drift and thermospheric wind at Resolute Bay are not large enough to lift or hold the lifted high density within patches at high altitudes, because of the high elevation angle (86.41°) of the magnetic field lines. A tilted beam with 83° elevation angle has observed more patches and therefore provided better statistical results, which shows downward ion fluxes along the beam in dawn, noon and dusk sectors and upward ion fluxes along the beam in the midnight sector. However, the upward motion of the patches along this beam could be partially caused by the beam's inclination and projection of the E×B drift and thermospheric wind.

3.5 Summary and Conclusion

In this chapter, we analyzed the ionospheric plasma state parameters measured by RISR-C in 2016 to identify the polar cap patches, and study their statistical characteristics, including occurrence frequency in terms of magnetic local time, and the median vertical profiles of their plasma properties. This work is the first systematic study on the vertical plasma profiles of polar cap patches. The conclusions are summarized as following:

- The patches are observed more often in the afternoon sector between 1400-1900 MLT.
- The density enhancement in the patches can extend from ∼200 km up to above 500 km on dayside and up to ∼450 km on night side. The ratio of F-region density peak between the

patches median and the sector median is ∼1.8 on the dayside and ∼2.1 on the night side. Below ∼200 km, the patches median density is lower than the sector median density except in the midnight sector.

- Electron temperature within the patches is lower than the sector median in the noon, dusk and dawn sectors, and the difference is as large as ∼380 K in the noon sector, which suggests that the main plasma source of the patches is solar EUV-produced plasma in the dayside sub-auroral region rather than soft particle precipitation. Smaller electron temperature decrease within the patches is found in the dawn and dusk sectors comparing with that in the noon sector.

- In the noon sector, ion temperature within the patches is higher than the sector median by ∼175 K. We suggest that this is due to stronger coupling between the electrons and ions within patches due to higher Coulomb collision frequency. No significant differences between the ion temperature within the patch and sector median are found in the other sectors. The median Te/Ti ratio in the noon sector can reach as large as ∼1.9 between ∼290 – 430 km, while within the patches the Te/Ti ratio is ∼1.3 – 1.6 at the those altitudes.

- Downward ion fluxes on a scale of $\sim 10^{13}$ $m^{-2}s^{-1}$ are observed within the patches in all the sectors, which are likely due to the combination of pressure gradient and gravitational forces.

It should be noted that the above results are based on the first year of RISR-C data. The patch identification algorithm and statistical analysis presented in this paper will be applied to a more comprehensive data set in the future as RISR-C continues to collect more data. In particular, more field-aligned beam observations have been scheduled, which will improve the field-aligned velocity and flux statistics in the future.

CHAPTER 4

Statistical Study of Ion Upflow and Downflow Observed by PFISR

4.1 Introduction

Ion upflow in the F region and topside ionosphere can greatly influence the ion density and fluxes at higher altitudes and thus may have significant impact on ion outflow. In this chapter, we investigated the statistical characteristics of ion upflow and downflow using a 3-year (2011–2013) data set from the Poker Flat Incoherent Scatter Radar (PFISR).

The results show that ion upflow is twice as likely to occur on the nightside than on the dayside in PFISR observations, while downflow events occur more often in the afternoon sector. Upflow and downflow on the dayside tend to occur at altitudes $\sim$500 km, which is $\sim$100 km higher than those on the nightside. Both upflow and downflow occur more frequently as ion convection speed increases. Upflow observed from 16 to 6 magnetic local time (MLT) through midnight is associated with temperature and density enhancements. Occurrence rates of upflow on the nightside and downflow on the dayside increase with geomagnetic activity level. On the nightside, the occurrence rate of ion upflow increases with enhanced solar wind and interplanetary magnetic field (IMF) drivers as well as southwestward local magnetic perturbations. The lack of correlation of upflow on the dayside with the solar wind and IMF parameters is because PFISR is usually equatorward of the dayside auroral zone. Occurrence rates of downflow do not show a strong dependence on the solar wind and IMF conditions. However, they occur much more frequently on the dayside when the IMF By $>$ 10 nT and the IMF Bz $<$ -10 nT, which may be associated with the decaying of the dayside storm-enhanced density (SED) and the SED plume.

In the next section, the methodology used to identify the ion upflow and downflow events is described. In section 3, statistical results regarding the density, temperature, fluxes, and occurrence rates of ion upflow and downflow as a function of season, magnetic local time (MLT), ionosphere convection, local magnetic perturbation, geomagnetic activity level, and solar wind and IMF are

presented. Summary of the findings of this study is given in section 4. The work in this chapter has been published in Ren et al. (2020b).

4.2 Methodology

4.2.1 Instrumentation

The PFISR is part of the NSF-supported AMISR facility that is used to conduct studies of the upper atmosphere and to observe space weather events. The PFISR data used in this study are downloaded from the SRI AMISR database and the CEDAR Madrigal database. Considering the solar cycle trend and gradual decay of the radar transmit power over time, PFISR has some of its highest quality data from 2011 to 2013 during the peak of solar cycle 24. Therefore, we selected these 3 years (2011–2013) of PFISR data to conduct the statistical study.

4.2.2 Upflow and downflow event identification

The field-aligned ion velocity profiles from the long-pulse PFISR data are used to identify the ion upflow and downflow events. In the high-altitude ionosphere, the ISR data might have large measurement uncertainties. Therefore, we select our upflow and downflow events based on the following criteria. First, we have data quality control criteria that the ratio between the velocity measurement uncertainty and the magnitude of the measurement itself must be smaller than one unless the uncertainty is less than 100 m/s. Second, following the method used in Ogawa et al. (2009), we select reliable ion upflow/downflow events when there are at least three consecutive ion field-aligned speed larger/smaller than 100/-100 m/s in the velocity altitude profile. Figure 4.1 shows examples of the identified ion upflow events (left) and downflow events (right). Dots with green crosses indicate data points satisfying the defined upflow/downflow events selection criteria, while dots with red crosses mean low-quality data points that fail to meet the first criterion. As a result, a total of 36,061 upflow events (or vertical profiles) and 39,632 downflow events (or vertical profiles) have been identified in these 3 years of data. A more restrictive data selection method has also been used and the results are similar and included in the supporting information of Ren et al. (2020b).

4.2.3 Occurrence rate estimation

The identified upflow and downflow data sets are binned according to MLT, month, geomagnetic activity level indicated by the SymH index, and the auroral electrojet index (AE), as well as solar

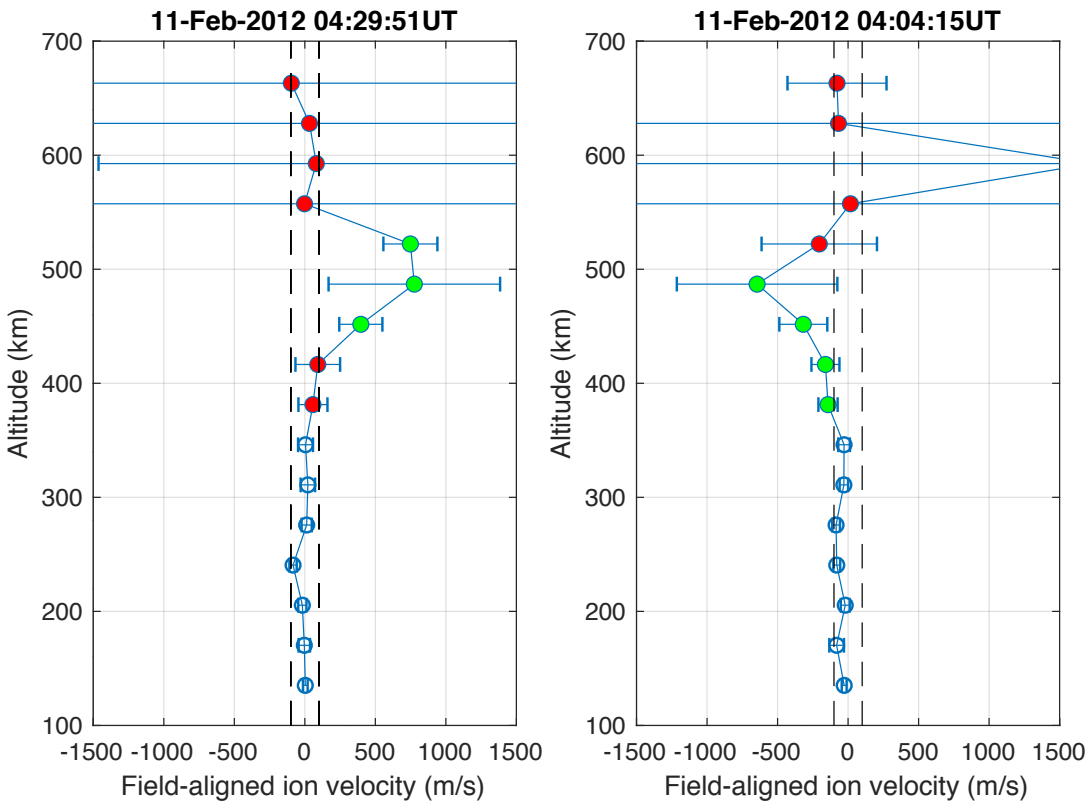

Figure 4.1: Examples of identified ion upflow and downflow events. The left and right panels show examples of an ion upflow record and a downflow record, respectively, on 11 February 2012. The dashed vertical lines mark -100/100 m/s field-aligned ion velocity. The dots in red mark the invalid data points that do not satisfy the data quality criteria, while those in green indicate all the valid data points with velocity smaller/larger than -100/100 m/s for downflow/upflow. Profiles with at least three consecutive green dots are selected as downflow/upflow events.

wind and IMF conditions. For each bin the relative occurrence rate of ion upflow and downflow is defined by

$$f(X) = \frac{n(X)}{N(X)} \tag{4.1}$$

where the variable X could be MLT, month, AE, SymH, solar wind, or IMF parameters, the numerator n is the number of upflow and downflow events in the bin, and the denominator N is the total number of PFISR observations available in that bin. To illustrate more robust statistics, we only show bins with N larger than 20. In order to estimate the uncertainty of the occurrence frequency, we use the following formula to calculate the standard deviation σ within each bin:

$$\sigma = \sqrt{\frac{f \times (1-f)}{N-1}} \tag{4.2}$$

where f is the frequency. Depending on the integration time, the PFISR data have 1- to 5-min time resolution. The range resolution is 36 and 24 km for 480 and 330 μs pulse length, respectively, which is comparable to the data used in Ogawa et al. (2009). To associate geomagnetic indices such as the SymH, AE, as well as solar wind and IMF data with each PFISR measurement record, we calculated the average values of these data within a 5-min window before the center of the measurement time and matched them with each measurement record.

4.3 Results

4.3.1 Diurnal and seasonal variations of ion upflow and downflow altitude and occurrence frequency

The left panels in Figure 4.2 show the distribution of ion upflow occurrence frequency over months (top panels) and MLT (bottom panels). MLT is roughly UT + 13 hr at PFISR located near Fairbanks, Alaska. In the seasonal plots (top panels), the upflow and downflow occurrence frequencies reach the maximum (∼12%) near-summer solstice, that is, May–July, and the minimum (∼6%) after winter solstice, that is, January–February. (Figures 4.2a and 4.2b).

In Figures 4.2c and 4.2d, ion upflow occurs more often on the nightside centered just after midnight, that is, 23–3 MLT. The upflow occurrence frequency reaches the maximum (∼12%) around midnight, which is more than double the minimum occurrence rate (∼5%) in the noon sector (Figure 4.2c). In contrast, the downflow occurs more often in the dusk sector. The downflow occurrence frequency reaches the maximum (∼11.3%) in the dusk sector, while the minimum (∼7%) occurs just before dawn (Figure 4.2d).

The distributions of altitudes of the upflow and downflow as a function of MLT are shown in Figure 4.3. On the nightside, both upflow and downflow tend to occur around 400 km, while on the dayside the altitude increases to slightly above/below 500 km for upflow/downflow.

4.3.2 Ionosphere density, temperature, and field-aligned flux associated with ion upflow and downflow

Figures 4.4 and 4.5 show distributions of ion and electron temperature as well as density and flux, averaged below 600-km altitude, as a function of MLT with only ion upflow/downflow profiles and also with all the profiles for comparison. On the dayside, due to solar radiation, the overall median electron temperature is ∼2200 K, 700 K higher than that on the nightside (Figure 4.4b), and the overall median electron density is $\sim 10^{11.3}$ m^{-3}, about 2.5 times the density near midnight (Figure 4.4c). The median fluxes for ion upflow are $\sim 3 \times 10^{13}$ m^{-2} s^{-1} and are slightly larger during

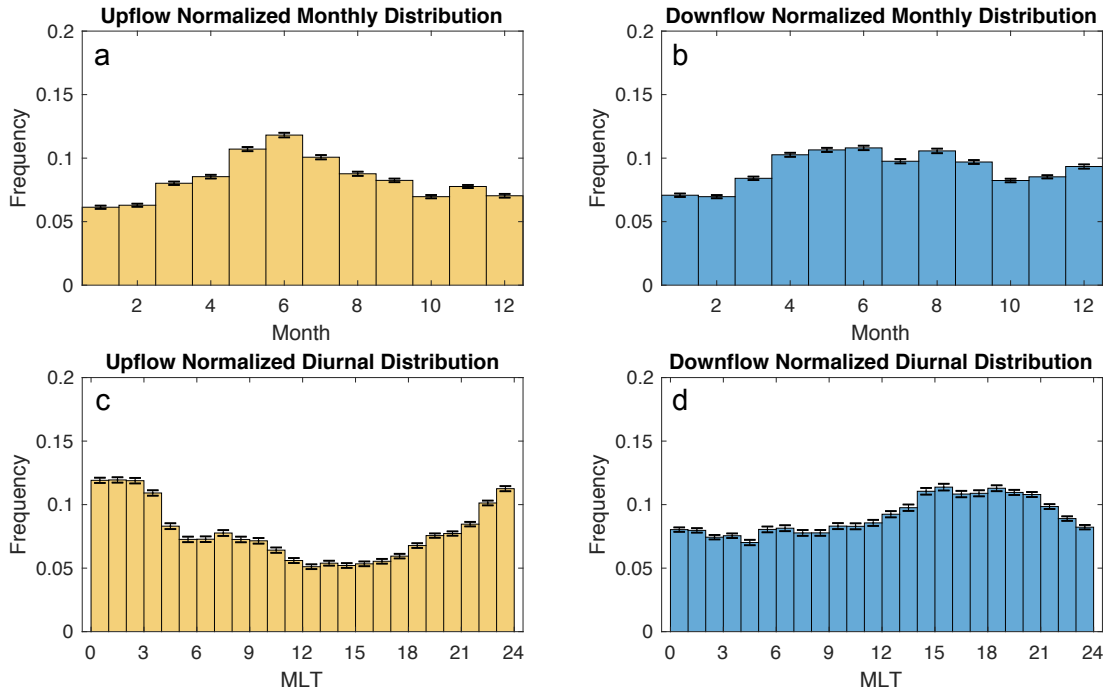

Figure 4.2: Monthly distribution of ion (a) upflow and (b) downflow occurrence frequencies. Magnetic local time (MLT) distribution of ion (c) upflow and (d) downflow occurrence frequencies. MLT is universal time (UT) + 13 at the PFISR site.

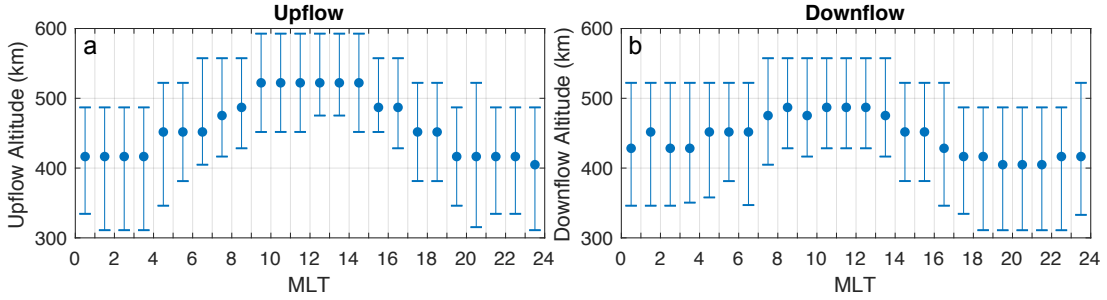

Figure 4.3: Median altitudes of ion (a) upflow and (b) downflow observed by PFISR at each MLT. The dots mark the median altitude of upflow/downflow observed within each MLT bin, while the vertical bars indicate the interquartile range from 25% to 75%.

daytime due to the higher density (Figure 4.4d). There are clear electron (∼200 K) and ion (∼50 K) temperature enhancements for upflow observed from 16 to 6 MLT throughout the nightside, which suggests that ion upflow seen at those MLTs is more likely associated with auroral particle precipitation.

For ion downflow, as shown in Figure 4.5, there is no clear difference in temperature or density comparing with the overall values at each MLT, except that near ∼6 MLT the downflow is associ-

ated with an ∼50 K increase in the median ion temperature. The median fluxes of downflow vary between 2 and 4×10^{13} m^{-2} s^{-1}, depending on the MLT.

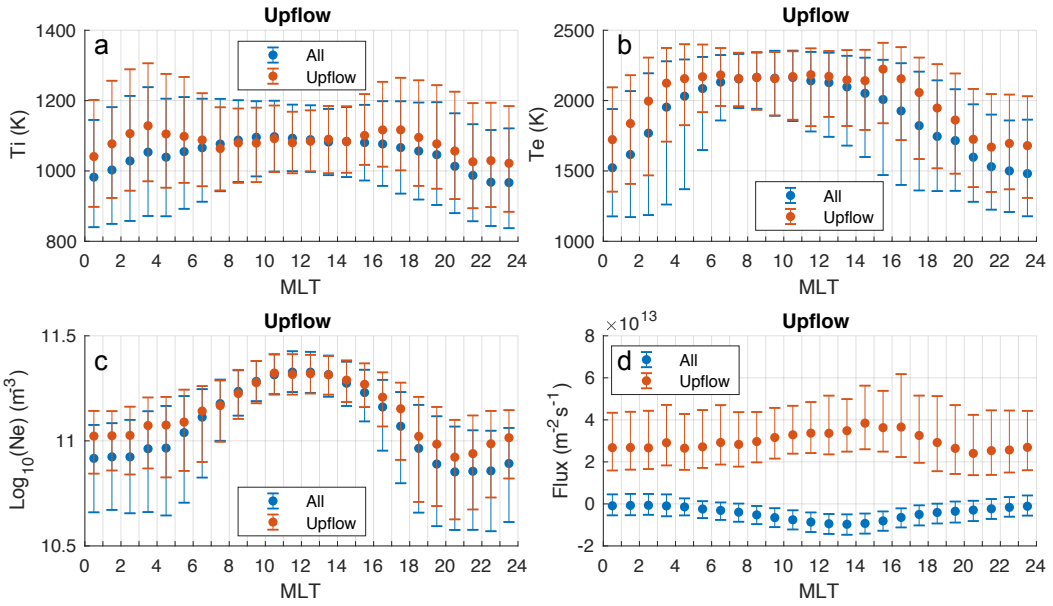

Figure 4.4: Distribution of (a) ion and (b) electron temperature, (c) electron density, and (d) field-aligned ion flux, averaged below 600 km, as a function of MLT with only ion upflow profiles and with all the profiles. The upflow flux is averaged over altitudes where the upflow occurs. The dots mark the median value for each bin and the vertical bars indicate the interquartile range from 25% to 75%.

4.3.3 Local ion convection speed dependence of the ion upflow and downflow occurrence frequency

Ion convection speed (averaged from 65.25° to 66.00° MLat) derived from PFISR multiple-beam line-of-sight ion velocity measurements were matched with each PFISR altitude profile, and its correlation with upflow/downflow occurrence frequency is shown in Figure 4.6. Overall, the occurrence frequency of both upflow and downflow increases almost monotonically as convection velocity increases, and the upflow occurrence is more sensitive to the convection flow speed as indicated by the slope of the trend. For upflow on the dayside, the occurrence frequency stays below 10% until convection speed exceeds 2.5 km/s, where the frequency jumps to ∼20%, whereas on the nightside, the frequency grows rapidly as convection velocity exceeds as low as 750 m/s and reaches 20% at ∼1.5 km/s.

This strong correlation between the upflow occurrence and convection flow speed is consistent with the theory that the frictional heating caused by enhanced convection can lead to ion upflow

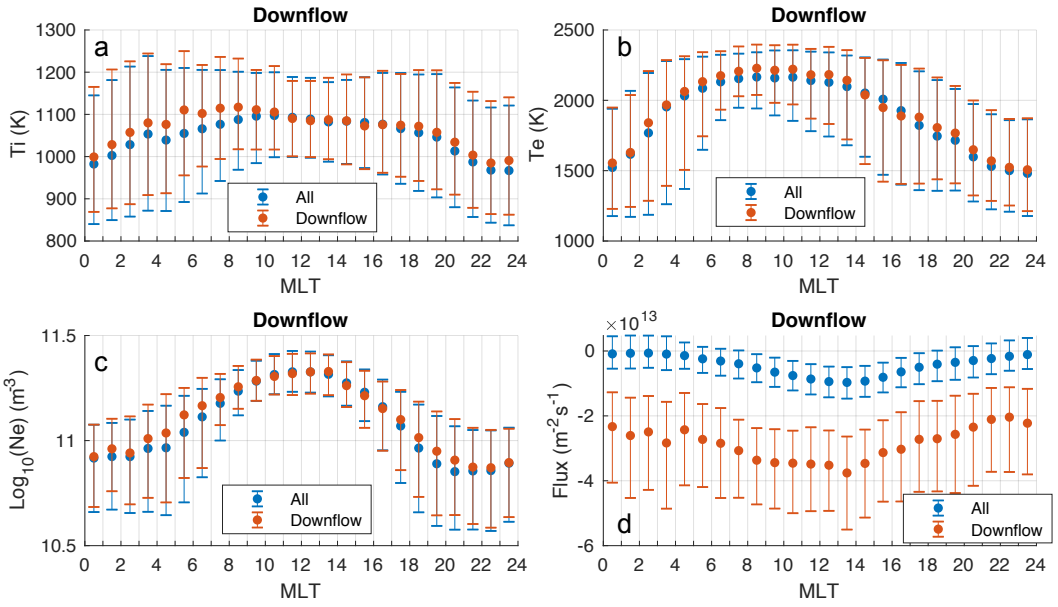

Figure 4.5: Distribution of (a) ion and (b) electron temperature, (c) electron density, and (d) field-aligned ion flux, averaged below 600 km, as a function of MLT with only ion downflow profiles and with all the profiles. The downflow flux is averaged over altitudes where the downflow occurs. The dots mark the median value for each bin and the vertical bars indicate the interquartile range from 25% to 75%.

(Ma et al., 2018; Strangeway, 2005; Zhang et al., 2016). The higher increasing rate on the nightside is likely due to the fact that convection flows and particle precipitation tend to occur at the same time around midnight during enhanced geomagnetic disturbances, and the enhanced convection flows can extend to latitudes lower than the auroral precipitation boundary but the separation between the two boundaries are narrower on the nightside (Zou et al., 2009b,a).

4.3.4 Geomagnetic activity dependence of the ion upflow and downflow occurrence frequency

4.3.4.1 AE dependence

Figure 4.7 shows how the occurrence frequencies of ion upflow (top panels) and downflow (bottom panels) are influenced by the auroral electrojet strength represented by the AE index. From left to right, the two panels in the same column show occurrence frequencies averaged over all MLTs, only on the dayside (9–15 MLT) and only on the nightside (21–3 MLT), respectively. The occurrence rate of ion upflow averaged over all MLT (Figure 4.7a) increases steadily with AE from ∼6% to ∼25%. Although when AE is larger than 1,600 nT, the upflow occurrence frequency starts to decrease as AE increases. This is likely due to the limited available number of events with AE

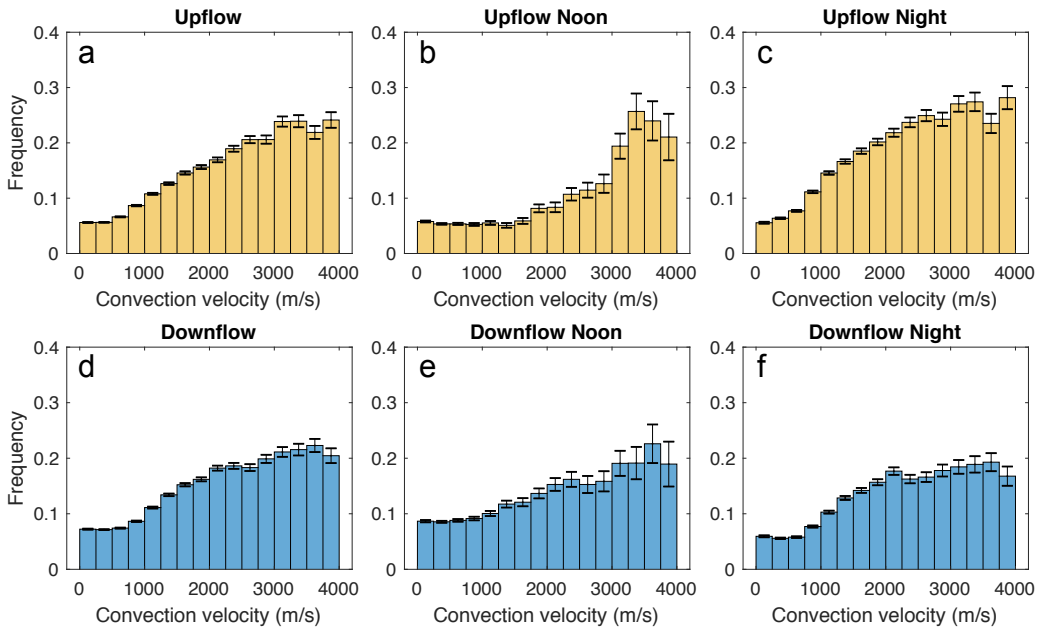

Figure 4.6: Occurrence frequency of ion upflow and downflow as a function of ion convection velocity for different MLT intervals: (a) all MLTs, (b) on the dayside between 9–15 MLT (4,831 upflow, 7,667 downflow), (c) on the nightside between 21–3 MLT (15,911 upflow, 12,292 downflow). (d–f) Downflow occurrence frequencies are in the same format as that for upflow.

higher than 1,600 nT, as indicated by the increasing size of the error bar. On the dayside (Figure 4.7b), there is no obvious relationship between AE and the upflow occurrence rate for AE less than ∼1,000 nT, where the rate is ∼5%. When AE is greater than 1,000 nT, the upflow occurrence rate on the dayside increases to ∼13%. On the nightside (Figure 4.7c), there is a clear increasing trend for the upflow occurrence rate, that is, from less than 10% for quiet time to ∼25% when AE increases from 0 to ∼700 nT. After AE exceeds ∼700 nT, the upflow occurrence rate does not change significantly, while at the same time, the uncertainties reflected by the size of the error bar also increase after that due to the lack of observations.

The downflow occurrence frequency does not show any clear dependence with AE when averaged over all MLTs (Figure 4.7d), but it is positively correlated with AE on the dayside (Figure 4.7e) with the maximum occurrence rate of ∼17% and weakly negatively correlated on the nightside (Figure 4.7f) with the peak occurrence rate of ∼9% when AE is less than 300 nT. The negative correlation on the nightside becomes less obvious when AE increases to 1,000 nT due to the reduced availability of large AE events.

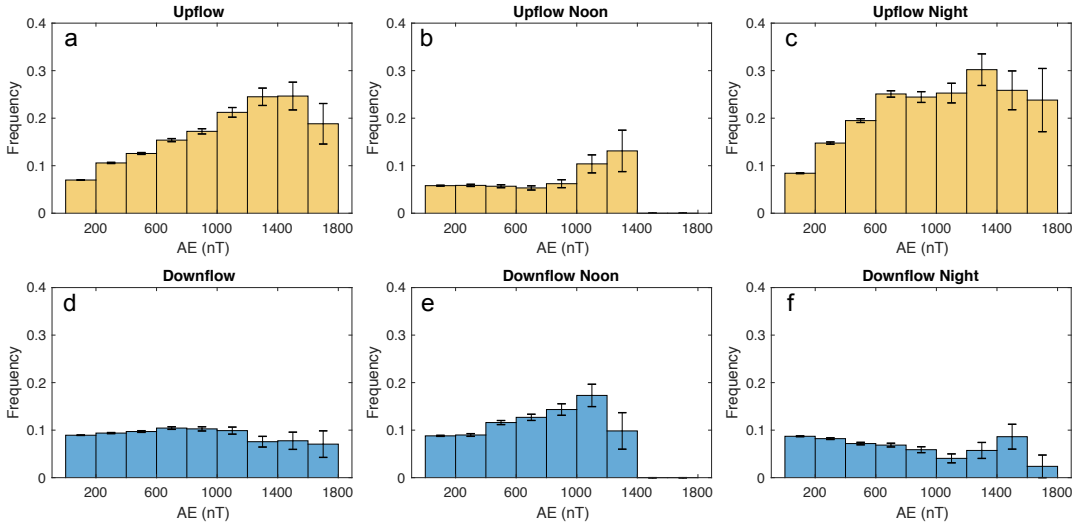

Figure 4.7: Ion upflow (first row) occurrence frequency plotted over AE index over different MLT intervals: (a) all MLTs, (b) on the dayside between 9–15 MLT (4,831 upflow, 7,667 downflow), (c) on the nightside between 21–3 MLT (15,911 upflow, 12,292 downflow). (d–f) Downflow occurrence frequencies (second row) are in the same formats as those for the upflows.

4.3.4.2 SymH Dependence

The dependence of ion upflow (top panels) and downflow (bottom panels) occurrence frequencies on the ring current strength represented by the SymH index is shown in Figure 4.8. From left to right, the three panels show occurrence rates averaged over all MLTs, in the dayside sector (09–15 MLT) and in the nightside sector (21–03 MLT), respectively. A clear increasing trend of the ion upflow occurrence rate with increasing ring current strength, that is, decreasing SymH, can be seen in Figure 4.8a. The upflow occurrence frequency increases from the minimum $\sim$7% when SymH is $\sim$15 nT to the maximum $\sim$21% when SymH reaches $\sim$-100 nT. Interestingly, the upflow occurrence rate also increases when the SymH becomes strongly positive, that is, under conditions with strong compression of the magnetosphere. Similar to the dependence on the AE index, the dayside ion upflow occurrence frequencies show no obvious trend with SymH (Figure 4.8b) except for a significant increase when SymH reaches -120 nT. Under those strong driving conditions, the dayside auroral oval likely extends to much lower latitudes and engulfs PFISR. Thus, PFISR is able to probe the dayside auroral oval under these circumstances. A strong correlation between the nightside ion upflow occurrence rate and SymH can be seen in Figure 4.8c. The nightside occurrence of ion upflow increases with decreasing SymH down to $\sim$-120 nT reaching the maximum of about 29.5%. Again, the error bars are slightly larger for the large negative SymH events because of fewer PFISR measurements during such disturbed periods.

The ion downflow occurrence rate over all MLTs (Figure 4.8d) shows a weak increasing trend

with decreasing SymH, due to exact opposite trends on the dayside (Figure 4.8e) and nightside (Figure 4.8f). On the dayside, there is a strong positive correlation between the downflow occurrence rate and the ring current strength, with the peak rate reaching ∼31% at SymH ∼-135 nT. In contrast, the nightside occurrence rate of downflow (Figure 4.8f) shows no clear trend for quiet times (SymH ∼ 0), but decreases slightly for large negative SymH.

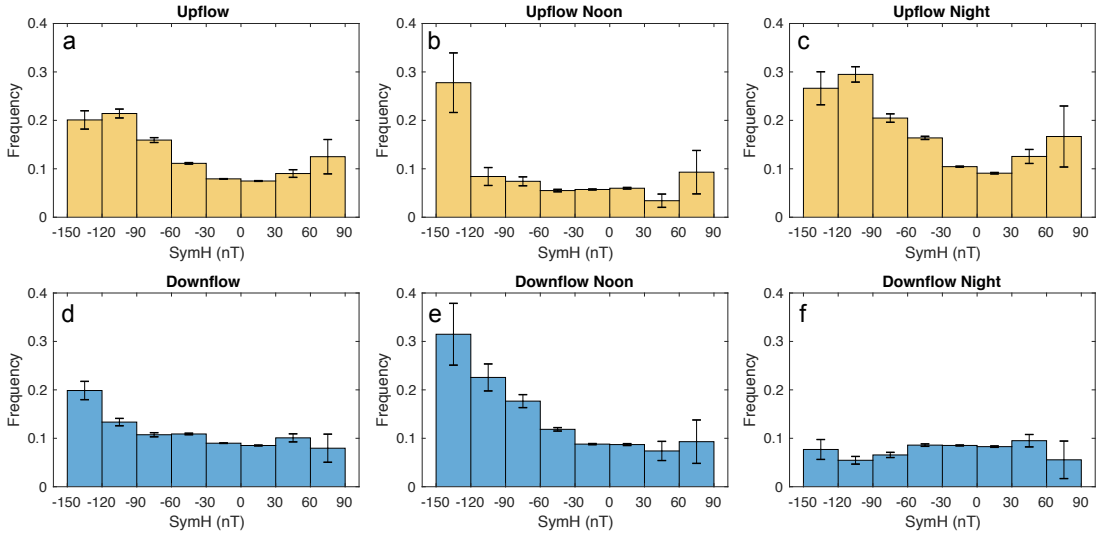

Figure 4.8: Ion upflow (first row) occurrence frequency plotted over SymH index over different MLT intervals: (a) all MLTs, (b) on the dayside between 9–15 MLT (4,831 upflow, 7,667 downflow), (c) on the nightside between 21–3 MLT (15,911 upflow, 12,292 downflow). (d–f) Downflow occurrence frequency (second row) formats the same as upflow.

4.3.4.3 Local magnetic perturbation dependence

Comparing with global geomagnetic indices, local magnetic perturbation is likely a more sensitive indicator for local ion upflow activities. To study this, we used SuperMAG magnetic perturbation data with 1-min resolution and baseline subtracted (Gjerloev, 2012) at Poker Flat (PKR) and College (CMO) Station, which were matched with all the PFISR records at the closest minute. Figure 4.9 shows the correlation between ion upflow occurrence frequency and local magnetic perturbations. The overall magnetic perturbations near PFISR (Figure 4.9a) are dominated by those in the southwestward and northeastward directions. On the nightside (Figure 4.9b), the occurrence frequency of ion upflow increases from below 10% with nearly no magnetic perturbation to above 25%, when there is strong southwestward magnetic perturbation reaching magnitude over 400 nT. The southwestward magnetic perturbation is due to a tilted westward electrojet typically seen just poleward of the Harang reversal (Zou et al., 2009b). This clear correlation between the night-

side ion upflow occurrence and the southwestward magnetic perturbation suggests that enhanced ion upflow occurrence is due to enhanced auroral precipitation associated with the substorms (Zou et al., 2009b,a). Meanwhile, such correlation is not found on the dayside. For downflow occurrence (not shown here), no clear correlation is found on either dayside or nightside.

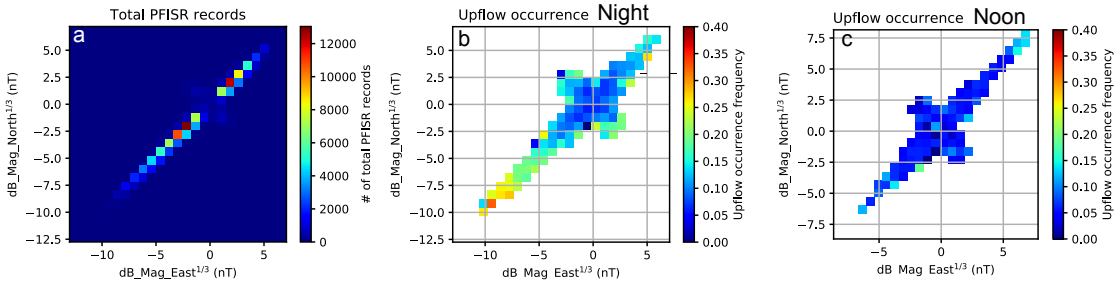

Figure 4.9: Heatmaps showing (a) distributions of local magnetic puerturbations matched with all PFISR records, (b and c) distribution of ion upflow occurrence frequency on local magnetic perturbations for data on the (b) nightside between 21–3 MLT and (c) on the dayside between 9–15 MLT. The magnetic perturbations are measured in local magnetic north and east directions and are plotted after applying cubic root for better visual clarity.

4.3.5 Solar wind and IMF dependence of ion upflow and downflow occurrence rates

For solar wind and IMF parameters, extracted from NASA OMNI data set through OMNIWeb, we match them to the upflow/downflow data with the smallest time difference, then take the average of solar wind and IMF within 5 min ahead of the upflow or downflow events. Considering propagation of the IMF effects might take over 1 hr from bow shock nose to the nightside auroral zone (Browett et al., 2017; Rong et al., 2015; Zhang et al., 2015), alternative average durations up to 1 hr have been tested and no statistically significant differences in the results are found.

4.3.5.1 Solar wind

Figure 4.10 shows how solar wind parameters (solar wind velocity (first row), proton number density (second row), and dynamic pressure (third row)) influence the occurrence frequencies of ion upflow. From left to right, the three panels in the same column show distributions over all MLTs, in the dayside sector and in the nightside sector, respectively. The three panels in the first column show that the ion upflow occurrence rates slightly increase when the solar wind velocity, number density, and dynamic pressure increase in general. The solar wind velocity shows the strongest positive dependency with the upflow. In particular, the occurrence rate increases much

faster for fast solar wind (>600 km/s) than that for slow solar wind speed. On the dayside (Figures 4.10b and 4.10e), no clear dependences appear between the solar wind velocity and proton number density and the ion upflow occurrence frequency. On the nightside (Figures 4.10c, 4.10f, and 4.10i), stronger dependences of the upflow occurrence rate on all three parameters can be observed, with the maximum occurrence frequency reaching ∼25% during high solar wind velocity ∼800 km/s or dynamic pressure ∼20 nPa.

Similarly formatted as Figure 4.10, Figure 4.11 shows the dependence of the ion downflow occurrence frequencies on the solar wind velocity (top row), proton number density (middle row), and dynamic pressure (bottom row). The downflow occurrence frequency slightly increases as the velocity increases over all MLTs (Figure 4.11a) and in the dayside sector (Figure 4.11b). No clear dependence is observed between solar wind proton number density or dynamic pressure and the downflow occurrence, except that when the proton number density exceeds ∼40 cm^{-3}, there is an increasing trend in the downflow occurrence frequency, with a peak of ∼18% at ∼55 cm^{-3}.

4.3.5.2 IMF

Figure 4.12 shows the dependence of ion upflow occurrence frequencies of the total IMF (first row), IMF Bx (second row), IMF By (third row), and IMF Bz (fourth row) in the Geocentric Solar Magnetospheric (GSM) coordinates. From left to right, the three columns of panels show distributions over all MLTs in the dayside sector and in the nightside sector, respectively. The overall upflow occurrence frequency in the dayside sector (Figures 4.12b, 4.12e, 4.12h, and 4.12k) is relatively low, that is, ∼10%, and insensitive to the IMF parameters. However, there are clear increasing trends between the ion upflow occurrence frequency and the total IMF over all MLTs (Figure 4.12a) and in the nightside sector (Figure 4.12c). In Figures 4.7d, 4.7g, and 4.7j, a rough bimodal distribution with the center around zero can be observed for all three IMF components. The occurrence rate increases with the magnitude of the IMF components, and the maximum occurrence rate exceeds 17% for Bx near -12 nT and >30% for By and Bz below -20 nT. This bimodal distribution is even clearer in the nightside sector (Figures 4.12f, 4.12i, and 4.12l).

In the bottom row, the increasing trend of the upflow occurrence rate with negative Bz is much more rapid than that with positive Bz. It is very well known that strong energy coupling between the solar wind and the magnetosphere occurs when the IMF is southward (IMF Bz < 0). Therefore, as expected, the occurrence frequency of ion upflow increases with stronger geomagnetic activities and auroral zone expansions as the IMF Bz decreases. This increasing trend becomes less clear when the IMF Bz is strongly southward, that is, smaller than -12 nT, which again is likely due to the limited availability of strong southward IMF Bz events as evidenced by the larger error bars.

Figure 4.13 shows the dependence of the ion downflow occurrence frequencies of the total IMF (top row), IMF Bx (second row), IMF By (third row), and IMF Bz (bottom row). From left

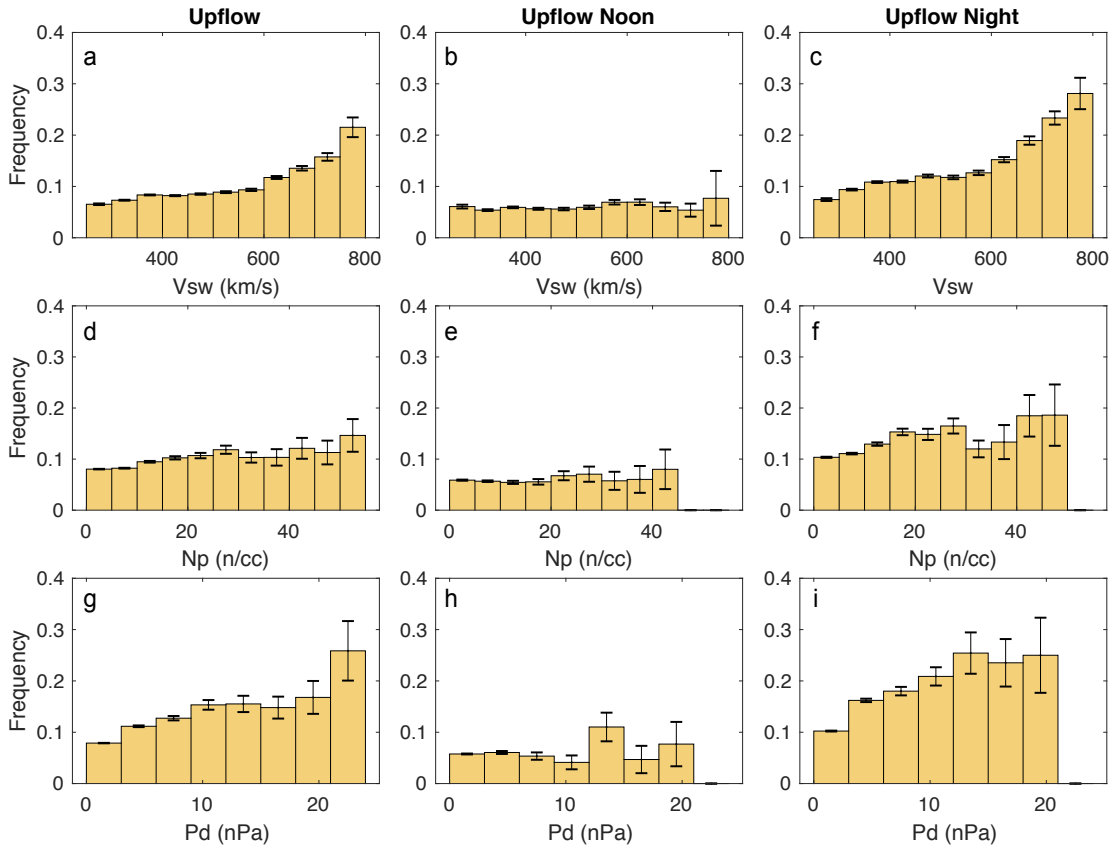

Figure 4.10: Ion upflow occurrence frequency plotted over solar wind parameters, extracted from NASA OMNI data set through OMNIWeb: Velocity (first row), proton number density (second row), dynamic pressure (third row), for different MLT intervals: (a, d, g) all MLTs, (b, e, h) on the dayside between 9–15 MLT (4,831 upflow, 7,667 downflow), (c, f, i) on the nightside between 21–3 MLT (15,911 upflow, 12,292 downflow).

to right, the three columns of panels show distributions over all MLTs in the dayside sector and in the nightside sector, respectively. The overall correlation between the downflow occurrence frequency and the total IMF is positive, in particular on the dayside (Figure 4.13b), while on the nightside there is no clear correlation (Figure 4.13c). No obvious dependency between the downflow occurrence frequency and Bx can be seen (Figures 4.13d–4.13f), except for extremely large $|\mathrm{Bx}| > 12$ nT although the error bars become larger as well. In terms of By, on the dayside, the downflow clearly prefers to occur when By is strongly positive, and the maximum downflow occurrence frequency reaches $\sim$18% when By is $\sim$18 nT (Figure 4.13h). Similarly, in Figure 4.13k, the downflow occurrence frequency also prefers strongly negative Bz, that is, $<$ -10 nT, on the dayside.

Since both the IMF By and Bz components have shown notable correlations with upflow and downflow occurrence frequency, joint distributions are shown in Figure 4.14 to further study the

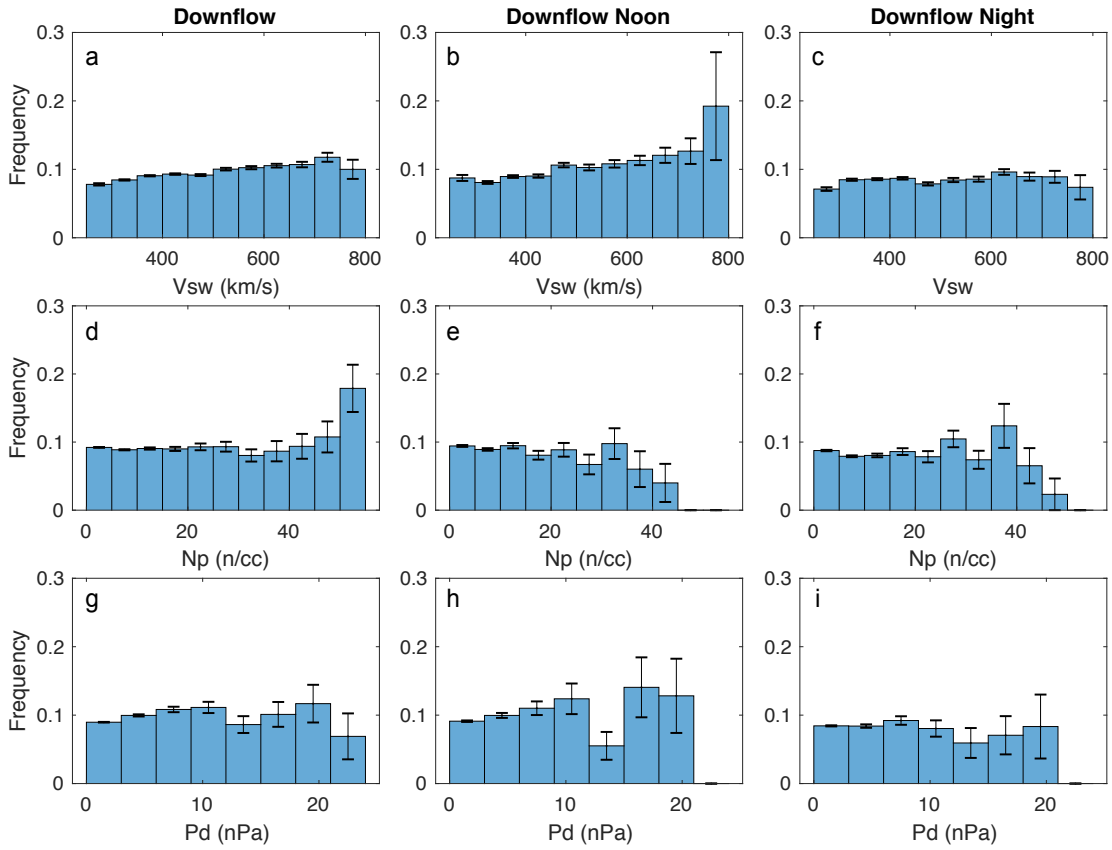

Figure 4.11: Ion downflow occurrence frequencies plotted over solar wind parameters, in the same format as ion upflow (Figure 4.10).

effects from the IMF clock angle and magnitude. Comparison between Figures 4.14e and 4.14h clearly indicates that, at Poker Flat, the upflow occurrence frequency is significantly higher on the nightside than it is on the dayside, at least when the IMF Bz is larger than -16 nT. Later discussion will suggest this is most likely due to its relative location with the auroral zone under quiet and moderate geomagnetic conditions. The overall occurrence of upflow, as shown in Figure 4.14b, increases as the IMF Bz decreases, and the highest occurrence frequencies are reached during strongly negative IMF Bz conditions when the IMF By also has magnitude larger than 8 nT. When the IMF Bz is near zero, the upflow occurrence shows a bimodal distribution on the IMF By where the occurrence frequency increases as the IMF By increases its magnitude.

As for downflow, the highest occurrence frequencies are seen on the dayside when the IMF Bz is strongly negative $\sim$-14 nT and IMF By is strongly positive $\sim$16 nT. Also, by comparing Figures 4.14f and 4.14i, it can be noticed that on the dayside negative IMF Bz conditions tend to favor the occurrence of downflow, while on the nightside downflow seems to occur more frequent during positive IMF Bz conditions.

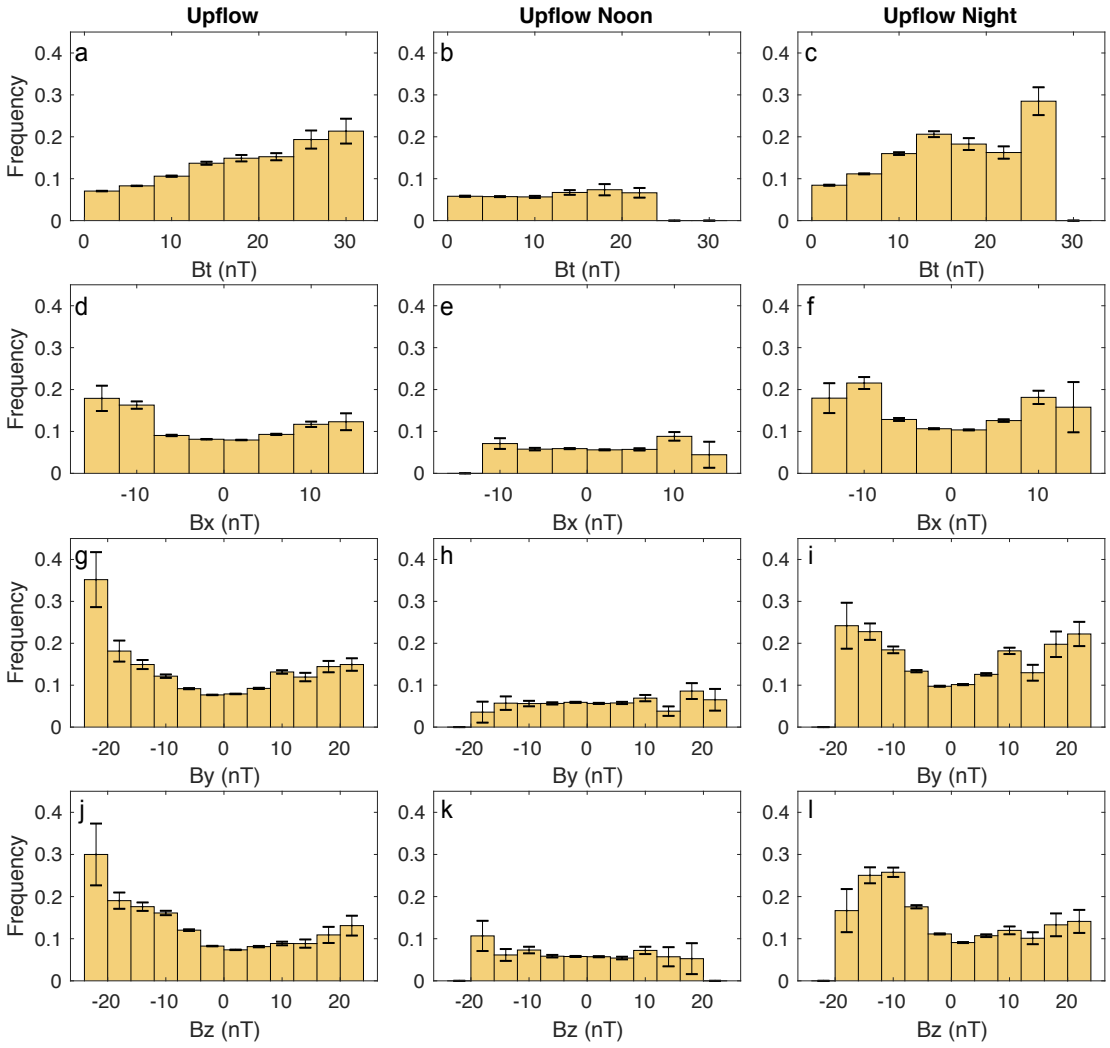

Figure 4.12: Ion upflow occurrence frequency plotted over the IMF components, extracted from NASA OMNI data set through OMNIWeb: Total IMF (first row), IMF Bx (second row), IMF By (third row), IMF Bz (fourth row), for different MLT intervals: (a, d, g) all MLTs, (b, e, h) on the dayside between 9–15 MLT (4,831 upflow, 7,667 downflow), (c, f, i) on the nightside between 21–3 MLT (15,911 upflow, 12,292 downflow).

4.4 Discussion

4.4.1 Upflow

It is generally known that ion upflow can be generated by either frictional heating mechanism (Type 1 upflow) or enhanced ambipolar electric field due to electron heating (Type 2 upflow) (Wahlund et al., 1992). These heating mechanisms prevail near or within the auroral oval; therefore, the ion upflow occurrence rate observed by PFISR strongly depends on its relative location to the auroral oval, the strength of auroral precipitation, and the convection flow speed.

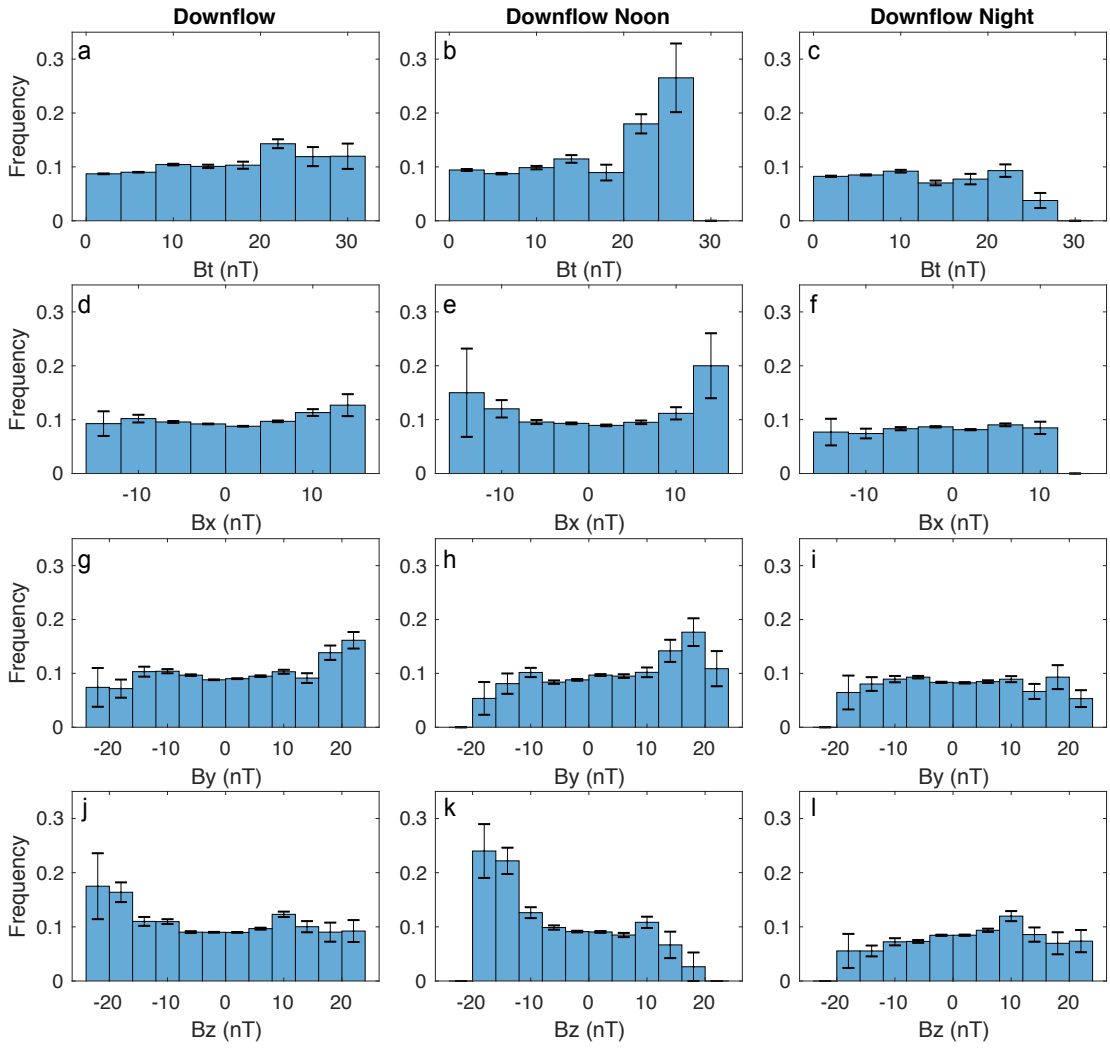

Figure 4.13: Ion downflow occurrence frequency plotted over the IMF components, with the same format as the ion upflow (Figure 4.12).

As shown in section 4.3, there is a strong day-night asymmetry of the upflow occurrence frequency with clear preference for nightside. This agrees well with previous statistical studies done by Keating et al. (1990) and Foster et al. (1998) using data from EISCAT at Tromsø (∼66.7° MLat, similar to PFISR at ∼65.5 ° MLat) from 1984 to 1996, in which they found a peak of upflow occurrence frequency near 23 MLT varying from 12% to 30% as the solar cycle shifts from minimum to maximum. In this study, the period selected is the first part of the solar maximum during solar cycle 24, which was comparable to the period 1987–1989. However, in this study, the peak of upflow occurrence rate, that is, ∼12% near 0 MLT, is lower than their results during 1987–1989 with a peak of upflow occurrence ∼20% near 23 MLT. This is due to the fact that solar cycle 24 is much weaker than solar cycle 22.

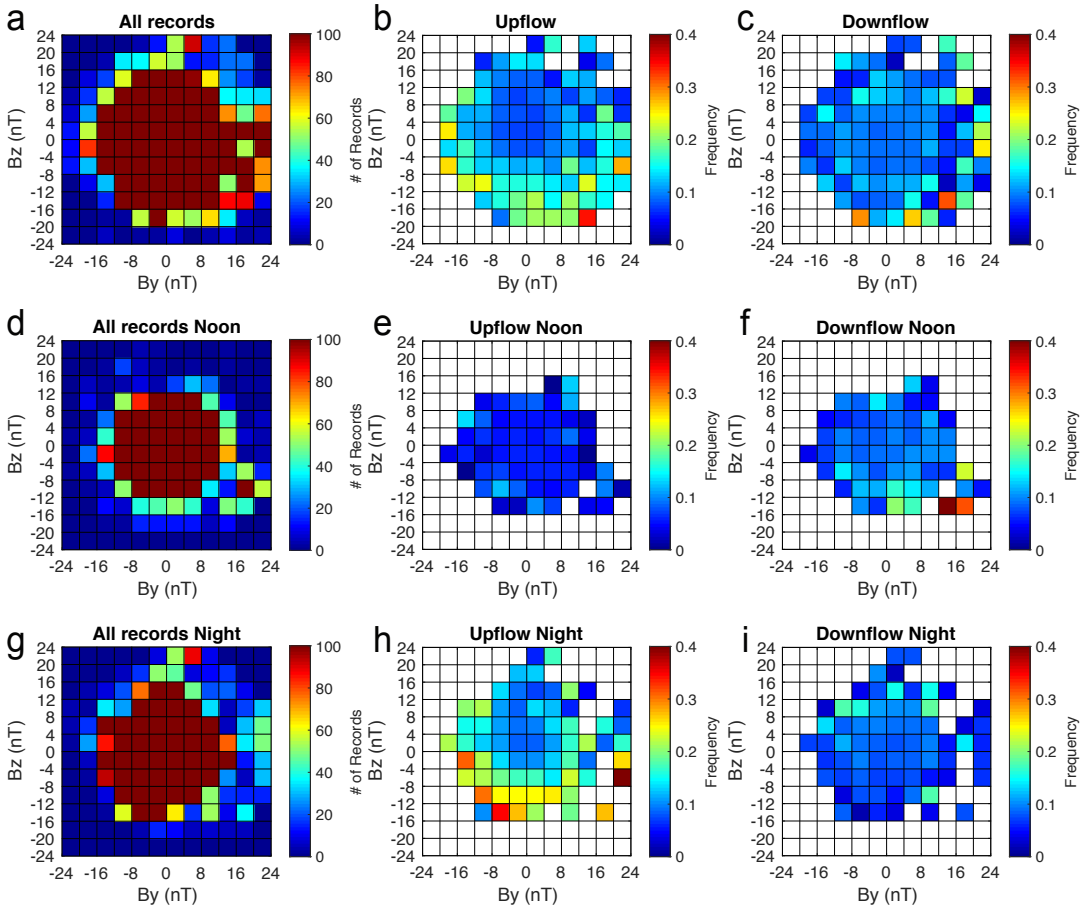

Figure 4.14: Heatmaps showing joint distributions of ion upflow/downflow occurrence frequency on the IMF By and IMF Bz components. Each row represents a certain MLT sector: (a–c) overall MLT (first row), (d–f) on the dayside between 9–15 MLT (second row), (g–i) on the night side between 21–3 MLT (third row). The first column indicates total count of records in each bin, while the second and third columns show distributions of upflow and downflow occurrence frequency, respectively.

This day-night asymmetry can be understood by the relative location of PFISR to auroral oval. As illustrated in Figures 4.15a and 4.15b, under quiet and moderate geomagnetic conditions, this latitude is usually several degrees equatorward of the auroral oval on the dayside but within the nightside auroral oval. During strong driving conditions (Figures 4.15c and 4.15d), such as geomagnetic storms, the auroral oval expands equatorward both on the dayside and nightside, and it could extend to the PFISR latitude or even beyond. The ion upflow occurrence rate starts to show a positive correlation with the geomagnetic activity levels under these circumstances, for example, when the AE index exceeds 1,000 nT (Figure 4.7b) or the SymH index reaches -120 nT (Figure 4.8b).

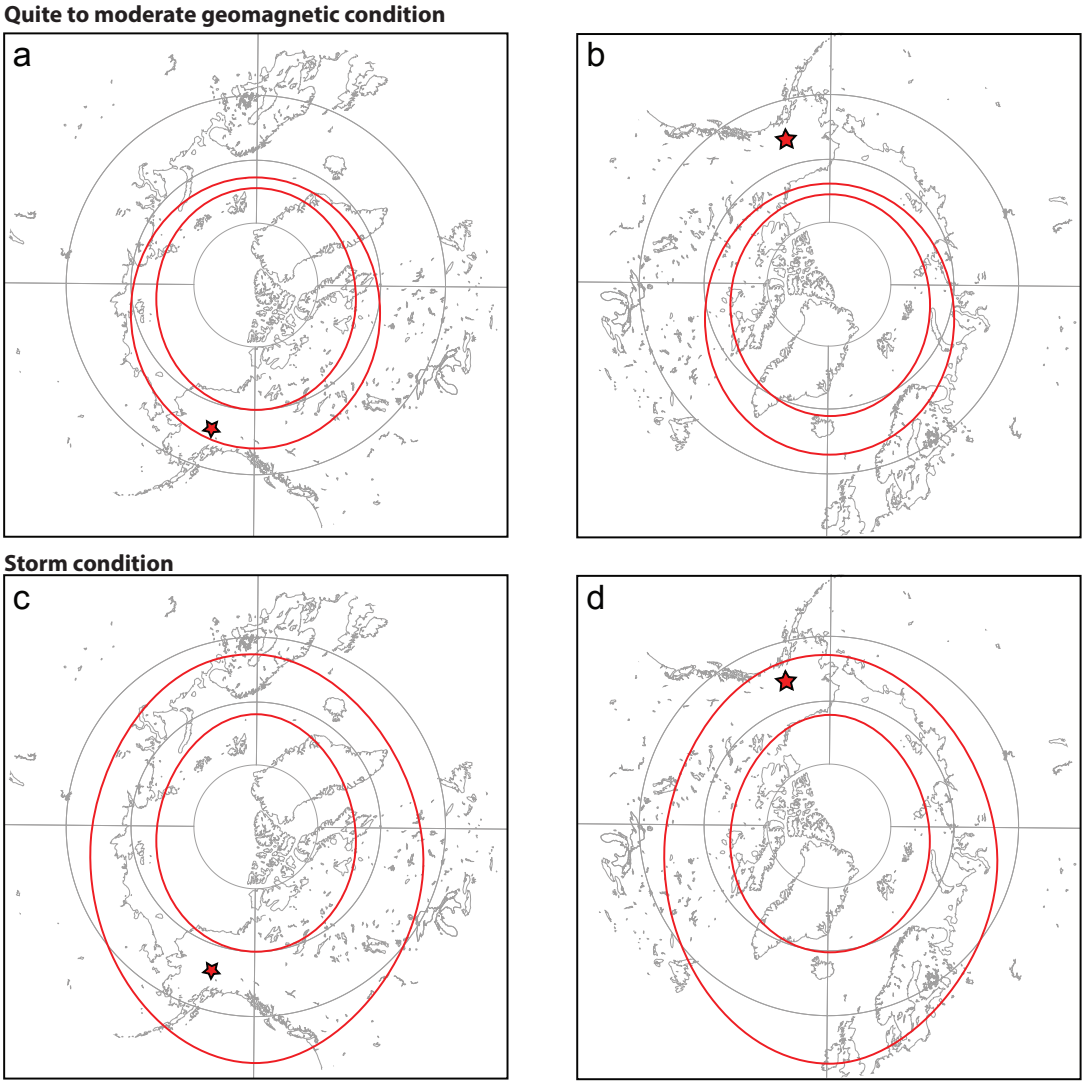

Figure 4.15: Illustration of PFISR location, marked by the star, relative to the auroral zone, during (a, b) quiet to moderate geomagnetic condition and (c, d) storm condition.

The absence of correlation between dayside upflow occurrence and the solar wind and IMF parameters indicates the limited effects from these individual parameters on regions at latitudes as low as PFISR. While in the nightside auroal zone, where parameters like the solar wind velocity, dynamic pressure, and the IMF Bz have direct influence on the precipitation intensity and convection velocity, such correlations are much stronger. This result suggests that the nightside auroral oval is a key region for supplying ions into the magnetosphere.

Compared to the study using data from the EISCAT Svalbard radar (ESR) located at 75.2° MLat (Liu et al., 2001; Ogawa et al., 2009), a clear difference in the diurnal distribution of ion upflow occurrence rate is found. Data from ESR revealed that ion upflow occurs most frequently

on the dayside (09–15 MLT), while PFISR observed much higher frequency for ion upflow on the nightside (21–03 MLT). Due to the difference in geomagnetic latitude, ESR is closer/at auroral zone on the dayside while PFISR is closer/at auroral zone on the nightside. Combining results from both studies, we can conclude that ion upflow occurs preferentially at the dayside cusp and nightside auroral zone.

The altitude distribution shown in Figure 4.3 suggests that on the nightside ion upflow tends to occur at ∼400 km, nearly 100 km lower than that on the dayside. This is consistent with the result reported by Ogawa et al. (2009), which showed that upflow observed during nighttime tends to occur more often at lower altitudes ∼200 km than those during daytime. The main factor contributing to this altitude difference is likely the ionosphere scale height decreasing from the dayside to the nightside due to diurnal variation of solar radiation and therefore plasma temperature, as shown in Figures 4.5a and 4.5b. Another potential reason is that in the nightside auroral oval energetic particle precipitation can penetrate to the E region or even below, while near the dayside cusp region soft particle precipitation are often observed to cause electron heating over a wide range of altitudes above 300 km, accelerating the ions upward through ambipolar electric field (Burchill et al., 2010).

As shown in Figures 4.4a–4.4c, the enhanced plasma density, ion, and electron temperature associated with the ion upflow between 15–6 MLT indicate contributions from both frictional heatings and particle precipitation. However, on the dayside between 7 and 14 MLT, no significant difference are seen in the density or temperature distribution of the ion upflow observed. Ogawa et al. (2009) suggested that 15–50% of the upflow they found at some MLTs without any ion or electron temperature increase were probably because the time scale of precipitation or Joule heating, in comparison with the time scale of the ion upflow, might be too short for them to be observed simultaneously with the upflow by the ISR. Simulation results by Cohen et al. (2015) suggest that the high plasma number density on the dayside would result in less significant temperature change when given a certain amount of precipitation energy input, but the resulting flux can still increase, as shown in Figure 4.4d, since more ions are being accelerated.

4.4.2 Downflow

Ion downflow has been observed within the tongue-of-ionization and polar cap patches (Ren et al., 2018) or within the SED plume (Zou et al., 2014), which are typical density structures in the high-latitude ionosphere during geomagnetic disturbed periods (Crowley, 1996; Deng and Ridley, 2006; Foster, 1993; Foster et al., 2005; Heelis et al., 2009; Hosokawa et al., 2010; Moen et al., 2008; Ren et al., 2020a; Sato and Rourke, 1964; Thomas et al., 2013; Wang et al., 2019; Weber et al., 1984; Zhang et al., 2015; Zou and Ridley, 2016). In addition, Shen et al. (2018) showed that

downflow associated with ion heating and broadband extremely low frequency (BBELF) waves can occur at altitudes as low as 350–450 km and often in the postmidnight to dawn sector. This could be a potential mechanism producing the downflow observed near 2–6 MLT and ∼450 km altitude in our study, which are associated with clear ion temperature increase as shown in Figure 4.5a. Future study is required to identify potential conjugate events with simultaneous satellite and PFISR conjunctions.

The preference of the ion downflow during strong positive By and southward Bz at the auroral latitudes has never been reported before. It has been well known that IMF By sign change could introduce asymmetries in the ionospheric convection and thermospheric wind pattern (Walsh et al., 2014). In Zou et al. (2013, 2014) and Zou and Ridley (2016), large ion downflow has been observed both by PFISR and in the numerical simulation to be associated with the storm-enhanced density (SED) base and SED plume. In these studies, they found that the downflow was due to a combination of enhanced poleward thermospheric wind and enhanced pressure gradient force within the plume. We have compared the clustered downflow events (more than 50 events within 6 hr) in our data set with the events presented in Zou et al., (2014) and indeed found that they tend to occur on the dayside within SEDs, such as the 13–14 October 2011, 13–14 November 2012, and 23–24 April 2012 storms shown in Figure 6 in Zou et al. (2014). The association with the SED can also explain the clear positive correlation between downflow occurrence and geomagnetic activity levels (Figures 4.7e and 4.7e) only on the dayside, because the SED is only present during storm time on the dayside subauroral region and its size and strength could be positively correlated with the storm intensity. Figure 4.2 clearly shows that the downward flows tend to occur more often in the afternoon sector. This is also likely due to the fact that the SED and SED plume are strongest in the afternoon sector.

4.5 Summary and Conclusions

Using PFISR, located near Fairbanks, Alaska, the dependences of ion upflow and downflow in the ionosphere in terms of the geomagnetic activity and solar wind and IMF conditions have been investigated. This is the first statistical study on ion upflow and downflow for the American sector. Here is the summary for the findings:

1. Ion upflows over PFISR are twice as likely to occur on the nightside than on the dayside and occur slightly more often near summer solstice.

2. On the nightside, both upflows and downflows tend to occur around 400 km, while on the dayside the altitude increases to slightly above/below 500 km for upflows/downflows.

3. Electron temperature and density enhancements for upflows are observed throughout the night side, suggesting the association with auroral particle precipitations. Median ion temperatures increase as large as 100 K are seen from 16 MLT to 6 MLT as well, suggesting contributions from enhanced convection flow speed and frictional heating.

4. The occurrence frequency of both upflow and downflow increases almost monotonically as convection velocity increases. The frequency grows more rapidly on the nightside.

5. The occurrence frequency of ion upflow averaged over all MLTs increases with enhanced geomagnetic activity levels represented by the AE and SymH indices. The strongest increasing trend is observed on the nightside with $\sim$30% peak occurrence rate when AE reaches $\sim$1,200 nT and SymH reaches $\sim$-90 nT.

6. On the nightside, the occurrence frequency of ion upflow increases from below 10% with nearly no magnetic perturbation to above 25%, when there is strong southwestward magnetic perturbation reaching magnitude over 400 nT. This southwestward magnetic perturbation is due to a tilted westward electrojet typically seen just poleward of the Harang reversal and thus suggests the nightside upflow tends to occur during periods with clear Harang signatures, such as substorms.

7. Overall, the occurrence rate of ion upflow increases with enhanced solar wind velocity, number density and dynamic pressure, especially on the nightside. In particular, a stronger dependency is identified for fast solar wind ($>$600 km/s).

8. The occurrence frequency of ion upflow increases as the total IMF and the magnitude of the three IMF components increase. The strongest correlation is observed for southward IMF Bz on the nightside.

9. No clear correlation of upflow on the dayside with any of the solar wind and IMF parameters has been observed. This is because PFISR is typically located equatorward of the dayside auroral zone. Enhanced upflow occurrence on the dayside is observed only during strong geomagnetic activity levels, that is, when SymH reaches -120 nT or AE exceeds 1,000 nT.

10. Ion downflow clearly prefers to occur in the afternoon sector and occur slightly more often near summer solstice.

11. Ion downflow tends to occur more frequently on the dayside during strong geomagnetic activities, indicated by larger AE and more negative SymH, suggesting its association with SED in the dayside subauroral regions.

12. In general, no strong correlation observed between the ion downflow and solar wind parameters, except that when proton number density exceeds over 50 m^{-3} the downflow occurrence frequency increases up to $\sim$18%. The downflow occurrence frequency also slightly increases on the dayside when the solar wind velocity increases.

13. The overall occurrence rate of downflow is not clearly correlated with IMF Bx. However, on the dayside, it clearly occurs much more often when IMF By is strongly positive, that is, $>$10 nT, and when IMF Bz is strongly negative, that is, $<$ -10 nT. Some of these downflow events are associated with SED base and SED plume, as have been shown in Zou et al. (2014).

CHAPTER 5

Summary and Conclusion

5.1 Concluding remarks

In this dissertation, the formation process and plasma characteristics of polar cap patches are investigated in Chapter 2 and 3. The ion upflow occurrence frequency and its correlation with the solar wind, IMF and geomagnetical activity conditions are studied in Chapter 4.

In Chapter 2, we reported comprehensive observations of a polar cap patch being segmented from the SED by a transient fast flow near the cusp. The enhanced flow speed and transient direction change were likely associated with a sudden magnitude increase of the negative IMF By component. The Sondrestrom ISR observation and quantitative estimations show that the patch segmentation was mainly due to plasma transport rather than enhanced recombination induced by frictional heating. The patch formation process can be generalized as follows: first, presence of the SED near the cusp or a preexisted TOI is required; second, there is low-density plasma in adjacent areas; at last, a transient fast flow channel transporting the low-density areas towards the high-density region is needed. If the density peak is lifted in the F2 region to $\sim$500 km, frictional heating is likely not effective for rapid patch segmentation. During geomagnetic storms, the first two conditions can be often seen near the dayside cusp region, and sudden changes in the IMF By may lead to sudden location change of fast flow channels and the subsequent transport of low-density plasma to high-density plasma region and thus the formation of polar cap patches.

In Chapter 3, through a statistical study, we show that most of the polar cap patches share similar electron temperature characteristics as the SED plasma produced by dayside photoionization at lower latitudes, which suggests that majority of the patch plasmas originate from the dayside subauroral region instead of the auroral zone due to particle precipitation. In addition, the patches in the deep polar cap are observed most frequently in the afternoon sector between 1400-1900 MLT, and downward ion fluxes $\sim 10^{13}$ $m^{-2}s^{-1}$ are often observed within the patches, due to pressure gradient and gravitational forces in an almost purely vertical magnetic field environment. As RISR-C collects more data in the following years, the patch identification algorithm presented in

this chapter can be readily applied to a larger data set and a solar cycle dependence of the patch occurrence can be conducted in the future.

In Chapter 4, the correlations of ion upflow and downflow occurrence frequency in the ionosphere with the geomagnetic activity and solar wind and IMF conditions have been investigated using PFISR observations during 2011-2013. The results show that ion upflow at PFISR location are more likely to occur on the nightside and near summer solstice. In general, ion upflows occur at a higher altitude on the dayside than that on the nightside, and the occurrence rate increases with enhanced solar wind and IMF driving, geomagnetic activities and convection speed. On the nightside, ion upflow occurs significantly more frequently when strong southwestward ground magnetic perturbation is present, which is mainly caused by the northwestward auroral electrojet during enhanced geomagnetic activities. Ion downflow clearly occurs more often on the dayside when IMF By $>$10 nT and IMF Bz $<$ -10 nT. Some of these downflow events are associated with the SED base and the SED plume, as have been shown in Zou et al. (2014).

5.2 Future works

5.2.1 Spherical harmonics reconstruction of TEC maps

The Madrigal Database (Rideout and Coster, 2006; Vierinen et al., 2016) provides global maps of vertical TEC measurements calculated from dual-frequency GNSS data collected by worldwide distributed receivers (over 5000 of them). The GNSS system used here include both the Global Positioning System (GPS) and the Global Navigation Satellite System (GLONASS). The Madrigal TEC maps are provided with a spatial resolution of 1° latitude by 1° longitude and a temporal resolution of 5 minutes. Mainly due to the absence of GNSS receivers over the oceans, the TEC measurement is missing at around 75% of the globe. In practice, a 3° by 3° median filter is usually applied to reduce the percentage of missing values down to about 50%, as shown in the left panel of Figure 5.1. In this work, we adopt the median filtered data as the observations and used spherical harmonic (SH) functions to estimate the global TEC distribution.

The SH fitting can create a general estimation on the large-scale TEC distribution. Known as the angular portion of the solutions to the Laplace's equation in spherical coordinates, the SH functions define a complete orthogonal basis and therefore can approximate a sufficiently smooth surface function defined in the spherical coordinates. Treating the TEC map at a given time as a function on spherical coordinates, $f(\theta, \phi)$, we can approximate the TEC distribution using SH expansion

$$f(\theta,\phi) \approx \sum_{l=0}^{l_{max}} \sum_{m=-l}^{l} a_l^m Y_l^m(\theta,\phi),$$

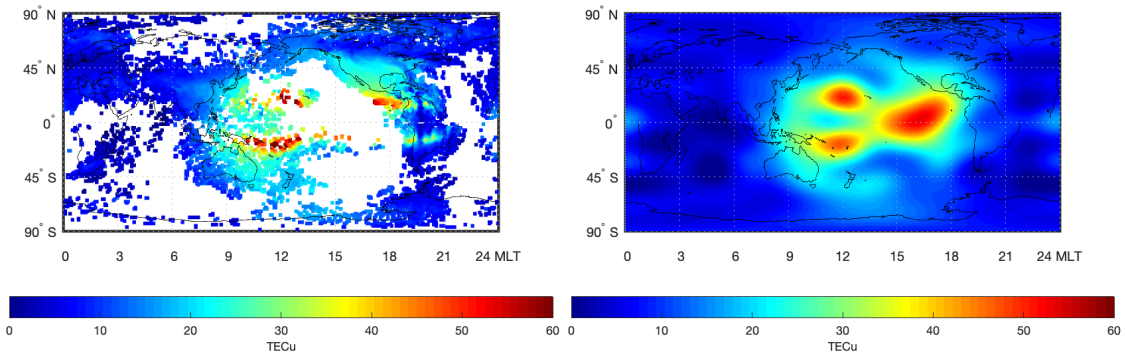

Figure 5.1: (Left) Madrigal TEC map with missing data and (Right) complete TEC map approximated by the spherical harmonics expansion.

where θ and ϕ are the elevation and azimuth angles. $Y_l^m(\theta, \phi)$ denotes a SH with degree m and order l ($|m| \leq l$), and a_l^m is the corresponding coefficient. For convenience, we give each harmonic function with degree m and order l a unique index $j = l^2 + l + m + 1$ and each observation an index i, then we have a system of linear equations in terms of the coefficients

$$\begin{bmatrix} Y_1(\theta_1, \phi_1) & \dots & Y_k(\theta_1, \phi_1) \\ \vdots & \ddots & \vdots \\ Y_1(\theta_N, \phi_N) & \dots & Y_k(\theta_N, \phi_N) \end{bmatrix} \begin{bmatrix} a_1 \\ \vdots \\ a_k \end{bmatrix} \approx \begin{bmatrix} f(\theta_1, \phi_1) \\ \vdots \\ f(\theta_N, \phi_N) \end{bmatrix}$$

that can be written as $YA = F$, where $k = (l_{max} + 1)^2$ and N is the total number of observations in the TEC map. The best coefficients A can be obtained by solving the least-square optimization problem with Tikhonov regularization

$$\min_A \|F - YA\|_2^2 + v\|\Gamma A\|_2^2$$

where Γ is a diagonal matrix with $\Gamma_{j,j} = l_j(l_j + 1)$ and l_j denotes the order of the j^{th} harmonic function. The purpose of having Tikhonov regularization is to avoid overfitting artifacts by penalizing high-frequency harmonics. Lastly, negative TEC values are removed based on a method using inequality constraints (Zhang et al., 2013).

To determine an optimal set of parameters $\{l_{max}, \mu\}$, data at certain longitudes and latitudes were reserved for validation, while the remaining data were used for the SH fit, as shown in Figure 5.2. Then, as shown in Figure 5.3, mean square error (MSE) between the fitted values and measured values of the validation data was calculated for each $\{l_{max}, \mu\}$ combination in a grid search. In Figure 5.4, as the maximum order l_{max} reaches 15, significant artifacts start to occur, e.g. low-TEC patches (blue) appear within the high-TEC region (red) near the equator. Comparing $\{l_{max} =$

$15, \mu = 0\}$ with $\{l_{max} = 15, \mu = 0.1\}$, it's noted that the low-TEC artifacts are eliminated by adding regularization. By fixing μ at 0.1 while increasing l_{max} from 1 to 15, as shown in Figure 5.4, the SH fitting result can better approximate detailed TEC structures as l_{max} increases from 1 to 5. However, artifacts start to appear when l_{max} continues to increase. In Figure 5.4, it can be noted that a high-TEC patch suddenly appear near 45° S latitude when l_{max} changes from 8 to 9. Figure 5.5 shows the MSE calculated with the validation data at different $\{l_{max}, \mu\}$ parameters. When $l_{max} \leq 5$, the MSE drops rapidly with l_{max} due to the better approximation achieved by the higher complexity of the SH expansion. For $l_{max} \geq 5$, the presence of artifact gradually becomes more dominant and the fitting results starts to get worse for $l_{max} \geq 12$. Based on the results shown in Figure 5.4 and Figure 5.5, $\{l_{max} = 8, \mu = 0.1\}$ is considered the optimal pair of parameter that produces the best approximation to the observations without creating significant artifact.

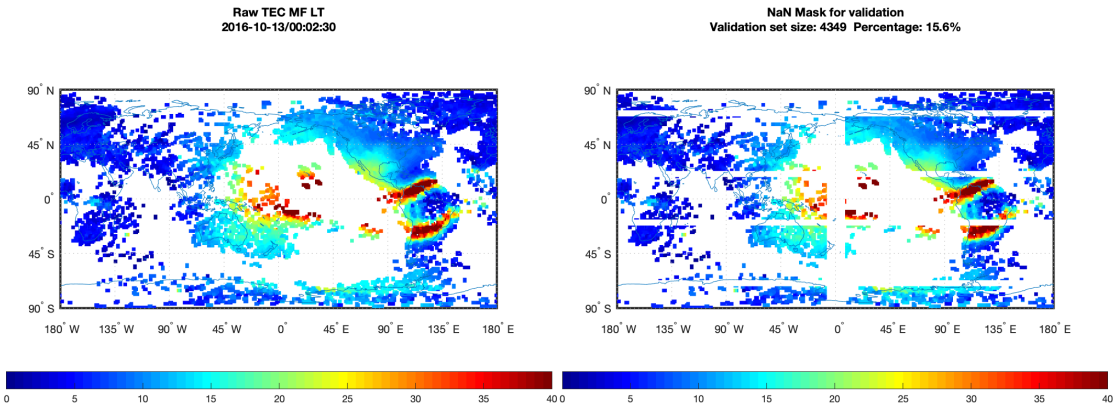

Figure 5.2: (Left) Madrigal TEC map with missing data and (Right) Remaining data used for the SH fit after the validation data are removed.

5.2.2 TEC maps imputation

Using the SH fit of Madrigal TEC maps described in Section 5.2.1 as auxiliary data, we can adopt a matrix completion method named *Video Imputation with SoftImpute, Temporal smoothing and Auxiliary data* (VISTA) that is proposed by Sun et al. (2020) to obtain complete TEC maps with all the data gaps filled with imputed TEC values. The VISTA algorithm takes a time sequence of TEC maps as input and leverages the information in the auxiliary data and neighboring maps in the sequence to impute the missing TEC values. For regions where data is available, the algorithm would use values as close to the measurements as possible.

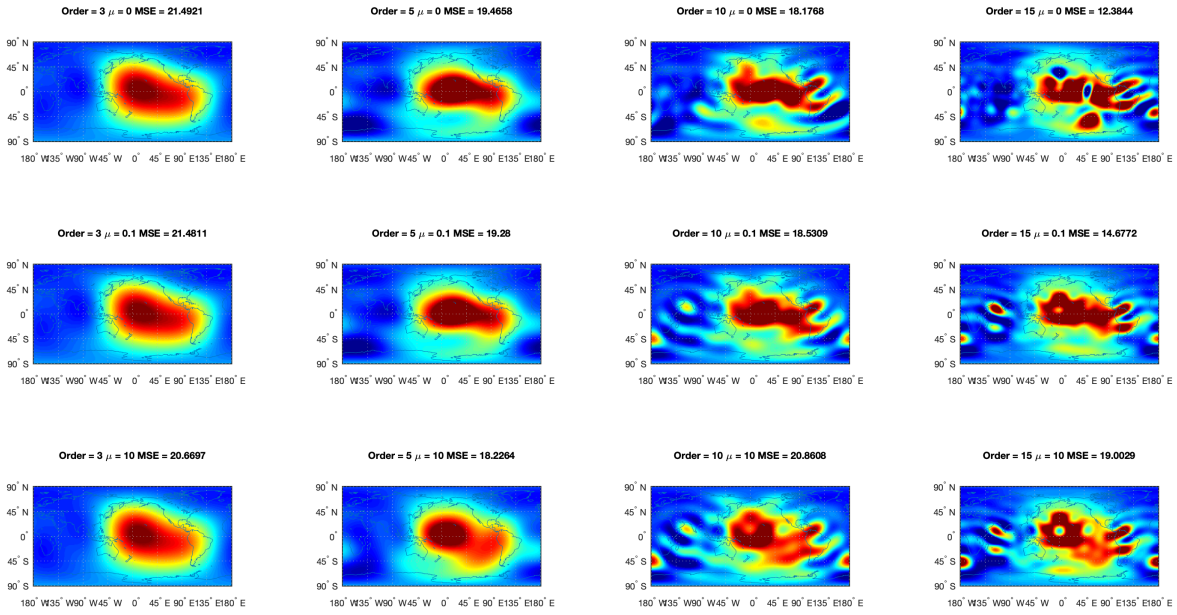

Figure 5.3: SH fit results by using different parameters $\{l_{max}, \mu\}$ and the corresponding MSE calculated using the validation data.

The advantage of the obtained VISTA TEC maps is that mesoscale structures observed in the original TEC maps are well preserved while the missing data points are filled in with reasonable values. In Figure 5.6, a comparison of an original Madrigal TEC map, its SH fit and VISTA TEC map is shown. The left panel of Figure 5.6, the same as Figure 1.8, shows the appearance of a polar cap patch in the Northern Hemisphere during a geomagnetic storm on September 8, 2017. The west half of the patch is mostly buried by a large block of data gap. In the middle panel of Figure 5.6, we can see that the SH fit gives a smooth estimation of the TEC distribution with little mesoscale structures. In the right panel of Figure 5.6, it can be seen that the VISTA algorithm is able to keep most of the observed TEC structures unchanged while it manages to fill the data gaps with reasonably good values.

5.2.3 Application of VISTA TEC maps for ionosphere research

The TEC map is a key data set for studies on various important ionosphere subjects, such as equatorial ionization anomaly, plasma bubbles, travelling ionospheric disturbances, mid- and high-latitude trough, SED, polar cap patches and even auroral precipitations. By leveraging the complete

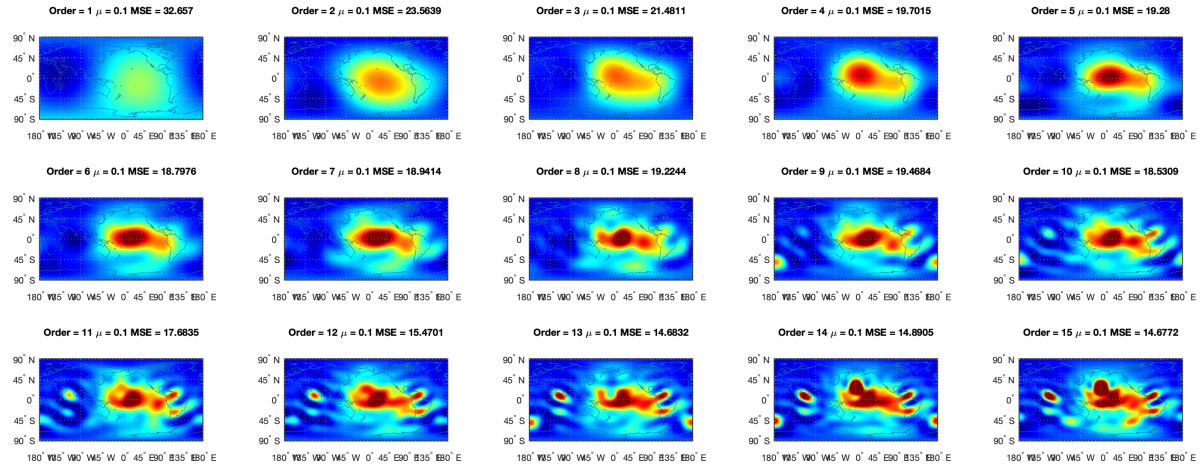

Figure 5.4: SH fit results by using different orders l_{max} while fixing $\mu = 0.1$ and the corresponding MSE calculated using the validation data.

VISTA TEC maps, we can develop algorithms for automatic identification of these ionosphere subjects without issues caused by the large data gaps, and then construct events database for statistical studies. By treating TEC maps as images, a variety of computer vision algorithms, like object detection, movement tracking and image segmentation, could be potentially applicable to such problems. With multiple years of complete TEC maps, high-performance machine learning models can be developed to forecast global ionosphere density distribution.

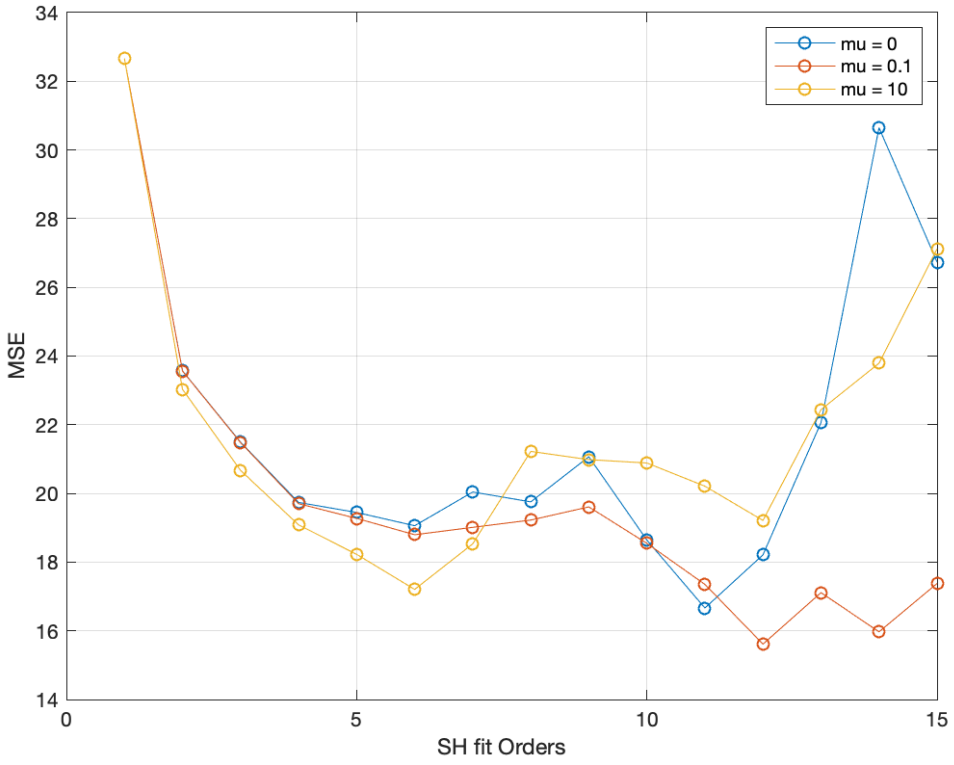

Figure 5.5: MSE for different parameter pairs $\{l_{max}, \mu\}$ calculated using the validation data.

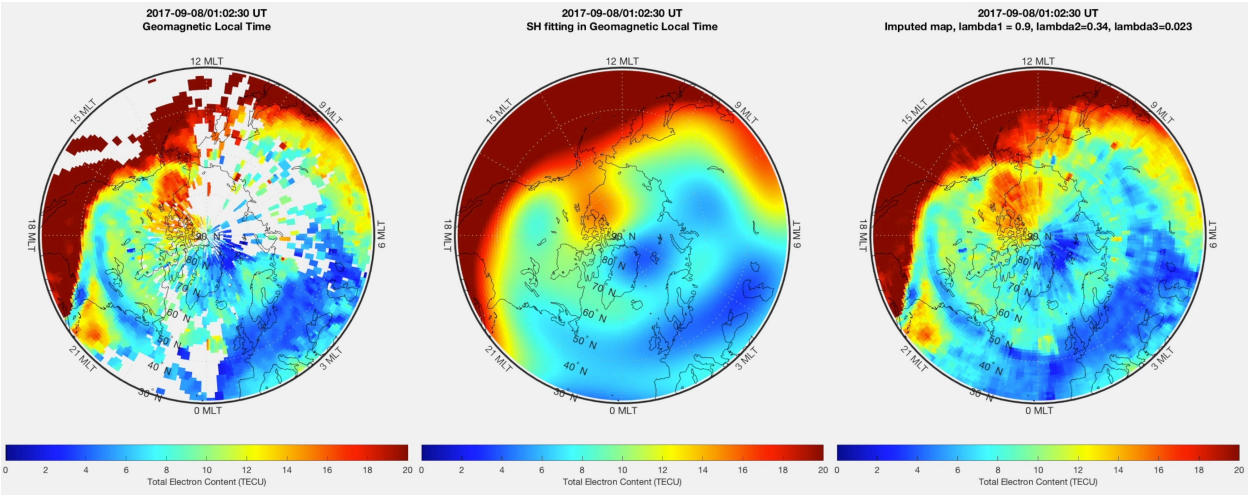

Figure 5.6: (Left) Polar view of Madrigal TEC map (after applying a 3-by-3 median filter) with missing data, same as Figure 1.8, (Middle) TEC map approximated by the spherical harmonics expansion, and (Right) complete TEC map obtained by applying the VISTA method. TEC structures such as polar cap patch and auroral oval enhancement are well persevered in the imputed map.

BIBLIOGRAPHY

B. J. Anderson, H. Korth, C. L. Waters, D. L. Green, V. G. Merkin, R. J. Barnes, and L. P. Dyrud. Development of large-scale birkeland currents determined from the active magnetosphere and planetary electrodynamics response experiment. 41(9):3017–3025, may 2014. doi: 10.1002/2014gl059941. URL https://doi.org/10.1002%2F2014gl059941.

D. N. Anderson, J. Buchau, and R. A. Heelis. Origin of density enhancements in the winter polar cap ionosphere. 23(4):513–519, jul 1988. doi: 10.1029/rs023i004p00513. URL https://doi.org/10.1029%2Frs023i004p00513.

G. Atkinson and D. Hutchison. Effect of the day night ionospheric conductivity gradient on polar cap convective flow. 83(A2):725, 1978. doi: 10.1029/ja083ia02p00725. URL https://doi.org/10.1029%2Fja083ia02p00725.

W. I. Axford and C. O. Hines. A unifying theory of high-latitude geophysical phenomena and geomagnetic storms. *Canadian Journal of Physics*, 39(10):1433–1464, 1961.

S. Basu, E. MacKenzie, S. Basu, E. Costa, P. Fougere, H. Carlson, and H. Whitney. 250 MHz/GHz scintillation parameters in the equatorial, polar, and auroral environments. 5(2):102–115, feb 1987. doi: 10.1109/jsac.1987.1146533. URL https://doi.org/10.1109%2Fjsac.1987.1146533.

S. Basu, E. MacKenzie, and S. Basu. Ionospheric constraints on VHF/UHF communications links during solar maximum and minimum periods. 23(3):363–378, may 1988. doi: 10.1029/rs023i003p00363. URL https://doi.org/10.1029%2Frs023i003p00363.

H. F. Bates. Atmospheric expansion from joule heating. 22(6):925–937, jun 1974. doi: 10.1016/0032-0633(74)90162-7. URL https://doi.org/10.1016%2F0032-0633%2874%2990162-7.

S. D. Browett, R. C. Fear, A. Grocott, and S. E. Milan. Timescales for the penetration of IMF by into the earth's magnetotail. 122(1):579–593, jan 2017. doi: 10.1002/2016ja023198. URL https://doi.org/10.1002%2F2016ja023198.

S. C. Buchert, Y. Ogawa, R. Fujii, and A. P. van Eyken. Observations of diverging field-aligned ion flow with the ESR. 22(3):889–899, mar 2004. doi: 10.5194/angeo-22-889-2004. URL https://doi.org/10.5194%2Fangeo-22-889-2004.

J. Burch, P. Reiff, J. Menietti, R. Heelis, W. Hanson, S. Shawhan, E. Shelley, M. Sugiura, D. Weimer, and J. Winningham. Imf by-dependent plasma flow and birkeland currents in the dayside magnetosphere: 1. dynamics explorer observations. *Journal of Geophysical Research: Space Physics*, 90(A2):1577–1593, 1985.

J. K. Burchill, D. J. Knudsen, J. H. Clemmons, K. Oksavik, R. F. Pfaff, C. T. Steigies, A. W. Yau, and T. K. Yeoman. Thermal ion upflow in the cusp ionosphere and its dependence on soft electron energy flux. 115(A5):n/a–n/a, may 2010. doi: 10.1029/2009ja015006. URL https://doi.org/10.1029%2F2009ja015006.

H. C. Carlson. Ionospheric patch formation: Direct measurements of the origin of a polar cap patch. 31(8), 2004. doi: 10.1029/2003gl018166. URL https://doi.org/10.1029%2F2003gl018166.

H. C. Carlson. Sharpening our thinking about polar cap ionospheric patch morphology, research, and mitigation techniques. 47(4), may 2012. doi: 10.1029/2011rs004946. URL https://doi.org/10.1029%2F2011rs004946.

H. C. Carlson, J. Moen, K. Oksavik, C. P. Nielsen, I. W. McCrea, T. R. Pedersen, and P. Gallop. Direct observations of injection events of subauroral plasma into the polar cap. 33(5), 2006. doi: 10.1029/2005gl025230. URL https://doi.org/10.1029%2F2005gl025230.

C. R. Chappell. The role of the ionosphere in providing plasma to the terrestrial magnetosphere—an historical overview. 192(1-4):5–25, jul 2015. doi: 10.1007/s11214-015-0168-5. URL https://doi.org/10.1007%2Fs11214-015-0168-5.

L. B. N. Clausen, J. B. H. Baker, J. M. Ruohoniemi, S. E. Milan, J. C. Coxon, S. Wing, S. Ohtani, and B. J. Anderson. Temporal and spatial dynamics of the regions 1 and 2 birkeland currents during substorms. 118(6):3007–3016, jun 2013. doi: 10.1002/jgra.50288. URL https://doi.org/10.1002%2Fjgra.50288.

I. J. Cohen, M. R. Lessard, R. H. Varney, K. Oksavik, M. Zettergren, and K. A. Lynch. Ion upflow dependence on ionospheric density and solar photoionization. *Journal of Geophysical Research: Space Physics*, 120(11):10039–10052, 2015. doi: https://doi.org/10.1002/2015JA021523. URL https://agupubs.onlinelibrary.wiley.com/doi/abs/10.1002/2015JA021523.

W. R. Coley and R. A. Heelis. Adaptive identification and characterization of polar ionization patches. 100(A12):23819, 1995. doi: 10.1029/95ja02700. URL https://doi.org/10.1029%2F95ja02700.

W. R. Coley, R. A. Heelis, and M. R. Hairston. Characteristics of high-latitude vertical plasma flow from the defense meteorological satellite program. 111(A11), nov 2006. doi: 10.1029/2005ja011553. URL https://doi.org/10.1029%2F2005ja011553.

G. Crowley. Critical review of ionospheric patches and blobs. *Review of Radio Science 1993–1996*, pages 619–648, 1996.

M. David, J. Sojka, R. Schunk, M. Liemohn, and A. Coster. Dayside midlatitude ionospheric response to storm time electric fields: A case study for 7 september 2002. *Journal of Geophysical Research: Space Physics*, 116(A12), 2011.

M. David, J. J. Sojka, R. W. Schunk, and A. J. Coster. Polar cap patches and the tongue of ionization: A survey of GPS TEC maps from 2009 to 2015. 43(6):2422–2428, mar 2016. doi: 10.1002/2016gl068136. URL https://doi.org/10.1002%2F2016gl068136.

Y. Deng and A. J. Ridley. Role of vertical ion convection in the high-latitude ionospheric plasma distribution. 111(A9), 2006. doi: 10.1029/2006ja011637. URL https://doi.org/10.1029%2F2006ja011637.

J. W. Dungey. Interplanetary magnetic field and the auroral zones. *Physical Review Letters*, 6(2): 47, 1961.

M. Endo, R. Fujii, Y. Ogawa, S. C. Buchert, S. Nozawa, S. Watanabe, and N. Yoshida. Ion upflow and downflow at the topside ionosphere observed by the EISCAT VHF radar. 18(2):170–181, feb 2000. doi: 10.1007/s00585-000-0170-3. URL https://doi.org/10.1007%2Fs00585-000-0170-3.

C. Foster, M. Lester, and J. A. Davies. A statistical study of diurnal, seasonal and solar cycle variations of f-region and topside auroral upflows observed by EISCAT between 1984 and 1996. 16(10):1144–1158, oct 1998. doi: 10.1007/s00585-998-1144-0. URL https://doi.org/10.1007%2Fs00585-998-1144-0.

J. C. Foster. Storm time plasma transport at middle and high latitudes. 98(A2):1675–1689, feb 1993. doi: 10.1029/92ja02032. URL https://doi.org/10.1029%2F92ja02032.

J. C. Foster, A. J. Coster, P. J. Erickson, J. M. Holt, F. D. Lind, W. Rideout, M. McCready, A. van Eyken, R. J. Barnes, R. A. Greenwald, and F. J. Rich. Multiradar observations of the polar tongue of ionization. 110(A9), sep 2005. doi: 10.1029/2004ja010928. URL https://doi.org/10.1029%2F2004ja010928.

R. G. Gillies, A. van Eyken, E. Spanswick, M. Nicolls, J. Kelly, M. Greffen, D. Knudsen, M. Connors, M. Schutzer, T. Valentic, M. Malone, J. Buonocore, J.-P. St.-Maurice, and E. Donovan. First observations from the RISR-c incoherent scatter radar. 51(10):1645–1659, oct 2016. doi: 10.1002/2016rs006062. URL https://doi.org/10.1002%2F2016rs006062.

J. W. Gjerloev. The SuperMAG data processing technique. 117(A9):n/a–n/a, sep 2012. doi: 10.1029/2012ja017683. URL https://doi.org/10.1029%2F2012ja017683.

T. I. Gombosi. *The Ionosphere*, page 176–208. Cambridge Atmospheric and Space Science Series. Cambridge University Press, 1998. doi: 10.1017/CBO9780511529474.011.

D. L. Green, C. L. Waters, B. J. Anderson, H. Korth, and R. J. Barnes. Comparison of large-scale birkeland currents determined from iridium and SuperDARN data. 24(3):941–959, may 2006. doi: 10.5194/angeo-24-941-2006. URL https://doi.org/10.5194%2Fangeo-24-941-2006.

R. A. Greenwald, J. M. Ruohoniemi, K. B. Baker, W. A. Bristow, G. J. Sofko, J.-P. Villain, M. Lester, and J. Slavin. Convective response to a transient increase in dayside reconnection. *Journal of Geophysical Research: Space Physics*, 104(A5):10007–10015, 1999.

J. K. Hargreaves. *The solar-terrestrial environment: an introduction to geospace-the science of the terrestrial upper atmosphere, ionosphere, and magnetosphere*. Cambridge university press, 1992.

R. Heelis. The effects of interplanetary magnetic field orientation on dayside high-latitude ionospheric convection. *Journal of Geophysical Research: Space Physics*, 89(A5):2873–2880, 1984.

R. A. Heelis, J. J. Sojka, M. David, and R. W. Schunk. Storm time density enhancements in the middle-latitude dayside ionosphere. 114(A3):n/a–n/a, mar 2009. doi: 10.1029/2008ja013690. URL https://doi.org/10.1029%2F2008ja013690.

K. Hosokawa, T. Kashimoto, S. Suzuki, K. Shiokawa, Y. Otsuka, and T. Ogawa. Motion of polar cap patches: A statistical study with all-sky airglow imager at resolute bay, canada. 114 (A4):n/a–n/a, apr 2009. doi: 10.1029/2008ja014020. URL https://doi.org/10.1029%2F2008ja014020.

K. Hosokawa, T. Tsugawa, K. Shiokawa, Y. Otsuka, N. Nishitani, T. Ogawa, and M. R. Hairston. Dynamic temporal evolution of polar cap tongue of ionization during magnetic storm. 115(A12): n/a–n/a, dec 2010. doi: 10.1029/2010ja015848. URL https://doi.org/10.1029%2F2010ja015848.

W. Hughes. The magnetopause, magnetotail, and magnetic reconnection. *Introduction to space physics*, pages 227–287, 1995.

E.-Y. Ji, G. Jee, and C. Lee. Characteristics of the occurrence of ion upflow in association with ion/electron heating in the polar ionosphere. 124(7):6226–6236, jul 2019. doi: 10.1029/2019ja026799. URL https://doi.org/10.1029%2F2019ja026799.

C. Y. Johnson. Ionospheric composition and density from 90 to 1200 kilometers at solar minimum. *Journal of Geophysical Research*, 71(1):330–332, 1966.

J. Keating, F. Mulligan, D. Doyle, K. Winser, and M. Lockwood. A statistical study of large field-aligned flows of thermal ions at high-latitudes. 38(9):1187–1201, sep 1990. doi: 10.1016/0032-0633(90)90026-m. URL https://doi.org/10.1016%2F0032-0633%2890%2990026-m.

M. C. Kelley. *The Earth's ionosphere: plasma physics and electrodynamics*. Academic press, 2009.

M. G. Kivelson, M. G. Kivelson, and C. T. Russell. *Introduction to space physics*. Cambridge university press, 1995.

W. C. Knudsen. Magnetospheric convection and the high-latitudeF2ionosphere. 79(7):1046–1055, mar 1974. doi: 10.1029/ja079i007p01046. URL https://doi.org/10.1029%2Fja079i007p01046.

H. Liu, S.-Y. Ma, and K. Schlegel. Diurnal, seasonal, and geomagnetic variations of large field-aligned ion upflows in the high-latitude ionosphericFregion. 106(A11):24651–24661, nov 2001. doi: 10.1029/2001ja900047. URL https://doi.org/10.1029%2F2001ja900047.

J. Liu, W. Wang, A. Burns, S. C. Solomon, S. Zhang, Y. Zhang, and C. Huang. Relative importance of horizontal and vertical transports to the formation of ionospheric storm-enhanced density and polar tongue of ionization. 121(8):8121–8133, aug 2016. doi: 10.1002/2016ja022882. URL https://doi.org/10.1002%2F2016ja022882.

M. Lockwood and H. C. Carlson. Production of polar cap electron density patches by transient magnetopause reconnection. 19(17):1731–1734, sep 1992. doi: 10.1029/92gl01993. URL https://doi.org/10.1029%2F92gl01993.

M. Loranc and J. P. S. Maurice. A time-dependent gyro-kinetic model of thermal ion upflows in the high-latitudeFregion. 99(A9):17429, 1994. doi: 10.1029/93ja01852. URL https://doi.org/10.1029%2F93ja01852.

M. Loranc, W. B. Hanson, R. A. Heelis, and J.-P. St.-Maurice. A morphological study of vertical ionospheric flows in the high-latitudeFregion. 96(A3):3627, 1991. doi: 10.1029/90ja02242. URL https://doi.org/10.1029%2F90ja02242.

W. Lotko. The magnetosphere–ionosphere system from the perspective of plasma circulation: A tutorial. 69(3):191–211, mar 2007. doi: 10.1016/j.jastp.2006.08.011. URL https://doi.org/10.1016%2Fj.jastp.2006.08.011.

G. Lu, L. Goncharenko, M. J. Nicolls, A. Maute, A. Coster, and L. J. Paxton. Ionospheric and thermospheric variations associated with prompt penetration electric fields. 117(A8): n/a–n/a, aug 2012. doi: 10.1029/2012ja017769. URL https://doi.org/10.1029%2F2012ja017769.

Y.-Z. Ma, Q.-H. Zhang, Z.-Y. Xing, P. T. Jayachandran, J. Moen, R. A. Heelis, and Y. Wang. Combined contribution of solar illumination, solar activity, and convection to ion upflow above the polar cap. 123(5):4317–4328, may 2018. doi: 10.1029/2017ja024974. URL https://doi.org/10.1029%2F2017ja024974.

D. J. McEwen and D. P. Harris. Occurrence patterns ofFlayer patches over the north magnetic pole. 31(3):619–628, may 1996. doi: 10.1029/96rs00312. URL https://doi.org/10.1029%2F96rs00312.

S. E. Milan, M. Lester, S. Cowley, and M. Brittnacher. Dayside convection and auroral morphology during an interval of northward interplanetary magnetic field. In *Annales Geophysicae*, volume 18, pages 436–444. Springer, 2000.

J. Moen, N. Gulbrandsen, D. A. Lorentzen, and H. C. Carlson. On the MLT distribution ofFregion polar cap patches at night. 34(14), jul 2007. doi: 10.1029/2007gl029632. URL https://doi.org/10.1029%2F2007gl029632.

J. Moen, X. C. Qiu, H. C. Carlson, R. Fujii, and I. W. McCrea. On the diurnal variability in f2-region plasma density above the EISCAT svalbard radar. 26(8):2427–2433, aug 2008. doi: 10.5194/angeo-26-2427-2008. URL https://doi.org/10.5194%2Fangeo-26-2427-2008.

T. E. Moore and J. L. Horwitz. Stellar ablation of planetary atmospheres. 45(3):n/a–n/a, aug 2007. doi: 10.1029/2005rg000194. URL https://doi.org/10.1029%2F2005rg000194.

H. Nilsson, M. Waara, O. Marghitu, M. Yamauchi, R. Lundin, H. Rème, J.-A. Sauvaud, I. Dandouras, E. Lucek, L. M. Kistler, B. Klecker, C. W. Carlson, M. B. Bavassano-Cattaneo, and A. Korth. Transients in oxygen outflow above the polar cap as observed by the cluster spacecraft. 26(11):3365–3373, oct 2008. doi: 10.5194/angeo-26-3365-2008. URL https://doi.org/10.5194%2Fangeo-26-3365-2008.

M. Noja, C. Stolle, J. Park, and H. Lühr. Long-term analysis of ionospheric polar patches based on CHAMP TEC data. 48(3):289–301, may 2013. doi: 10.1002/rds.20033. URL https://doi.org/10.1002%2Frds.20033.

Y. Ogawa, S. C. Buchert, R. Fujii, S. Nozawa, and A. van Eyken. Characteristics of ion upflow and downflow observed with the european incoherent scatter svalbard radar. *Journal of Geophysical Research: Space Physics*, 114(A5), 2009.

Y. Ogawa, K. Seki, K. Keika, and Y. Ebihara. Characteristics of CME- and CIR-driven ion upflows in the polar ionosphere. 124(5):3637–3649, may 2019. doi: 10.1029/2018ja025870. URL https://doi.org/10.1029%2F2018ja025870.

K. Oksavik, J. M. Ruohoniemi, R. A. Greenwald, J. B. H. Baker, J. Moen, H. C. Carlson, T. K. Yeoman, and M. Lester. Observations of isolated polar cap patches by the european incoherent scatter (EISCAT) svalbard and super dual auroral radar network (SuperDARN) finland radars. 111(A5), 2006. doi: 10.1029/2005ja011400. URL https://doi.org/10.1029%2F2005ja011400.

G. Perry and J.-P. S. Maurice. A polar-cap patch detection algorithm for the advanced modular incoherent scatter radar system. *Radio Science*, 53(10):1225–1244, 2018.

R. J. Redmon, W. K. Peterson, L. Andersson, E. A. Kihn, W. F. Denig, M. Hairston, and R. Coley. Vertical thermal oflows at 850 km in dynamic auroral boundary coordinates. 115(A11): n/a–n/a, nov 2010. doi: 10.1029/2010ja015589. URL https://doi.org/10.1029%2F2010ja015589.

P. H. Reiff and J. Burch. Imf by-dependent plasma flow and birkeland currents in the dayside magnetosphere: 2. a global model for northward and southward imf. *Journal of Geophysical Research: Space Physics*, 90(A2):1595–1609, 1985.

J. Ren, S. Zou, R. G. Gillies, E. Donovan, and R. H. Varney. Statistical characteristics of polar cap patches observed by RISR-c. 123(8):6981–6995, aug 2018. doi: 10.1029/2018ja025621. URL https://doi.org/10.1029%2F2018ja025621.

J. Ren, S. Zou, E. Kendall, A. Coster, K. Sterne, and M. Ruohoniemi. Direct observations of a polar cap patch formation associated with dayside reconnection driven fast flow. 125(4), apr 2020a. doi: 10.1029/2019ja027745. URL https://doi.org/10.1029%2F2019ja027745.

J. Ren, S. Zou, J. Lu, N. Giertych, Y. Chen, R. H. Varney, and A. S. Reimer. Statistical study of ion upflow and downflow observed by pfisr. *Journal of Geophysical Research: Space Physics*, 125(10):e2020JA028179, 2020b.

W. Rideout and A. Coster. Automated GPS processing for global total electron content data. *GPS Solutions*, 10(3):219–228, 2006. ISSN 10805370. doi: 10.1007/s10291-006-0029-5.

A. S. Rodger, M. Pinnock, J. R. Dudeney, K. B. Baker, and R. A. Greenwald. A new mechanism for polar patch formation. 99(A4):6425, 1994. doi: 10.1029/93ja01501. URL https://doi.org/10.1029%2F93ja01501.

Z. J. Rong, A. T. Y. Lui, W. X. Wan, Y. Y. Yang, C. Shen, A. A. Petrukovich, Y. C. Zhang, T. L. Zhang, and Y. Wei. Time delay of interplanetary magnetic field penetration into earth's magnetotail. 120(5):3406–3414, may 2015. doi: 10.1002/2014ja020452. URL https://doi.org/10.1002%2F2014ja020452.

J. Ruohoniemi and R. Greenwald. The response of high-latitude convection to a sudden southward imf turning. *Geophysical Research Letters*, 25(15):2913–2916, 1998.

J. M. Ruohoniemi and K. B. Baker. Large-scale imaging of high-latitude convection with super dual auroral radar network HF radar observations. 103(A9):20797–20811, sep 1998. doi: 10.1029/98ja01288. URL https://doi.org/10.1029%2F98ja01288.

J. M. Ruohoniemi and R. A. Greenwald. Statistical patterns of high-latitude convection obtained from goose bay HF radar observations. 101(A10):21743–21763, oct 1996. doi: 10.1029/96ja01584. URL https://doi.org/10.1029%2F96ja01584.

J. M. Ruohoniemi and R. A. Greenwald. Dependencies of high-latitude plasma convection: Consideration of interplanetary magnetic field, seasonal, and universal time factors in statistical patterns. 110(A9), sep 2005. doi: 10.1029/2004ja010815. URL https://doi.org/10.1029%2F2004ja010815.

T. Sato and G. F. Rourke. F-region enhancements in the antarctic. 69(21):4591–4607, nov 1964. doi: 10.1029/jz069i021p04591. URL https://doi.org/10.1029%2Fjz069i021p04591.

R. Schunk and A. Nagy. Space environment. In *Ionospheres*, pages 11–49. Cambridge University Press, Cambridge, 2009. doi: 10.1017/CBO9780511635342.002. URL https://www.cambridge.org/core/product/identifier/CBO9780511635342A011/type/book_part.

J. Semeter, C. J. Heinselman, J. P. Thayer, R. A. Doe, and H. U. Frey. Ion upflow enhanced by driftingF-region plasma structure along the nightside polar cap boundary. 30(22), nov 2003. doi: 10.1029/2003gl017747. URL https://doi.org/10.1029%2F2003gl017747.

Y. Seo, J. L. Horwitz, and R. Caton. Statistical relationships between high-latitude ionosphericFregion/topside upflows and their drivers: DE 2 observations. 102(A4):7493–7500, apr 1997. doi: 10.1029/97ja00151. URL https://doi.org/10.1029%2F97ja00151.

Y. Shen, D. J. Knudsen, J. K. Burchill, A. D. Howarth, A. W. Yau, D. M. Miles, H. G. James, G. W. Perry, and L. Cogger. Low-altitude ion heating, downflowing ions, and BBELF waves in the return current region. 123(4):3087–3110, apr 2018. doi: 10.1002/2017ja024955. URL https://doi.org/10.1002%2F2017ja024955.

J. Sojka, W. Raitt, and R. Schunk. Effect of displaced geomagnetic and geographic poles on high-latitude plasma convection and ionospheric depletions. 84(A10):5943, 1979. doi: 10.1029/ja084ia10p05943. URL https://doi.org/10.1029%2Fja084ia10p05943.

J. J. Sojka, M. D. Bowline, and R. W. Schunk. Patches in the polar ionosphere: UT and seasonal dependence. 99(A8):14959, 1994. doi: 10.1029/93ja03327. URL https://doi.org/10.1029%2F93ja03327.

A. Spicher, L. B. N. Clausen, W. J. Miloch, V. Lofstad, Y. Jin, and J. I. Moen. Interhemispheric study of polar cap patch occurrence based on swarm in situ data. 122(3):3837–3851, mar 2017. doi: 10.1002/2016ja023750. URL https://doi.org/10.1002%2F2016ja023750.

J. P. St.-Maurice and D. G. Torr. Nonthermal rate coefficients in the ionosphere: The reactions of owith n2, o2, and NO. 83(A3):969, 1978. doi: 10.1029/ja083ia03p00969. URL https://doi.org/10.1029%2Fja083ia03p00969.

R. J. Strangeway. Factors controlling ionospheric outflows as observed at intermediate altitudes. 110(A3), 2005. doi: 10.1029/2004ja010829. URL https://doi.org/10.1029%2F2004ja010829.

H. Sun, Z. Hua, J. Ren, S. Zou, Y. Sun, and Y. Chen. Matrix completion methods for the total electron content video reconstruction, 2020.

T. Tanaka. Interplanetary magnetic fieldByand auroral conductance effects on high-latitude ionospheric convection patterns. 106(A11):24505–24516, nov 2001. doi: 10.1029/2001ja900061. URL https://doi.org/10.1029%2F2001ja900061.

E. G. Thomas, J. B. H. Baker, J. M. Ruohoniemi, L. B. N. Clausen, A. J. Coster, J. C. Foster, and P. J. Erickson. Direct observations of the role of convection electric field in the formation of a polar tongue of ionization from storm enhanced density. 118(3):1180–1189, mar 2013. doi: 10.1002/jgra.50116. URL https://doi.org/10.1002%2Fjgra.50116.

R. T. Tsunoda. High-latitudeFregion irregularities: A review and synthesis. 26(4):719–760, nov 1988. doi: 10.1029/rg026i004p00719. URL https://doi.org/10.1029%2Frg026i004p00719.

J.-N. Tu, M. Dhar, P. Song, B. W. Reinisch, J. L. Green, R. F. Benson, and A. J. Coster. Extreme polar cap density enhancements along magnetic field lines during an intense geomagnetic storm. 112(A5):n/a–n/a, may 2007. doi: 10.1029/2006ja012034. URL https://doi.org/10.1029%2F2006ja012034.

C. E. Valladares, S. Basu, J. Buchau, and E. Friis-Christensen. Experimental evidence for the formation and entry of patches into the polar cap. 29(1):167–194, jan 1994. doi: 10.1029/93rs01579. URL https://doi.org/10.1029%2F93rs01579.

C. E. Valladares, D. T. Decker, R. Sheehan, and D. N. Anderson. Modeling the formation of polar cap patches using large plasma flows. 31(3):573–593, may 1996. doi: 10.1029/96rs00481. URL https://doi.org/10.1029%2F96rs00481.

J. Vierinen, A. J. Coster, W. C. Rideout, P. J. Erickson, and J. Norberg. Statistical framework for estimating GNSS bias. *Atmospheric Measurement Techniques*, 9(3):1303–1312, 2016. ISSN 18678548. doi: 10.5194/amt-9-1303-2016.

J. E. Wahlund, H. J. Opgenoorth, I. Häggström, K. J. Winser, and G. O. L. Jones. EISCAT observations of topside ionospheric ion outflows during auroral activity: Revisited. 97(A3):3019–3037, mar 1992. doi: 10.1029/91ja02438. URL https://doi.org/10.1029%2F91ja02438.

I. K. Walker, J. Moen, L. Kersley, and D. A. Lorentzen. On the possible role of cusp/cleft precipitation in the formation of polar-cap patches. 17(10):1298–1305, oct 1999. doi: 10.1007/s00585-999-1298-4. URL https://doi.org/10.1007%2Fs00585-999-1298-4.

A. P. Walsh, S. Haaland, C. Forsyth, A. M. Keesee, J. Kissinger, K. Li, A. Runov, J. Soucek, B. M. Walsh, S. Wing, and M. G. G. T. Taylor. Dawn–dusk asymmetries in the coupled solar wind–magnetosphere–ionosphere system: a review. 32(7):705–737, jul 2014. doi: 10.5194/angeo-32-705-2014. URL https://doi.org/10.5194%2Fangeo-32-705-2014.

B. Wang, Y. Nishimura, L. R. Lyons, Y. Zou, H. C. Carlson, H. U. Frey, and S. B. Mende. Analysis of close conjunctions between dayside polar cap airglow patches and flow channels by all-sky imager and DMSP. 68(1), sep 2016. doi: 10.1186/s40623-016-0524-z. URL https://doi.org/10.1186%2Fs40623-016-0524-z.

Z. Wang, S. Zou, T. Coppeans, J. Ren, A. Ridley, and T. Gombosi. Segmentation of sed by boundary flows associated with westward drifting partial ring current. *Geophysical Research Letters*, 46(14):7920–7928, 2019. doi: https://doi.org/10.1029/2019GL084041. URL https://agupubs.onlinelibrary.wiley.com/doi/abs/10.1029/2019GL084041.

C. L. Waters, B. J. Anderson, and K. Liou. Estimation of global field aligned currents using the iridium® system magnetometer data. 28(11):2165–2168, jun 2001. doi: 10.1029/2000gl012725. URL https://doi.org/10.1029%2F2000gl012725.

E. J. Weber, J. Buchau, J. G. Moore, J. R. Sharber, R. C. Livingston, J. D. Winningham, and B. W. Reinisch. Flayer ionization patches in the polar cap. 89(A3):1683, 1984. doi: 10.1029/ja089ia03p01683. URL https://doi.org/10.1029%2Fja089ia03p01683.

D. Weimer. A flexible, imf dependent model of high-latitude electric potentials having "space weather" applications. *Geophysical Research Letters*, 23(18):2549–2552, 1996.

D. Weimer. An improved model of ionospheric electric potentials including substorm perturbations and application to the geospace environment modeling november 24, 1996, event. *Journal of Geophysical Research: Space Physics*, 106(A1):407–416, 2001.

D. T. Welling, M. André, I. Dandouras, D. Delcourt, A. Fazakerley, D. Fontaine, J. Foster, R. Ilie, L. Kistler, J. H. Lee, M. W. Liemohn, J. A. Slavin, C.-P. Wang, M. Wiltberger, and A. Yau. The earth: Plasma sources, losses, and transport processes. 192(1-4):145–208, sep 2015. doi: 10.1007/s11214-015-0187-2. URL https://doi.org/10.1007%2Fs11214-015-0187-2.

Q. Wu, G. Jee, C. Lee, J.-H. Kim, Y. H. Kim, W. Ward, and R. H. Varney. First simultaneous multistation observations of the polar cap thermospheric winds. 122(1):907–915, jan 2017. doi: 10.1002/2016ja023560. URL https://doi.org/10.1002%2F2016ja023560.

X.-Y. Wu, J. L. Horwitz, and Y. Seo. Statistical analysis ofFregion and topside ionospheric ion field-aligned flows at high latitudes. 105(A2):2477–2494, feb 2000. doi: 10.1029/1999ja900437. URL https://doi.org/10.1029%2F1999ja900437.

A. W. Yau and M. André. 80(1/2):1–25, 1997. doi: 10.1023/a:1004947203046. URL https://doi.org/10.1023%2Fa%3A1004947203046.

H. Zhang, P. Xu, W. Han, M. Ge, and C. Shi. Eliminating negative VTEC in global ionosphere maps using inequality-constrained least squares. *Advances in Space Research*, 51(6):988–1000, 2013. ISSN 02731177. doi: 10.1016/j.asr.2012.06.026. URL http://dx.doi.org/10.1016/j.asr.2012.06.026.

Q.-H. Zhang, B.-C. Zhang, R.-Y. Liu, M. W. Dunlop, M. Lockwood, J. Moen, H.-G. Yang, H.-Q. Hu, Z.-J. Hu, S.-L. Liu, I. W. McCrea, and M. Lester. On the importance of interplanetary magnetic field |by| on polar cap patch formation. 116(A5), may 2011. doi: 10.1029/2010ja016287. URL https://doi.org/10.1029%2F2010ja016287.

Q.-H. Zhang, M. Lockwood, J. C. Foster, S.-R. Zhang, B.-C. Zhang, I. W. McCrea, J. Moen, M. Lester, and J. M. Ruohoniemi. Direct observations of the full dungey convection cycle in the polar ionosphere for southward interplanetary magnetic field conditions. 120(6):4519–4530, jun 2015. doi: 10.1002/2015ja021172. URL https://doi.org/10.1002%2F2015ja021172.

Q.-H. Zhang, Q.-G. Zong, M. Lockwood, R. A. Heelis, M. Hairston, J. Liang, I. McCrea, B.-C. Zhang, J. Moen, S.-R. Zhang, Y.-L. Zhang, J. M. Ruohoniemi, M. Lester, E. G. Thomas, R.-Y. Liu, M. W. Dunlop, Y. C.-M. Liu, and Y.-Z. Ma. Earth's ion upflow associated with polar cap patches: Global and in situ observations. 43(5):1845–1853, mar 2016. doi: 10.1002/2016gl067897. URL https://doi.org/10.1002%2F2016gl067897.

S. Zou and A. J. Ridley. Modeling of the evolution of storm-enhanced density plume during the 24 to 25 october 2011 geomagnetic storm. pages 205–213. John Wiley & Sons, Inc., oct 2016. doi: 10.1002/9781119066880.ch16. URL https://doi.org/10.1002%2F9781119066880.ch16.

S. Zou, L. Lyons, M. Nicolls, C. Heinselman, and S. Mende. Nightside ionospheric electrodynamics associated with substorms: Pfisr and themis asi observations. *Journal of Geophysical Research: Space Physics*, 114(A12), 2009a.

S. Zou, L. R. Lyons, C.-P. Wang, A. Boudouridis, J. M. Ruohoniemi, P. C. Anderson, P. L. Dyson, and J. C. Devlin. On the coupling between the harang reversal evolution and substorm dynamics: A synthesis of SuperDARN, DMSP, and IMAGE observations. 114(A1):n/a–n/a, jan 2009b. doi: 10.1029/2008ja013449. URL https://doi.org/10.1029%2F2008ja013449.

S. Zou, A. J. Ridley, M. B. Moldwin, M. J. Nicolls, A. J. Coster, E. G. Thomas, and J. M. Ruohoniemi. Multi-instrument observations of SED during 24-25 october 2011 storm: Implications for SED formation processes. 118(12):7798–7809, dec 2013. doi: 10.1002/2013ja018860. URL https://doi.org/10.1002%2F2013ja018860.

S. Zou, M. B. Moldwin, A. J. Ridley, M. J. Nicolls, A. J. Coster, E. G. Thomas, and J. M. Ruohoniemi. On the generation/decay of the storm-enhanced density plumes: Role of the convection flow and field-aligned ion flow. 119(10):8543–8559, oct 2014. doi: 10.1002/2014ja020408. URL https://doi.org/10.1002%2F2014ja020408.

S. Zou, D. Ozturk, R. Varney, and A. Reimer. Effects of sudden commencement on the ionosphere: PFISR observations and global MHD simulation. 44(7):3047–3058, apr 2017a. doi: 10.1002/2017gl072678. URL https://doi.org/10.1002%2F2017gl072678.

S. Zou, A. Ridley, X. Jia, E. Boyd, M. Nicolls, A. Coster, E. Thomas, and J. M. Ruohoniemi. PFISR observation of intense ion upflow fluxes associated with an SED during the 1 june 2013 geomagnetic storm. 122(2):2589–2604, feb 2017b. doi: 10.1002/2016ja023697. URL https://doi.org/10.1002%2F2016ja023697.

S. Zou, J. Ren, Z. Wang, H. Sun, and Y. Chen. Impact of storm-enhanced density (sed) on ion upflow fluxes during geomagnetic storm. *Frontiers in Astronomy and Space Sciences*, 8:162, 2021. ISSN 2296-987X. doi: 10.3389/fspas.2021.746429. URL https://www.frontiersin.org/article/10.3389/fspas.2021.746429.

Y. Zou, Y. Nishimura, L. R. Lyons, K. Shiokawa, E. F. Donovan, J. M. Ruohoniemi, K. A. McWilliams, and N. Nishitani. Localized polar cap flow enhancement tracing using airglow patches: Statistical properties, IMF dependence, and contribution to polar cap convection. 120 (5):4064–4078, may 2015. doi: 10.1002/2014ja020946. URL https://doi.org/10.1002%2F2014ja020946.